

AD-A127 983

ACTA AERONAUTICA ET ASTRONAUTICA SINICA(U) FOREIGN
TECHNOLOGY DIV WRIGHT-PATTERSON AFB OH F QIAN ET AL.
04 MAR 83 FTD-ID(RS)T-0664-82

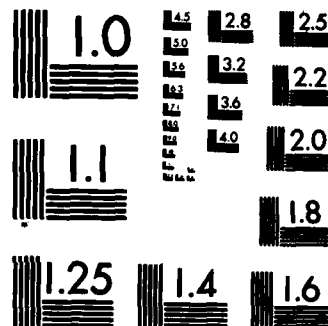
1/3

UNCLASSIFIED

F/G 28/4

NL

A 10x10 grid of squares. The top-left corner contains a pattern of white squares on a black background. The white squares are located at (row, column) coordinates: (1,2), (1,3), (2,1), (2,2), (2,3), (2,4), (3,1), (3,2), (3,3), (3,4), (3,5), (4,1), (4,2), (4,3), (4,4), (4,5), (4,6), (5,1), (5,2), (5,3), (5,4), (5,5), (5,6), (5,7), (6,1), (6,2), (6,3), (6,4), (6,5), (6,6), (6,7), (6,8), (7,1), (7,2), (7,3), (7,4), (7,5), (7,6), (7,7), (7,8), (7,9), (8,1), (8,2), (8,3), (8,4), (8,5), (8,6), (8,7), (8,8), (8,9), (8,10), (9,1), (9,2), (9,3), (9,4), (9,5), (9,6), (9,7), (9,8), (9,9), (9,10), and (10,1) through (10,10). All other squares are black.



MICROCOPY RESOLUTION TEST CHART
NATIONAL BUREAU OF STANDARDS-1963-A

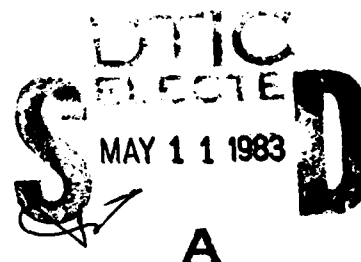
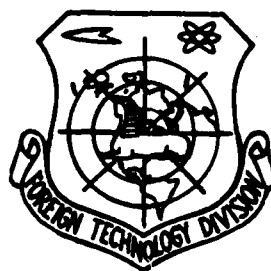
ADA 127983

FTD-ID(RS)T-0664-82

FOREIGN TECHNOLOGY DIVISION



ACTA AERONAUTICA ET ASTRONAUTICA SINICA



Approved for public release;
distribution unlimited.

DTIC FILE COPY

83 05 09-029

EDITED TRANSLATION

FTD-ID(RS)T-0664-82

4 March 1983

MICROFICHE NR: FTD-83-C-000327

ACTA AERONAUTICA ET ASTRONAUTICA SINICA

English pages: 223

Source: Hang Kong Xuebao, Vol. 2, Nr. 1,
1981, pp. 1-103

Country of origin: China

Translated by: LEO KANNER ASSOCIATES
F33657-81-D-0264

Requester: FTD/TQTA

Approved for public release; distribution unlimited.

DTIC
COPY
INSPECTED
2

THIS TRANSLATION IS A RENDITION OF THE ORIGINAL FOREIGN TEXT WITHOUT ANY ANALYTICAL OR EDITORIAL COMMENT. STATEMENTS OR THEORIES ADVOCATED OR IMPLIED ARE THOSE OF THE SOURCE AND DO NOT NECESSARILY REFLECT THE POSITION OR OPINION OF THE FOREIGN TECHNOLOGY DIVISION.

PREPARED BY:

TRANSLATION DIVISION
FOREIGN TECHNOLOGY DIVISION
WP-afb, OHIO.

TABLE OF CONTENTS

Accuracy and Application of a Second-Order Theory for Three-Dimensional Supersonic and Low Hypersonic Unsteady Flows Around a Thin Wing	by/Qian Fuxing, Gu Weikai, He Longde	1
Experimental Investigation on Interferences on Top and Bottom Slotted Walls and Effects of Sidewalls in a Transonic Airfoil Wind Tunnel	by Research Team on Airfoil	17
The Biparametric Cycle Count Method and Principle of Simplification	by Research Team on Aircraft Load Spectrum	38
A General Formula of Stress Intensity Factors for CT Specimens	by/Wang Keren	60
A Finite Element Method for Local Stability of a Stiffened Panel in Axial Compression	by/Liu Dongchang	70
A Universal Method for Solving the Two-Dimensional Cascade Flow Field with Free Streamline Boundaries	by Chen Jingyi	94
Tests for Inlet Distortion in a Two-Spool Turbojet Engine on the Ground Test Bed	by Jiang Feng	113
Fundamental Investigation on Jet Engine Ignition of Fuel Sprays and Its Application	by Cheng Nengkun	134
Development of an Astro-Inertial Hybrid Navigation System and a Star Tracker	by Shen Gongxun, Qin Shiguang, Chang Qingzhi, Zhou Danian	149
Monopulse Technique in Airborne Radar	by Ji Jie	175
Mechanism of Stress Corrosion Cracking and Hydrogen Induced Cracking	by Zhu Wuyang, Li Shiqiong, Xiao Jimei, Zhu Shuyan	196

SOCIETY NEWS

The 1980 Annual Conference of CSAA in Shanghai	215
A Brief About the Conference on Composites by CSAA	217
A Visit of Third CSAA Delegation to the United States	219
A Visit of an AIAA Delegation to China	220
The National Conference on System Simulation Technique in Lushan	222

GRAPHICS DISCLAIMER

All figures, graphics, tables, equations, etc. merged into this translation were extracted from the best quality copy available.

ACCURACY AND APPLICATION OF A SECOND-ORDER THEORY FOR THREE-DIMENSIONAL SUPERSONIC AND LOW HYPERSONIC UNSTEADY FLOWS AROUND A THIN WING

Qian Fuxing, Gu Weikai and He Longde
(Institute of Mechanics, Academia Sinica)

Abstract

This paper deals with the problem of three-dimensional supersonic unsteady flows around a thin wing and utilizes the PLK method so that the second-order solution is uniformly effective. We first considered the situation wherein the angle of attack is zero or there is an initial angle of attack. An unsteady small disturbed flow a magnitude higher is superposed on a known steady flow around a body and it is linearized. This method starts from a sound fundamental equation and uses high Mach number approximations to reduce the unsteady second-order equation. Its form is similar to that of a steady second-order equation. This makes it possible to solve the equation by methods used in the steady second-order theory. The special solution is the key to solving the equation. In view of the complexity of the correct special solution, this paper used a type of special approximation solution.

This method is suitable for the Mach number range between most supersonic and completely hypersonic velocities (about 3-8). The reduced frequency can reach to about 1. We can accurately estimate the influence of the thickness and initial angle of attack on the unsteady aerodynamic force and moment of force.

As related test data is still not available, we can only compare our results with theoretical results. For this reason, we calculated the supersonic flows around a flat delta wing with initial angles of attack at low frequencies. In the range of Mach numbers 3-8, our results were in agreement with those of D.D. Liu [6]. Calculation results show that the second-order theory for three-dimensional thin wings can be used up to a hypersonic approximate parameter of $M_\infty = 1.0$.

LIST OF SYMBOLS

- b = distance between the apex and the fulcrum
 c_o = maximum wing chord
 C_m = pitching moment coefficient
 C_m = pitching moment static derivative $\frac{\partial C_m}{\partial \theta}$
 C = pitching moment dynamic derivative $U \frac{\partial C_m}{c_o \partial \theta}$
 C_p = pressure coefficient
 $C_p^{(0)}, C_{po}^{(0)}, C_{pl}^{(0)}$ = steady component of the pressure coefficient and its first-order and second-order quantities $C_p^{(0)} = C_{po}^{(0)} + C_{pl}^{(0)}$
 $C_p^{(1)}, C_{po}^{(1)}, C_{pl}^{(1)}$ = the unsteady component of the pressure coefficient and its first and second-order quantities $C_p^{(1)} = C_{po}^{(1)} + C_{pl}^{(1)}$
 $f = \omega c_o / U$, ϕ is the disturbance velocity potential (equation 1)
 $g(x,y)$ = wing oscillation amplitude function
 g = small disturbance dimension
 $H(x,y,t)$ = object surface equation
 $h(x,y)$ = airfoil surface function when angle of attack is 0°
 \bar{K} = ω / U
 k = reduced frequency, $\omega c_o / U = K c_o$
 M = inflow Mach number
 $\bar{N} = \frac{\gamma + 1}{2}$
 $n = \tan X_s / M$
 t = time variable
 x, y, z = space coordinates
 $\bar{x}, \bar{y}, \bar{z}$ = dimensionless coordinates that take c_o as reference length
 $x_1^{(1)}(u, y, z)$ = magnitude of disturbance of ϕ_1
 $x_1^{(2)}, R x_1^{(2)}, I x_1^{(2)}$ = magnitude of disturbance of ψ_1 , its real component and imaginary component
 $x_1^{(2)} = R x_1^{(2)} + i I x_1^{(2)}$

LIST OF SYMBOLS (continued)

U	= inflow velocity
u	= disturbance coordinate
α_0	= mean angle of attack
β	= $\sqrt{M^2 - 1}$
γ	= adiabatic index of gas
θ	= oscillation angle $\theta_0 e^{i\omega t}$
θ_0	= angular [amplitude] of simple harmonic pitch oscillation
$\dot{\theta}$	= $\frac{\partial \theta}{\partial t}$
χ_s	= sweepback angle
δ	= thickness ratio
$M\delta$	= hypersonic similarity parameter
ω	= oscillation angular velocity
S	= wing area

I. FOREWORD

Because the performance of supersonic aircraft has gradually risen, the problem of dynamic derivatives and dynamic stability has received more and more attention. In recent years, the problem of unsteadiness of low aspect ratio thin wings has aroused great interest. Many articles have applied linear theory to solve this problem. As to the condition of low supersonic speed where Mach number is not too close to 1, linear theory can give comparatively accurate aerodynamic results, but at a Mach number that is fairly high, nonlinear effect variations are important. The linear theory can be viewed as completely solving the first-order problems towards relative thickness or angle of attack of the wing. In some literature they have computed a second-order solution, and point out that when Mach number is high, the second-order solution greatly improves the first-order solution.

The second order theory is a method of computing nonlinear effects and since Buseman's [2] two dimensional thin wing second-order theory was published, there has been great progress in the steady and unsteady theories of two-dimensional flows. Within this progress are works such as Landahl's method [4] which takes the form of the parameters in the two-dimensional results to express the three-dimensional effects. Naturally, this is only a weak three-dimensional effect, and cannot resolve the three-dimensional problem in the delta wing apex Mach cone.

At the same time, there has been a series of work on the three-dimensional steady flow second-order theories proving that second-order solutions are especially suitable to flight Mach numbers between the linear region and the high Mach number region.

Qian Fuxing et al [5], using high Mach numbers approximation, extend a series of steady three-dimensional treatment methods to unsteady flow, and concretely solve unsteady problems of the high Mach number transonic leading edge low aspect ratio wing.

This paper uses this method to compute the dynamic derivative of a flat delta wing that has angle of attack, makes comparison with results of related theories, and gives the accuracy and a suitable range of this method.

II. FUNDAMENTAL EQUATION

Consider a certain pointed leading edge low aspect ratio three-dimensional thin wing flying at a uniform supersonic velocity in static air and making small simple harmonic oscillations. The coordinate primary point is chosen at the mean position of the delta wing apex, x axis is in the same direction as the flow direction and the x , y and z form the right hand Cartesian coordinate system. t expresses time.

Due to longitudinal shock waves, the entropy change is the third-order small quantity of the thickness ratio and pitch angle. Therefore, considering the second-order, then the flow is isentropic and as a result is irrotational and has potential $\Omega(x, y, z, t)$. Now introducing disturbance potential Φ divided by free flow velocity U makes the standardization obtain a total velocity potential of:

$$\Omega(x, y, z, t) = U(x + \Phi(x, y, z, t)) \quad (1)$$

The second-order equation which is satisfied by disturbance potential Φ can be derived as follows [9]:

$$\begin{aligned} \Phi_{xx} + \Phi_{yy} - \beta^2 \Phi_{zz} - 2 \frac{M^2}{U} \Phi_{xt} - \frac{M^2}{U^2} \Phi_{tt} = M^2 \left[(\gamma - 1) \left(\Phi_x + \frac{1}{U} \Phi_t \right) \right. \\ \left. \times (\Phi_{xx} + \Phi_{yy} + \Phi_{zz}) + 2(\Phi_x \Phi_{xx} + \Phi_y \Phi_{yy} + \Phi_z \Phi_{zz}) + \frac{2}{U} (\Phi_x \Phi_{xt} \right. \\ \left. + \Phi_y \Phi_{yt} + \Phi_z \Phi_{zt}) \right] \end{aligned} \quad (2)$$

The object surface equation can be written as:

$$z = H(x, y, t) \quad (3)$$

The object surface tangential condition is:

$$\Phi_x = -\frac{1}{U} H_t + (1 + \Phi_x) H_x + \Phi_z H_z \quad (4)$$

The pressure coefficient can be written as:

$$C_p = -2\Phi_x - 2\Phi_t/U + \beta^2 \Phi_z^2 - \Phi_x^2 - \Phi_y^2 + 2M^2 \Phi_x \Phi_t/U + M^2 (\Phi_t/U)^2 \quad (5)$$

Now considering under conditions of high Mach number, we introduce the following parameters:

$$\left. \begin{aligned} \xi = x/c_0, \quad \eta = y/\sigma c_0, \quad \zeta = z/\mu c_0, \quad \tau = kUt/c_0 \\ k = \omega c_0/U, \quad \bar{h} = H/\delta c_0, \quad f(\xi, \eta, \zeta, \tau) = \Phi/gc_0 \end{aligned} \right\} \quad (6)$$

Here c_0 is the maximum chord of the wing, σ is the dimension of the existing area of disturbance in the span direction, ω is the oscillation angular velocity, k is the reduced frequency and g is the dimension of small disturbances. With equation (6) substituted in equations (2) and (4) we can obtain

$$\begin{aligned} & k^2 f_{\tau\tau} + 2(1 + gf_{\tau})kf_{\tau\tau} + 2g\sigma^{-2}kf_{\tau}f_{\tau\tau} + 2g\mu^{-2}kf_{\tau}f_{\tau\tau} \\ & + (1 + 2gf_{\tau})f_{\tau\tau} + 2g\sigma^{-2}f_{\tau}f_{\tau\tau} + 2g\mu^{-2}f_{\tau}f_{\tau\tau} \\ & = \{1/M^2 - (\gamma - 1)g(kf_{\tau} + f_{\tau})\}(f_{\tau\tau} + \sigma^{-2}f_{\tau\tau} + \mu^{-2}f_{\tau\tau}) \end{aligned} \quad (7)$$

and the boundary conditions are

$$f_{\tau} \Big|_{\zeta = \frac{\delta}{\mu} \bar{h}} = \frac{\mu \delta}{g} [k\bar{h}_{\tau} + (1 + gf_{\tau})\bar{h}_{\tau} + (g/\sigma^2)f_{\tau}\bar{h}_{\tau}] \quad (8)$$

In formula (8) we can assume $g \ll 1$, $g \ll \sigma$ based on a small disturbance. If we assume $k \ll 1$, then we have $\mu \delta / g \sim 1$. When M number is fairly high, for the pointed thin object, we can consider:

$$\begin{aligned} & \text{(or)} \\ & \mu \sim \delta \quad \text{或} \quad \mu \sim 1/M \end{aligned}$$

Therefore:

$$\begin{aligned} & \text{(or)} \\ & g \sim \delta^2 \quad \text{或} \quad g \sim \delta/M \end{aligned} \quad (9)$$

When formula (9) is substituted into expressions (7) and (8), and dropping the μ^2 (that is M^{-2}) terms of magnitude, we obtain:

$$\begin{aligned} & k^2 f_{\tau\tau} + 2kf_{\tau\tau} + 2g\sigma^{-2}kf_{\tau}f_{\tau\tau} + 2g\mu^{-2}kf_{\tau}f_{\tau\tau} + f_{\tau\tau} + 2g\sigma^{-2}f_{\tau}f_{\tau\tau} + 2g\mu^{-2}f_{\tau}f_{\tau\tau} \\ & = \{1/M^2 - (\gamma - 1)g(kf_{\tau} + f_{\tau})\}(\sigma^{-2}f_{\tau\tau} + \mu^{-2}f_{\tau\tau}) \end{aligned} \quad (10)$$

$$f_{\tau} \Big|_{\zeta = \frac{\delta}{\mu} \bar{h}} = (\mu \delta / g)(k\bar{h}_{\tau} + \bar{h}_{\tau} + (g/\sigma^2)f_{\tau}\bar{h}_{\tau}) \quad (11)$$

When equations (10) and (11) are changed back to the original

coordinates by means of formula (6), they become:

$$\begin{aligned} & \Phi_{yy} + \Phi_{zz} - M^2 \Phi_{xx} - 2(M^2/U) \Phi_{xz} - (M^2/U^2) \Phi_{xx} \\ & = M^2[(\gamma - 1)(\Phi_x + \Phi_z/U)(\Phi_{yy} + \Phi_{zz}) + 2(\Phi_y \Phi_{xy} + \Phi_z \Phi_{xz}) \\ & + (2/U)(\Phi_y \Phi_{yz} + \Phi_z \Phi_{yz})] \end{aligned} \quad (12)$$

$$\Phi_x|_{y=0} = (H_x/U + H_x + \Phi_y H_y - H \Phi_{xx})_{y=0} \quad (13 a)$$

or

$$\Phi_x|_{y=0} = (H_x/U + H_x + \Phi_y H_y - H \Phi_{xx})_{y=0} \quad (13 b)$$

Comparing equations (12) and (2) we can then see that under conditions of high Mach number and normal reduced frequency, it is reasonable to drop the terms for the disturbance velocity in the x-direction and for its derivative of x.

With disturbance potential Φ of the second-order theory divided into the two components of steady and unsteady, when the wing near the mean angle of attack α_0 makes simple harmonic oscillations of small amplitude, its unsteady component can again be written into the corresponding simple harmonic oscillation formula:

$$\Phi = \phi(x, y, z) + \theta_0 e^{i(\omega t - \bar{k}z)} \psi(x, y, z) \quad (14)$$

Again with ϕ and ψ developed according to the thickness ratio:

$$\phi = \phi_0(\delta) + \phi_1(\delta^2) + o(\delta^3) \quad (15)$$

$$\psi = \psi_0(1) + \psi_1(\delta) + o(\delta^2) \quad (16)$$

Here $\bar{k} = \omega M^2 / U \beta^2$, and when M is high $\bar{k} = \omega / U$, while $\phi_0, \phi_1, \psi_0, \psi_1$ satisfy the following equations:

$$\square \phi_0 = 0 \quad (17)$$

$$\square \phi_1 = M^2(M^2(\bar{N} - 1)\phi_{0xx}^2 + \phi_{0yy}^2 + \phi_{0zz}^2)_{,x} \quad (18)$$

$$\square \psi_0 = 0 \quad (19)$$

$$\square \psi_1 = 2M^2(M^2(\bar{N} - 1)\phi_{0xx}\psi_{0xx} + \phi_{0yy}\psi_{0yy} + \phi_{0zz}\psi_{0zz})_{,x} \quad (20)$$

In the equations, $\square = \frac{\partial^2}{\partial y^2} + \frac{\partial^2}{\partial z^2} - M^2 \frac{\partial^2}{\partial x^2}$. The boundary

conditions are:

$$\phi_{0z}|_{z=0} = h_z + \alpha_0 \quad (21)$$

$$\phi_{1z}|_{z=0} = h_z \phi_{0z} - (h + \alpha_0 x) \phi_{0xz}|_{z=0} \quad (22)$$

$$\psi_{0z}|_{z=0} = -e^{i\bar{K}x} (g_z + i\bar{K}g)|_{z=0} \quad (23)$$

$$\psi_{1z}|_{z=0} = e^{i\bar{K}x} (g\phi_{0xz} - g_z\phi_{0z}) + h_z\psi_{0z} - \psi_{0xz}(h + \alpha_0 x)|_{z=0} \quad (24)$$

In the equations, $h(x,y)$ and $g(x,y)$ indicate the shape and amplitude of oscillation of the object. Therefore the boundary equation for the object is:

$$H(x, y, t) = h(x, y) + \alpha_0 x - \theta_0 e^{i\omega t} g(x, y) \quad (25)$$

The corresponding pressure coefficients are:

$$C_p = C_p^{(0)} + C_p^{(1)} \quad (26)$$

$$C_p^{(0)} = C_{p_0}^{(0)} + C_{p_1}^{(0)}$$

$$C_p^{(1)} = C_{p_0}^{(1)} + C_{p_1}^{(1)}$$

$$C_{p_0}^{(0)} = -2\phi_{0xz}|_{z=0} \quad (27)$$

$$C_{p_1}^{(0)} = -2\phi_{1z} + M^2\phi_{0z}^2 - \phi_{0z}^2 - \phi_{0z}^2 - 2\phi_{0xz}(h + \alpha_0 x)|_{z=0} \quad (28)$$

$$C_{p_0}^{(1)} = -2\theta_0 e^{i(\omega t - \bar{K}x)} \psi_{0z}|_{z=0} \quad (29)$$

$$C_{p_1}^{(1)} = 2\theta_0 e^{i(\omega t - \bar{K}x)} [-\psi_{1z} + M^2\phi_{0z}\psi_{0z} - \phi_{0z}\psi_{0z} - \phi_{0z}\psi_{0z} + g\phi_{0xz}e^{i\bar{K}x} - \psi_{0xz}(h + \alpha_0 x)]|_{z=0} \quad (30)$$

III. PLK METHOD

The solution of ϕ_0 and ψ_0 of the first-order equation near the apex Mach line shows singularity, making the right sides of equations (18) and (20) disperse, and causing the second-order solution of ϕ_1 and ψ_1 to show even more serious singularity. In order to obtain applicable results, we must make disturbance towards the independent variable according to the PLK method in order to obtain a completely effective solution.

The general expression for the coordinates disturbance is:

$$x = u + x_1(u, v, z) + o(\delta^2) \quad (31)$$

In this expression, the disturbance variable is x_1 and its magnitude is δ . It is assumed that $x_1^{(1)}$ is the magnitude of disturbance in equation (18) and $x_1^{(2)} = K x_1^{(2)} + i_1 x_1^{(2)}$ is the magnitude of disturbance in equation (20). Therefore equations (17) through (20) become:

$$\square \phi_0 = 0 \quad (32)$$

$$\square \phi_1 = M^2(M^2(\bar{N} - 1)\phi_{0u}^2 + \phi_{0v}^2 + \phi_{0z}^2) + \phi_{0u}\square x_1^{(1)} + 2(\phi_{0uv}x_{1v}^{(1)} + \phi_{0uz}x_{1z}^{(1)} - M^2\phi_{0uu}x_{1u}^{(1)}) \quad (33)$$

$$\square \psi_0 = 0 \quad (34)$$

$$\square \psi_1 = 2M^2(M^2(\bar{N} - 1)\phi_{0u}\psi_{0u} + \phi_{0v}\psi_{0v} + \phi_{0z}\psi_{0z}) + \psi_{0u}\square x_1^{(2)} + 2(\psi_{0uv}x_{1v}^{(2)} + \psi_{0uz}x_{1z}^{(2)} - M^2\psi_{0uu}x_{1u}^{(2)}) \quad (35)$$

In the equations, $\square = \frac{\partial^2}{\partial y^2} + \frac{\partial^2}{\partial z^2} - M^2 \frac{\partial^2}{\partial u^2}$. The boundary

conditions are:

$$\phi_{0u}|_{z=0} = h_u + \alpha_u \quad (36)$$

$$\phi_{1u}|_{z=0} = \phi_{0u}x_{1u} - h_u x_{1u}^{(1)} - \alpha_u x_{1u}^{(1)} + \phi_{0v}h_v - (h + \alpha_u u)\phi_{0uu}|_{z=0} \quad (37)$$

$$\kappa\psi_{0u}|_{z=0} = -(g_u \cos \bar{K}u - \bar{K}g \sin \bar{K}u) \quad (38)$$

$$i\psi_{0u}|_{z=0} = -(g_u \sin \bar{K}u + \bar{K}g \cos \bar{K}u) \quad (39)$$

$$\kappa\psi_{1u}|_{z=0} = \kappa\psi_{0u}x_{1u}^{(2)} - i\psi_{0u}x_{1u}^{(2)} - (\phi_{0v}g_v - g\phi_{0vv} - g_u x_{1u}^{(2)})\cos \bar{K}u - g_u x_{1u}^{(2)}\sin \bar{K}u + h_v \kappa\psi_{0v} - (h + \alpha_u u)\kappa\psi_{0uu} \quad (40)$$

$$i\psi_{1u}|_{z=0} = i\psi_{0u}x_{1u}^{(2)} - \kappa\psi_{0u}x_{1u}^{(2)} - (\phi_{0v}g_v - g\phi_{0vv} - g_u x_{1u}^{(2)})\sin \bar{K}u + g_u x_{1u}^{(2)}\cos \bar{K}u + h_v i\psi_{0v} - (h + \alpha_u u)i\psi_{0uu} \quad (41)$$

The partial differential equations satisfied by $x_1^{(1)}$ and $x_1^{(2)}$ are:

$$\begin{cases} \frac{\partial x_1^{(1)}}{\partial u} = M^2(\bar{N} - 1) \frac{\partial \phi_0}{\partial u} \\ \frac{\partial x_1^{(1)}}{\partial y} = -M^2 \frac{\partial \phi_0}{\partial y} \\ \frac{\partial x_1^{(1)}}{\partial z} = -M^2 \frac{\partial \phi_0}{\partial z} \end{cases} \quad (42)$$

$$\begin{cases} \frac{\partial x_1^{(2)}}{\partial u} = M^2(\bar{N} - 1) \left(\frac{\partial \phi_0}{\partial u} + \frac{\partial \psi_0}{\partial u} \frac{\partial^2 \phi_0}{\partial u^2} + \frac{\partial^2 \psi_0}{\partial u^2} \right) \\ \frac{\partial x_1^{(2)}}{\partial y} = -M^2 \left(\frac{\partial \phi_0}{\partial y} + \frac{\partial \psi_0}{\partial y} \frac{\partial^2 \phi_0}{\partial u \partial y} + \frac{\partial^2 \psi_0}{\partial u \partial y} \right) \\ \frac{\partial x_1^{(2)}}{\partial z} = -M^2 \left(\frac{\partial \phi_0}{\partial z} + \frac{\partial \psi_0}{\partial z} \frac{\partial^2 \phi_0}{\partial u \partial z} + \frac{\partial^2 \psi_0}{\partial u \partial z} \right) \end{cases} \quad (43)$$

They can be solved on the basis of the characteristics of ϕ_0 and ψ_0 near the apex Mach cone.

According to the works of Van Dyke [3], Qian Fuxing et al [5], we have

$$\phi_1 = M^2(\phi_0 \phi_{0,u}) - M^2 \bar{N} u \phi_{0,u}^2 + \phi_{0,u} x_1^{(1)} + \phi_1^{(0)} \quad (44)$$

$$\psi_1 = M^2(\phi_0 \psi_0)_u - M^2 \bar{N} u \phi_{0,u} \psi_{0,u} + \psi_{0,u} x_1^{(1)} + \psi_1^{(0)} \quad (45)$$

The equations which satisfy subsidiary solutions $\phi_1^{(0)}$ and $\psi_1^{(0)}$ are the homogeneous wave equations:

$$\square \phi_1^{(0)} = 0 \quad (46)$$

$$\square \psi_1^{(0)} = 0 \quad (47)$$

We need only solve ϕ_0 , ψ_0 , $\phi_1^{(0)}$ and $\psi_1^{(0)}$ and substitute them into equations (27) through (30) to be able to obtain the pressure coefficient. Then, we can obtain the lift coefficient and the moment of force coefficient with its integral.

IV. THE THREE-DIMENSIONAL FLAT WING OSCILLATING NEAR THE MEAN ANGLE OF ATTACK

In order to prove the dependability and applicability range of this theory, we must make some quantitative computations, using convenient and related theories and test results to make comparisons. Because to date we have not seen the test results of the dynamic derivatives of the three-dimensional wing in supersonic flight where the mean angle of attack is not zero, therefore there is no way to make comparisons with actual tests. The only way we can make comparisons is with the results of a flat delta wing compressed surface oscillating at low reduced frequency by D.D. Liu and W.H. Hui [6]. Therefore, we also computed this kind of test sample.

We consider a flat delta wing with supersonic leading edges near a certain angle of attack α_0 making low amplitude low frequency simple harmonic oscillation about a fixed point ($x=b$). In that case, $h(x,y)=0$ and $g(x,y)=x-b$ in equation (25), that is:

$$H(x, y, t) = \alpha_0 x - \theta_0 e^{i\omega t} (x - b)$$

Under conditions of low frequency oscillation, $k \ll 1$, and the boundary conditions of equations (17) through (20) become:

$$\phi_{00}|_{x=0} = \alpha_0$$

$$\psi_{00}|_{x=0} = -(1 + i\bar{K}(2x - b))$$

$$\psi_{10}|_{x=0} = (1 + i\bar{K}x)(x - b)\phi_{000} - \psi_{000}\alpha_0 x|_{x=0}$$

The analytical expression which under these conditions can find the solution for ϕ_0 and ψ_0 is substituted into equations (42) and (43), solving:

$$x_1^{(1)} = -\frac{\alpha_0 M}{(1 - n^2)^{1/2}} ((\bar{N} - 1)u + Mny) \quad (48)$$

$$x_1^{(2)} = -\frac{2\alpha_0 M}{(1 - n^2)^{1/2}} ((\bar{N} - 1)u + Mny) \quad (49)$$

$$x_1^{(3)} = \frac{\alpha_0 \bar{K} M (x - Mny)((1 - 2n^2)x + Mny)}{(1 - n^2)^{3/2}} \quad (50)$$

From equations (44) and (45) we obtain:

$$\begin{aligned} \kappa \psi_{1/2}^{(0)}|_{z=0} = & -\frac{2\alpha_0 M}{\pi} \left\{ \frac{n(u^2 - M^2 y^2)^{1/2}(2u - b)}{u^2 - M^2 n^2 y^2} + \frac{(\bar{N} - 1)}{(1 - n^2)^{1/2}} \right. \\ & \left. + \frac{1}{(1 - n^2)^{1/2}} \left(\cos^{-1} \frac{un - My}{u - Mny} + \cos^{-1} \frac{un + My}{u + Mny} \right) \right\} \quad (51) \end{aligned}$$

$$\begin{aligned} \kappa \psi_{1/2}^{(1)}|_{z=0} = & -\frac{2\alpha_0 M \bar{K}}{\pi} \left\{ n(u^2 - M^2 y^2)^{1/2} \left(-\frac{3u^2 - 2b}{u^2 - M^2 n^2 y^2} + \frac{2}{1 - n^2} \right) \right. \\ & + \frac{3u - b}{(1 - n^2)^{1/2}} \left(\cos^{-1} \frac{un - My}{u - Mny} + \cos^{-1} \frac{un + My}{u + Mny} \right) \\ & - \frac{2n^2 - 1}{(1 - n^2)^{3/2}} \left[(u - Mny) \cos^{-1} \frac{un - My}{u - Mny} \right. \\ & \left. + (u + Mny) \cos^{-1} \frac{un + My}{u + Mny} \right] - \frac{\pi}{(1 - n^2)^{1/2}} \left[\left(\frac{1 - 2n^2}{1 - n^2} \right) \right. \\ & \left. \left. - 3(\bar{N} + 3)u + \frac{3n^2 - 2}{1 - n^2} Mny \right] \right\} \quad (52) \end{aligned}$$

From this we can numerically solve ψ_1 , and substituting it into equations (29) and (30), we find the pressure coefficient $C_p^{(1)}$. The pitching moment coefficient is:

$$C_m = \frac{1}{S C_\rho} \iint C_p (x - b) dx dy \quad (53)$$

As to the low amplitude simple harmonic oscillation, $\theta = \theta_0 e^{j\omega t}$, and therefore we have:

$$\frac{C_m}{\theta} = C_{m_0} + ikC_{m_i} = 2 \tan \chi_r \int_0^1 d\bar{x} \int_0^{2 \tan \chi_r} \frac{C_p}{\theta} (\bar{x} - \bar{b}) d\bar{y} \quad (54)$$

From this equation, we can know that there is a relationship between the dynamic derivative and the imaginary component of $\frac{C_m}{\theta}$, that is the imaginary component of $C_p^{(1)}/\theta$, thus:

When integrating, we see to it that the original singular line $x=My$ in plane $u-y$ becomes:

$$C_{m1} = -\frac{2 \tan \chi_s}{h} \int_0^1 d\bar{x} \int_0^{\tan \chi_s} \left[\frac{C_p^{(1)}}{\theta} \right]_{\tan(\bar{x}-\bar{b})} d\bar{y} \quad (55)$$

Thus we can obtain the dynamic derivative that was sought.

$$u = \left[1 + \frac{\alpha_s M}{(1 - \pi^2)^{1/2}} (\bar{N} - 1 + \pi) \right] My \quad (56)$$

V. RESULTS AND DISCUSSION

In the process of solving the second-order equation, we partially use a three-dimensional special approximation solution (the second term on the right side of equation (45)). We used the above mentioned method to carry out a large number of calculations regarding M from 2 to 8, angle of attack α_0 from 5° to 20° , sweepback angle from 20° to 63° , and pitching rotation axis position \bar{b} from 0 to 1.0. Representative results are drawn in Fig. 1 and Fig. 2. Moreover, Liu and Hui's results [6] which can provide results of a comparative curve and linear theory [5] are also drawn in the figures. Based on what we know, to date we have not seen related test data.

We can see from Fig. 1 and Fig. 2 that these results and the results of Liu and Hui tally on tendency and magnitude. In Fig. 1 a flat delta wing (aspect ratio 2) with a sweepback angle $\chi_s=63$ were compared with linear theory. It is evident that thickness or initial angle of attack play a reducing role towards the aerodynamic derivative.

Van Dyke [8] had in the second-order theory of axisymmetric bodies utilized the point of divergence between the curves of change in the Mach number and the air stream and determined the applicable range of the second-order theory of flow about axisymmetric bodies to be approximately $M_\infty \leq 0.7$. In Fig. 1 of this text we can also see similar conditions. The larger

the sweepback angle becomes, the higher the Mach number at initial divergence. We can say that under three-dimensional conditions, the applicable range of the second-order theory can reach $M\delta > 1.0$. Under conditions of normal sweepback angle, it can be applicable up to $M\delta = 1.0$. Between $M\delta \approx 0.7 \sim 1.0$, the primary nonlinear effect can be estimated by the second-order theory.

The assumed applicable range of high Mach number is $M \geq 3$, at Mach numbers of $2 \sim 3$, the error of the second-order solution can be somewhat large. But when computing the aerodynamic force and the dynamic derivative, we must add the second-order solution in the first-order solution. This first-order solution is a linear result. If the first-order solution employs a linear result not having the approximate accuracy of the high Mach numbers, even if the error of the low supersonic second-order equation is somewhat large, it can still improve on the original comparatively dependable linear results.

In the range of supersonic speed and low hypersonic speed, in order to raise the maneuverability and dynamic stability of the aircraft, we looked for some linear theory or semi-experiential piston theory on the calculation of dynamic derivatives, shock wave expansion method, Newtonian theory etc. having more dependable theoretical basis and a method suitable for engineering computations. What is primary is the thickness effect of the low aspect ratio wing and the influence of the mean angle of attack, and there is still the reduced frequency required to reach the range of $0 \sim 1$. These cannot make people satisfied in linear theory, especially when the Mach number is above 3.

Lastly, we should mention Comrade Han Yanliang. From start to finish he participated in the related large amount of

computation work for this text. In the process of writing this text we obtained assistance from Comrade Yan Meiyun. We express our gratitude.



Fig. 1. $C_{m\theta}$ with Mach number variations (Flat delta wing compressed surface).
Key: (a) Linear theory; (b) Theory in this paper; (c) Liu and Hui [6].

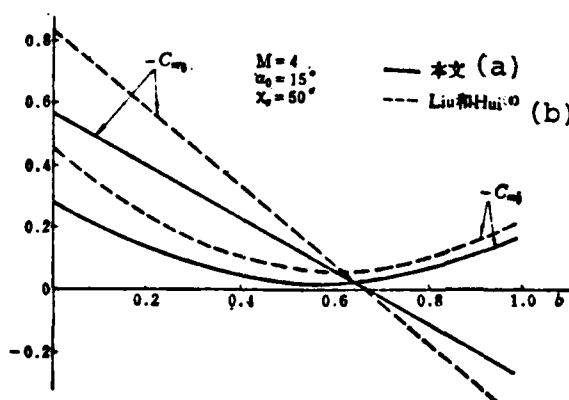


Fig. 2. $C_{m\theta}$ and C_L with b variations (Flat delta wing compressed surface).
Key: (a) This paper; (b) Liu and Hui [6].

Reference Literature:

- [1] Orlik-Rückemann K.J., Dynamic Stability Testing of Aircraft-Needs Versus Capabilities. Prog. Aerospace Sci. Vol. 16, No. 4, 1975.

Reference Literature:

- [2] Buseman A., Aerodynamischer Auftrieb bei Überschall Geschwindigkeit. Lufo. Bd. 12, Nr. 6, 1935.
- [3] Van Dyke M.D., A Study of Second-Order Supersonic Flow Theory. NACA Report 1981, 1952.
- [4] Landahl M.T., Unsteady Flow Around Thin Wings at High Mach Numbers. JAS. 1957, p. 33
- [5] Qian Fuxing, Hua Wei, Wang Quanwei, et al, "Unsteady Second-Order Theory for Supersonic and Hypersonic Three-Dimensional Thin Wing," Ke Xue Ji Shu Yan Jiu Bao Gao, Mechanics Institute, Academia Sinica, December, 1964.
- [6] Liu, D.D. and Hui, W.H., Oscillating Delta Wings with Attached Shock Waves. AIAA J. Vol. 15, No. 6, 1977.
- [7] Hui, W.H., Stability of Oscillating Wedge and Wings in Hypersonic and Supersonic Flows. AIAA J. Vol. 7, No. 8, 1969.
- [8] Van Dyke, M.D., Practical Calculation of Second-Order Supersonic Flow Nonlifting Bodies of Revolution, NACA TN 2744, 1952.
- [9] Van Dyke, M.D., Supersonic Flow Past Oscillating Airfoils Including Nonlinear Thickness Effects. NACA Rep. 1183, 1954.

EXPERIMENTAL INVESTIGATION OF INTERFERENCES OF TOP AND BOTTOM
SLOTTED WALLS AND THE EFFECTS OF SIDEWALLS IN A TRANSONIC
AIRFOIL WIND TUNNEL

Research Team on Airfoil
(Northwestern Polytechnical University)

Abstract

Pressure distribution on three RAE 104 airfoil models with 50mm, 100mm and 125mm chords respectively were measured in Northwestern Polytechnical University's transonic airfoil wind tunnel (also called wind tunnel 57). Results showed that when the open area ratio is 2%, the blockage interference of the wind tunnel practically vanishes.

Results from tests made on RAE 104 airfoil models under the three sidewall conditions of solid sidewalls, multilayered mesh plates without air exhaust and multilayered mesh plates with air exhaust showed: multilayered mesh plates without air exhaust caused the lift coefficients to be much lower than the values when there is no interference; when $M < 0.7$, use of a solid sidewall can cause the lift coefficients to basically reach the values when there is no interference; installment of a multilayered mesh plate with air exhaust can also cause the lift coefficients to basically reach the values when there is no interference.

A comparison between test results in this wind tunnel and those in the British NPL's 20 inch x 8 inch transonic tunnel is presented.

INTRODUCTION

With the continuous development of experimental research on transonic airfoils, there has also been much attention devoted to the research of transonic airfoil wind tunnel experimental technology abroad. But the experimental research on airfoils (especially transonic airfoils) in China is practically blank. In the past we did not have a high speed airfoil wind tunnel in China that could be used to develop our country's own work of experimental research on airfoils. For this reason, in 1976 we participated in rebuilding Canada's large wind tunnel [2] into a transonic airfoil wind tunnel. In this wind tunnel we successively carried out measurements of sidewall boundary layers [3] and flow field calibration [4]. The results were in accordance with experiment requirements.

During this period, the primary focus was the experimental research of top and bottom wall interference and sidewall influence. The test results clearly indicated that when the top and bottom wall open area ratio is 2%, it draws near to an open area ratio with no blockage interference. This is in agreement with the results for certain foreign slotted wall wind tunnels.

At the same time, we referred to the foreign method of resolving sidewall influence; we also carried out some experiments in this wind tunnel. But our work is only beginning and we still must make further attempts to work out the question of sidewall influence; some problems in test results when the angle of attack is fairly large and the Mach number fairly high must also be further resolved.

SYMBOLS

b = airfoil chord length

c = slot parameter, $c = -\frac{1}{\pi} \log_e \sin\left(\frac{\pi}{2} \sigma\right)$

SYMBOLS

- C_N = normal force coefficient
 C_P = pressure coefficient
 h = wind tunnel test section height
 l = distance between slots
 M = Mach number
 P = static pressure
 P_O = total pressure
 T = wind tunnel parameter, $T = \frac{1-c/h}{1+c/h}$
 V_∞ = mainstream velocity
 V_n = airflow velocity that is perpendicular to sidewall mesh plate
 $\bar{x} = \frac{x}{b}$ = corresponding coordinates of the airflow downstream of the airfoil leading edge
 σ = top and bottom slotted wall open area ratio
 a = angle of attack

Lower footnote:

- i = incompressible

I. TEST DEVICES

1. Wind Tunnel

The Northwestern Polytechnic University transonic wind tunnel is a blow down, intermittent type. The test section cross section is rectangular, 300mm high and 100mm wide. It is constructed by adding a two-dimensional insert section in an original three-dimensional wind tunnel; see Fig. 1.

The total length of the two-dimensional test section is 1050mm. Installed on the sidewall is a fixed model and a turnable disk which changes the angle of attack; on the turnable disk a stainless steel wire multilayered mesh plate or solid plate can be installed; see Fig. 2. The sidewall cavity air exhaust duct and the valve gate are interlinked with the

atmosphere (or vacuum pump), utilizing the pressure difference between the test section and the sidewall cavity to carry out sidewall air exhaust in order to eliminate sidewall influence. The 40% chord point of the model and the center of the turnable disk coincide, the distance between this point and the test inlet is 280mm.

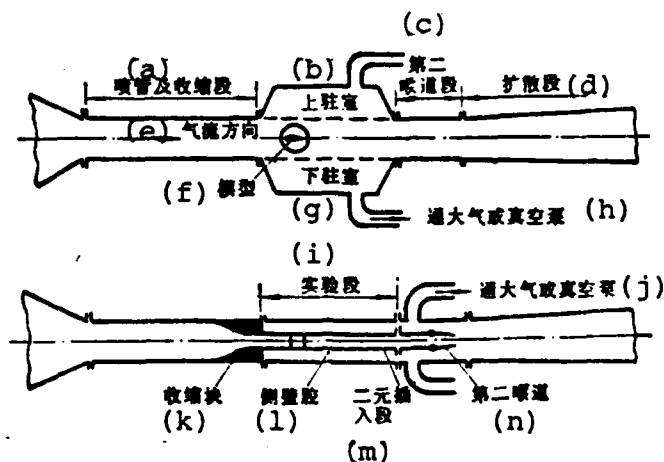


Fig. 1. Sketch of transonic airfoil wind tunnel.

Key: (a) Nozzle and converging section; (b) Upper stationary chamber; (c) Second throat section; (d) Diffusion section; (e) Airflow direction; (f) Model; (g) Lower stationary chamber; (h) To atmosphere or vacuum pump; (i) Test section; (j) To atmosphere or vacuum pump; (k) Converging place; (l) Side wall cavity; (m) Two dimensional insert section; (n) Second throat.

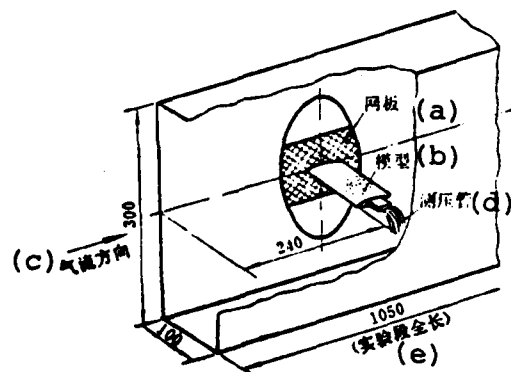


Fig. 2. Sketch of model position and sidewall air exhaust mesh plate.

Key: (a) Mesh plate; (b) Model; (c) Airflow direction; (d) Pressure calibration tube; (e) Test section length.

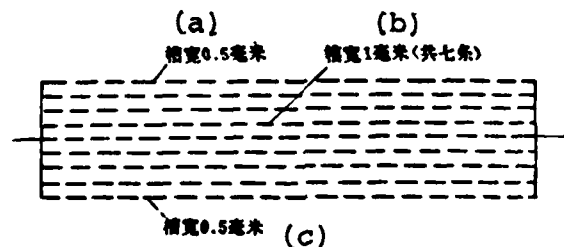


Fig. 3(a). Sketch of top and bottom slotted walls.

Key: (a) Slot width 0.5mm; (b) Slot width 1mm (altogether 7 slots); (c) Slot width 0.5mm.

The top and bottom of the test section are slotted walls, each has seven 1mm wide and two 0.5mm wide slots; see Fig. 3(a). The slot length is 910mm. Using the method of glue paper we can cover some of the slots and change the open area ratio. The

slotted wall expansion angle is 30'. On the outside of the top and bottom slotted walls are the stationary chambers. They can carry out stationary air exhaust through the air exhaust ducts.

Empty wind tunnel flow field calibrations show that the greatest difference between the local Mach number in the model region and the average Mach number is less than ± 0.005 .

2. Inspection Measurement Devices

The wind tunnel is equipped with a pressure circulation inspection system, including SYD-1 digital pressure sensor, XJ-100 circulation inspection measurement device, and LS-5 digital recorder. Pressure sensor precision is 0.2~0.3%.

3. Measurement of Mach Number

To change the open degree of the second throat we can make the continuous variation of the Mach number between 0.4~0.85, the stationary chamber air exhaust can raise the Mach number to 1.0. By the static pressure of the stationary chamber measurement we compute the inflow Mach number of the wind tunnel. Experiments show that the root mean square error of Mach number measurement is less than 0.0013.

II. MODEL

The chord lengths of the three RAE 104 airfoil models used in the tests were 50, 100 and 125mm respectively. The corresponding degrees of blockage were 1.7%, 3.3% and 4.2% respectively. The pressure measurement holes on the model are distributed at 10mm intervals on both sides of the center cross section. Table 1 gives the coordinates of the pressure measurement holes. The inside diameter of the pressure measurement holes is 0.8mm.

(c)	孔号 (a)	x × 100		
		125	100	50
上表面	前缘 (b)	0	0	0
	1	0.2	0.2	5
	2	1	1	20
	3	5	5	50
	4	10	10	60
	5	20	20	70
	6	30	30	80
	7	45	40	
	8	50	45	
	9	55	50	
	10	60	55	
	11	65	60	
	12	75	65	
	13	80	70	
	14	85	75	
	15	92	80	
	16	96	90	
			95	

(e)	孔号 (d)	x × 100		
		125	100	50
下表面	1	0.5	0.5	10
	2	2	2	20
	3	10	5	40
	4	15	15	90
	5	25	30	
	6	35	45	
	7	45	60	
	8	55	70	
	9	70	80	
	10	75	90	
	11	85		
	12	95		

Table 1. Coordinates of pressure measurement holes in the three Rae 104 wing models.

Key: (a) Hole number; (b) Leading edge; (c) Top surface; (d) Hole number; (e) Bottom surface

The model was machined by Beijing Great Wall Machine Factory.

III. BLOCKAGE INTERFERENCE TEST METHOD AND RESULTS

In the high speed wind tunnel, because of the compressibility influence, the amount of tunnel wall interference greatly increases. At the same time, the Mach number at high speed is an important parameter. Therefore, to define and do what is possible to eliminate blockage interference influence then appears to be very important.

The most ideal method is to take a series of wall plates with different open area ratios to conduct tests, requiring that the wall plates are able to systematically change slot width and slot spacing. The test results that are obtained can be compared with the test results without interference that were obtained in the large wind tunnel of the small model. Thus we define the open

area ratio without blockage interference.

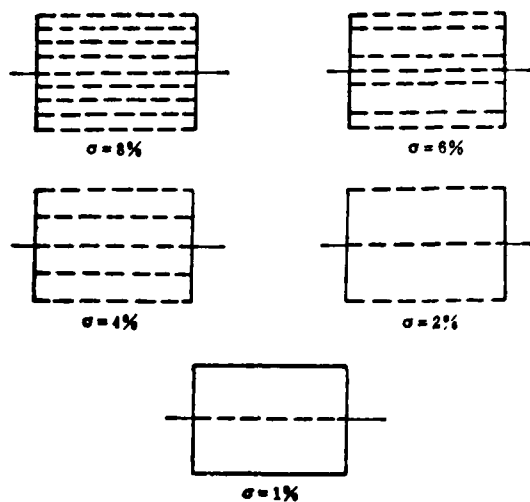


Fig. 3(b). Sketch of five open area ratios of slotted walls that were used.

Table 2.
Key: (a) Wall; (b) Slot number.

(a) 壁	(b) 槽 数	σ	T
1	$7 + 2 \left(-\frac{1}{2} \right)$	0.08	0.917
2	$5 + 2 \left(-\frac{1}{2} \right)$	0.06	0.928
3	$3 + 2 \left(-\frac{1}{2} \right)$	0.04	0.863
4	$1 + 2 \left(-\frac{1}{2} \right)$	0.02	0.690
5	1	0.01	0.640

At present, this wind tunnel does not have the conditions to systematically and simultaneously change slot width and slot spacing, but we use glue paper to paste over some of the slots

to change the open area ratio. The several open area ratios used in the tests are shown in Fig. 3(b). Table 2 shows the corresponding parameter value of each wall plate.

During the 1950's, England's NPL carried out a large amount of experimental research on related tunnel wall interference of slotted wall wind tunnels [5], and tried to find a set of methods to research wind tunnel wall interference. Because at present we have no large airfoil wind tunnel in China, therefore we basically used the method of the NPL to define wind tunnel blockage interference. If we use some models that are geometrically similar under conditions of different open area ratios in the same wind tunnel (or under a different T value) to conduct tests, we measure the pressure of different models on certain corresponding points. Under normal conditions, if the wall plate is not an open area ratio without interference then when the pressure of corresponding points on different models is the same, the corresponding inflow Mach numbers are different; conversely, if the wall plate has an open area ratio without interference, then when the pressure of corresponding points on different models is the same, the corresponding inflow Mach numbers also should be identical.

When the model has an angle of attack it is difficult to resolve the influence of the blockage interference with the lift interference from the tests. Therefore, the model angle of attack during blockage interference in the tests is zero.

The concrete method in this test is to take five kinds of slotted wall open area ratios, respectively measure the pressure distribution on three RAE 104 similar models of different chord lengths under conditions of zero angle of attack, and draw the pressure distribution curve, as shown in Fig. 4. We take the pressure value at the corresponding points on each

model (for example $\bar{x}=35\%$), and draw the $P/P_0 \sim M_\infty$ curve, as shown in Fig. 5. Then in each group of curves we take the same P/P_0 value (for example $P/P_0=0.525$), turning to draw the curve of M_∞ with changes in σ and T , as Fig. 6(a) and Fig. 6(b) show. By the above mentioned figures we can obtain that the open area ratio without blockage interference is approximately 1.6% and the corresponding wind tunnel parameter is approximately 0.67.

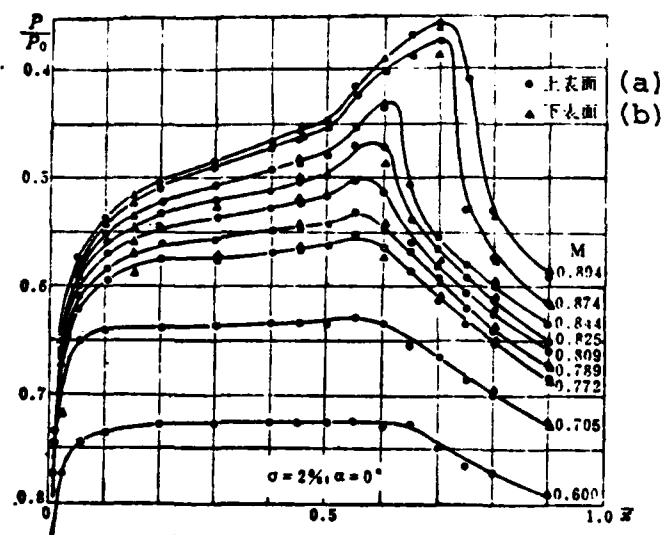


Fig. 4. Curve of pressure distribution of a $b=100$ model when Mach number is different.
Key: (a) Top surface; (b) Bottom surface.

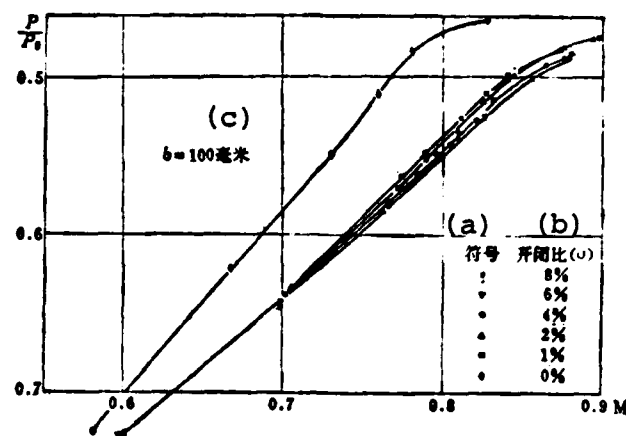


Fig. 5. Curve of pressure at point $x=0.35$ with Mach number variations, when there are different open area ratios.
Key: (a) Symbol; (b) Open area ratio; (c) $b=100\text{mm}$.

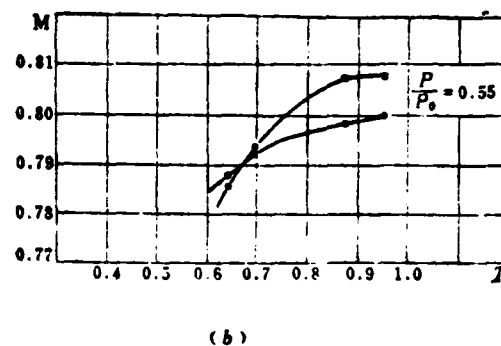
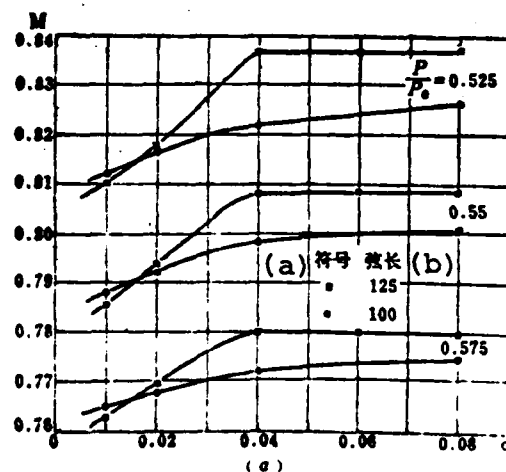


Fig. 6.
(a) Curve of variation of Mach number with σ , when airfoil surface pressure is consistent.
Key: (a) Symbol; (b) Chord length.

(b) Variation of Mach number with T , when airfoil surface pressure is consistent.

The parameters of slotted walls without interference that were obtained from numerous tests of England's NPL are shown in Table 3. We can see that the T value of slotted walls without blockage interference of wind tunnel 57 coincides with the general pattern.

Table 3

Wind Tunnel	Wall #	Slot #	Slot Width(mm)	Slot Distance(mm)	σ	T
NPL 20"x8" wind tunnel	4	3	0.915	67.6	0.016	0.69
NPL 18"x14" wind tunnel						0.52
ARC 7.5"x3"	H	2	1.524	38	0.04	0.70
Beijing Poly-Technical University wind tunnel 57	4	$1+2\left(\frac{1}{2}\right)$	1	50	0.02	0.69

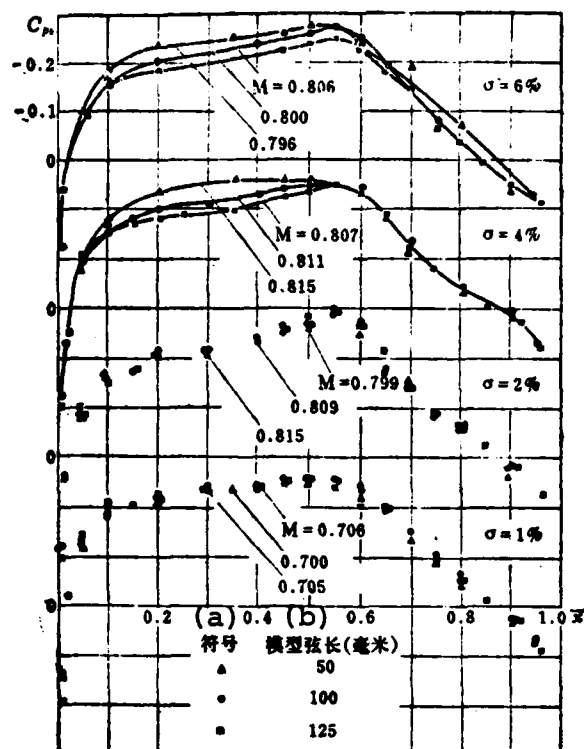


Fig. 7. Curve of pressure distribution of similar models with three different chord lengths, when there is different σ .
Key: (a) Symbol; (b) Model Chord Length (mm).

According to the "Data Comparison Method" in reference [6], Fig. 7 gives the curves of the pressure distribution of the three models when the open area ratios are 1%, 2%, 4% and 6%, and $C_{pi} = C_p \sqrt{1-M_\infty^2}$ was used in order to eliminate the differences arising from different Mach numbers in the test. It is evident from the figure that when the open area ratio is 1% and 2%, the pressure distribution curve of the three models coincide fairly well; but when the open area ratio is 4% and 6%, the curves then separate and assume the appearance of excessively open slotted walls. Thus it is evident that at an open area ratio of 1% and 2% both are close to a condition of no

blockage interference. We also can see from Table 2 that the T value of the wind tunnel when there are these two open area ratios all are near the T value of no blockage interference.

Based on the above results, we decided on a slotted wall open area ratio of 2%.

IV. INFLUENCE OF SIDEWALL AIR EXHAUST

The two-dimensional model is supported on the two sidewalls of the test section, and the influence of the sidewall boundary layer possibly ruins the two-dimensional nature of the flow, particularly when the Mach number and angle of attack are fairly large. The counter pressure gradient on the airfoil increases causing the boundary layer to separate at the junction of the model and the tunnel wall, and causing this influence to be even more prominent. There are many methods for eliminating the sidewall boundary layer influence. Among them, the method of boundary layer control is taken as the most effective. In recent years, Canada, America, England, Holland and other countries have all adopted this method and obtained success. Canada's NAE 15"x16" two-dimensional high Reynolds number wind tunnel adopted the method of sidewall mesh plates and added air exhaust to successfully resolve the problem of the two-dimensional nature of the flow, and caused the lift coefficient to raise. West Germany's DFVLR's BWT [7] also had conducted tests on the three different sidewall conditions of smooth solid walls, porous walls without air exhaust and porous walls with air exhaust. The results indicated that installing porous mesh plates without air exhaust cannot improve the lift properties,

it is not even as good as smooth solid walls; but porous mesh plates carrying out air exhaust can improve lift properties.

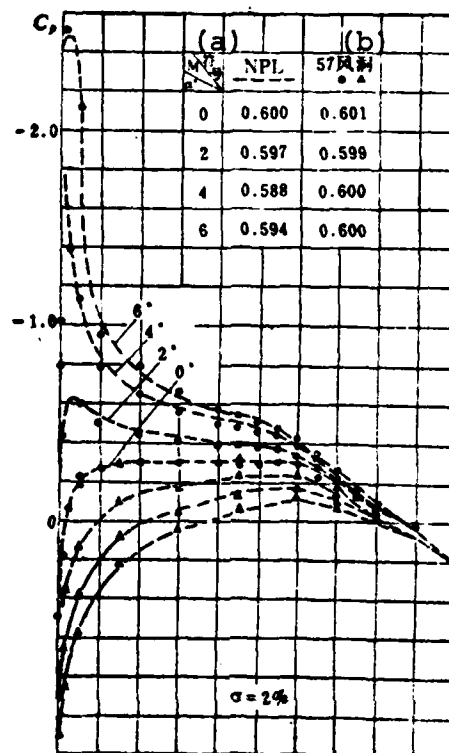


Fig. 8. Curve of pressure distribution with angle of attack α variations, when the device has solid side-walls.

Key: (a) Symbol; (b) Wind tunnel 57.

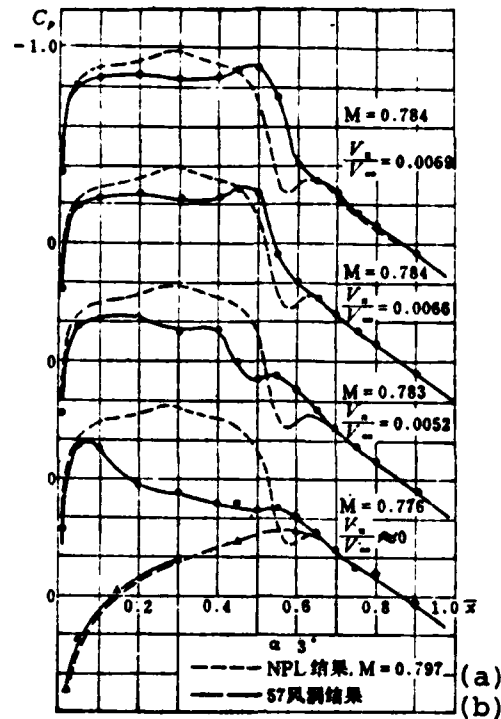


Fig. 9. Curve of pressure distribution with variations in the amount of sidewall air exhaust.
Key: (a) NPL results; (b) Wind tunnel 57 results.

We also carried out tests on three different sidewall conditions of solid sidewall, multilayered mesh plates with air exhaust and without air exhaust. Figure 8 gives the curves of pressure distribution with variation in angle of attack for smooth solid wall conditions when $M=0.6$. From the figure we can see that the results tally well with the NPL results. Figure 9 gives the curve of pressure distribution when $M \approx 0.78$ and the sidewall is a mesh plate adopting different amounts of air exhaust. In the figure, the amount of air exhaust is expressed as V_n/V_∞ , its definition is:

$$\frac{V_{\bullet}}{V_{\bullet}} = \frac{W_{\bullet}^{(1)} A}{W_{\bullet}^{(2)} A_{\bullet}^{(3)}} \quad (2) \quad (3)$$

Key:

(1) Exhaust;

(2) Main;

(3) Mesh.

In the formula, W_{exhaust} and W_{main} , respectively, are the mass flow exhausted through the breather mesh plate and the main flow in the test section; A and A_{mesh} , respectively, are the flow through area of the test section and the mesh plate.

From the above figures we can clearly see that the pressure distribution curve of the installed sidewall mesh without air exhaust is very low. With an increase in the amount of air exhaust, the curve gradually rises, showing that the air exhaust plays an important role. However, there is still a slight disparity with the NPL results, which awaits continued research hereafter to be resolved. Figure 10 gives the comparative curves of the pressure distribution of three different sidewall conditions. From the figure it is evident that the results of the sidewall equipped with mesh plate without air exhaust are even poorer than those of solid walls. This agrees with the test results of West Germany's BTW.

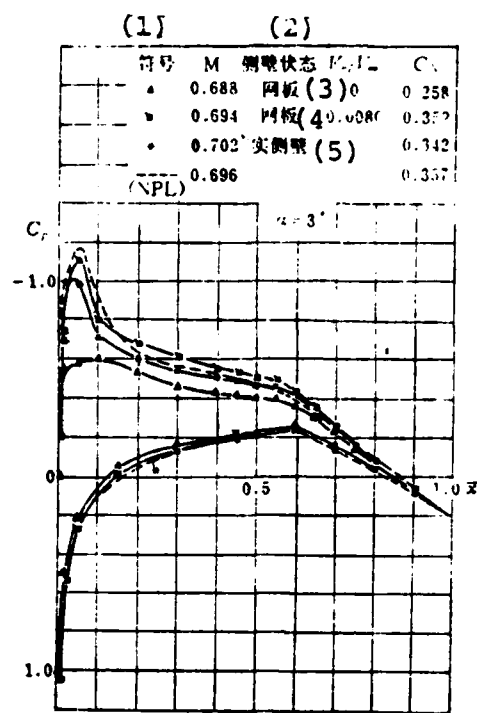


Fig. 10. Curve of pressure distribution of three different sidewall conditions.
Key: (1) Symbol; (2) Sidewall condition; (3) and (4) Mesh plate; (5) Solid sidewall.

From our test results we see that when $M < 0.7$, smooth solid walls already basically conform to test requirements. Hereafter when we do tests we can consider that it is not necessary to add mesh plates and air exhaust systems; in this way we can make tests even more simple and convenient.

Figure 11 comprehensively gives the normal force curves of three different sidewall conditions when $M=0.4, 0.6, 0.7$ and 0.8 , and makes comparisons with the NPL results. The C_N values in the figure are all obtained by the pressure distribution curve integral. By the numerous test results of the above mentioned figures we again see that sidewall boundary layer control, namely the effect of air exhaust, is especially even more obviously advantageous when Mach number and angle of attack are comparatively large.

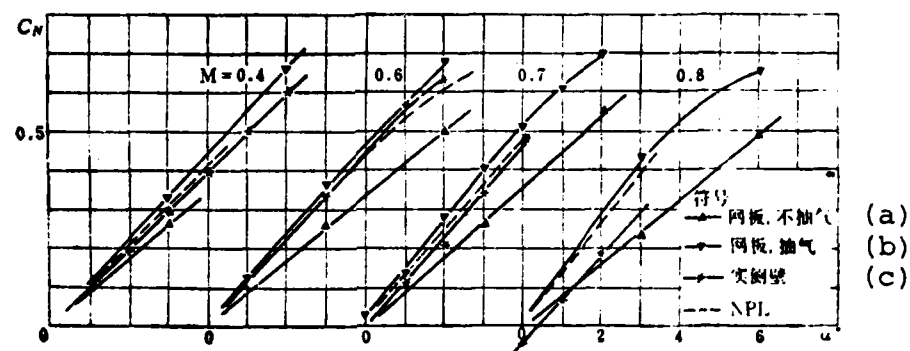


Fig. 11. Curve of $C_N \sim a$ with three different sidewall conditions.
Key: (a) Mesh plate with no air exhaust; (b) Mesh plate with air exhaust; (c) Solid sidewall.

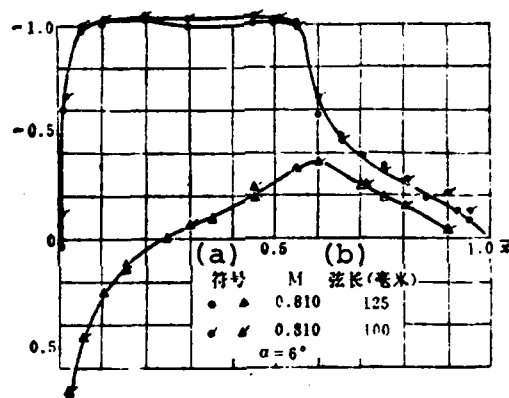


Fig. 12. Comparison of pressure distribution of models with different chord lengths, when $\sigma = 2\%$.
Key: (a) Symbol; (b) Chord Length (mm).

V. LIFT DISTURBANCE

We carried out tests with two models where chord lengths are 100mm and 125mm under conditions of open area ratio of 2% and with Mach numbers as identical as possible. Figure 12 gives the comparative curves of the test results. We can see that the pressure distribution curves of different models are basically identical. Seeing it from this point of view, we should say that

we already basically eliminated lift disturbance, but we can say that in light of the value of the pressure coefficient the results have some differences from the NPL results. In the future, we will further experiment on this point when we experiment using other models.

VI. STATIONARY CHAMBER CONDITIONS

Additionally, we made some related comparative tests of pressure distributions when the top and bottom chambers were connected and when separated. Figure 13 gives some of the first test results. Generally speaking, whether or not the stationary chambers were linked does not have a large influence on the test results.

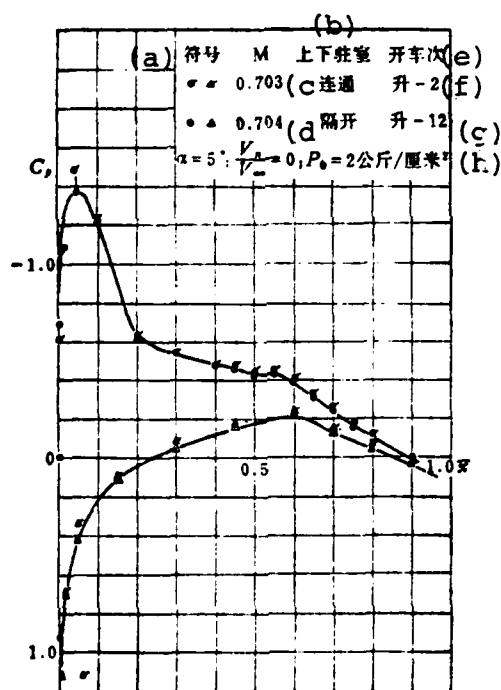


Fig. 13. Influence of top and bottom chamber linkage condition on pressure distribution.

Key: (a) Symbol; (b) Top and bottom chamber; (c) Linked; (d) Separated; (e) Set time; (f) Lift-2; (g) Lift-12; (h) kg/cm².

Those participating in the work of this research question are: Zhang Naiping, Yang Ye, Zhang Yuehui, Wang Dahai, Su Yuexi and others. We obtained energetic support from Comrades Pu Jiachen, Xi Yonglan and Wang Xiaoli. The wind tunnel construction and design work was primarily completed by Comrade He Jiaju, and others.

Reference Literature:

- [1] E.W.E. Rogers, C.J. Berry and R.F. Cash, Tests at High Subsonic Speeds on a 10 per cent Thick Pressure-plotting Aerofoil of RAE 104 Section. ARC. R & M 2863, 1956.
- [2] L.H. Ohman, D. Brown, The NAE High Reynolds Number 15"x60" Two-Dimensional Test Facility, Descriptions, Operating Experiences and Some Representative Results. AIAA Paper 71-293.
- [3] Xi Bei Gong Ye Da Xue Xi Xing Ke Ti Xiao Zu: Yi Xing Feng Tong De Fu Mian Ceng Ce Liang He Ji Suan [Northwestern Polytechnical University Research Group on Airfoil: Boundary Layer Calibration and Computation of Airfoil Wind Tunnels], 1977.
- [4] Xi Bei Gong Ye Da Xue Yi Xing Ke Ti Xiao Zu: 57 Tong Feng Liu Chang Xiao Liang [Northwestern Polytechnical University Research Group on Airfoil: Flow Field Calibrations of Wind Tunnel 57], 1978.
- [5] H.H. Pearcey, C.S. Sinnott and J. Osborne, Some Effects of Wind Tunnel Interference Observed in Tests on Two-Dimensional Aerofoils at High Subsonic and Transonic Speeds. AGARD Report 296. 1959.
- [6] J.D. Lee, G.M. Gregorek and K.D. Korkan: Testing Techniques and Interference Evaluation in the OSU Transonic Airfoil Facility AIAA 78-1118.
- [7] E. Stanewsky, W. Puffert, R. Müller: Der Transsonische Windkanal des Instituts für Aerodynamik der DFVLR, Eichung der modifizierten Meßstrecke und Vergleichsmessungen am Profil. Braunschweig. 1978.
- [8] Xi Bei Gong Ye Da Xue Yi Xing Ke Ti Xiao Zu: Kua Yin Su Yi Xing Shi Yan De Ji Ge Wen Ti [Northwestern Polytechnical University Research Group on Airfoil: Several Problems of Transonic Airfoil Tests], 1973.
- [9] D.W. Holder, R.J. North and A. Chinneck, B. Sc. Experiments with Slotted and Perforated Walls in a Two-Dimensional High-Speed Tunnel, ARC R&M 2955.

THE BIPARAMETRIC CYCLE COUNT METHOD AND THE PRINCIPLE OF SIMPLIFICATION

Research Team on Aircraft Load Spectrum
Penned by Jiang Zuguo

Abstract

Working out the load spectrum plays an important part in determining the fatigue life of the aircraft structure. Therefore, selection of the counting method and determination of the principle of simplification are two outstanding problems in drawing up the operational load spectrum of a fighter.

In the early 1970's, the NLR method was put forward by the Dutch NLR. From the point of view of the counting principle, this method corresponds to the stress-strain delaying loop and can give real expression to fatigue loads sustained on the aircraft; as viewed from the principle of simplification, it is a simplification principle of invariable mean value. Based on the NLR method, we have proposed the simplification principle of the variable mean value and two-wave method.

Through a great deal of practical measurement and investigation, this paper gives a typical random load mechanism of a fighter for 50 flight hours. Taking this as the initial data, we used two counting methods and four simplification principles for load spectra calculations, and corresponding life estimations were completed. Moreover, the contrast tests in groups for the six different load spectra have been carried out with satisfactory results. These results have confirmed that our theoretical analysis is useful for working out the load spectrum of the fighter with the counting method and the principle of simplification.

I. PREFACE

The accuracy of aircraft fatigue tests and life estimates to a large extent depend on the authenticity of load spectrum. There are two completely different methods to work out load spectrum: power spectrum and counting methods [1,2,3]. If the stochastic load-time mechanism (such as gusts of wind, random

vibrations, etc.), then we can use the power spectrum technique, and we can also use the counting method. However, the fighter plane maneuvering load mechanism is an unsteady stochastic process, and we generally use the counting method. As a result, the selection of the counting method and the determination of the principle of simplification become two outstanding problems in whether or not fighter plane load spectrums actually reflect the fatigue loads sustained by the aircraft.

There are already more than ten kinds of counting methods. When working out load spectrum, which method is actually good and which simplification principle is appropriate for use? These questions await final resolution both domestically and abroad. However, outside China, its tendentiousness is very obvious. In the early 1970's, Holland's space navigation research laboratory proposed the NLR method [4,5]. The counting principle of this method is the range pair-mean value counting method. This text calls it the biparametric cycle count method. The fixed mean value principle is what this text calls the principle of simplification. The range pair-mean value counting method (or rainflow method) has been adopted by countries[1,2,6,7], and is already used in the new determination of the F-104G aircraft fatigue life.

From the counting principle we can see that the NLR method is better than other counting methods; but from the principle of simplification we see that the mechanical foundation is not ample. Therefore, on the basis of the NLR method (that is, the constant mean value simplification principle), considering the distinguishing features of the fighter aircraft fatigue load and the influence of average stress on damage, we propose the principle of simplification of the variable mean value and the two-wave methods.

This text, by means of actual examples, carries out

comparisons of various load spectrums drawn up on different counting methods and principles of simplification and from these determines the counting methods and simplification principles which have fairly good authenticity in order to provide a basis for working out aircraft load spectrums from now on.

II. BIPARAMETRIC CYCLE COUNT METHOD

In ten odd counting methods, from the number of the parameter that was counted we come to see that they can be divided into two major categories: single parametric method and biparametric method. All the peak value types, penetrating level types, and some certain range types all belong to the single parametric method. Range pair-mean value counting methods belong to the biparametric method. If the rainflow method counts the mean values at the same time as counting the ranges, then its counting result is completely the same as the range pair-mean value counting method. Therefore, if we don't particularly explain, we call the range pair-mean value counting method and the rainflow method the biparametric cycle count method.

The counting process of the biparametric cycle count method is divided into two stages: the first stage counts the full cycle ranges S_r and the corresponding mean values S_m which are in the center (see Fig. 1(a)). After going through the first counting stage, what is remaining is the time mechanism of the diffusion-convergence condition, the half-cycle ranges S_r and the corresponding mean values S_m are counted according to the simple range-mean value counting method (see Fig. 1(b)). The flow chart of this counting method is shown in Fig. 2.

What the biparametric cycle count method counts is load cycles, and at the same time counts the two parameters (range and mean value) that can fully determine fatigue load. Moreover, it is consistent with stress-strain delay loop[9,10]. These

characteristics are not possessed simultaneously by any single parametric counting method. Therefore, the biparametric cycle count method can more authentically reflect all the fatigue load and fatigue damage of aircraft than all single parametric methods.

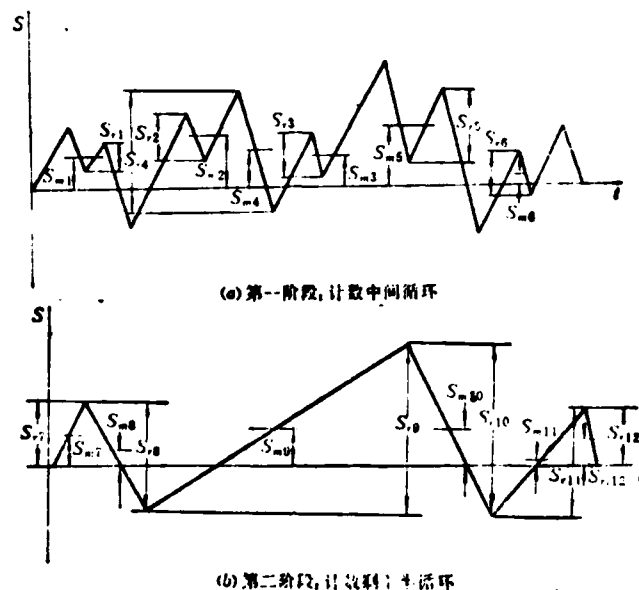


Fig. 1. Counts of biparametric cycle count method.

Key: (a) First stage: counting intermediate cycles; (b) Second stage: counting remaining half-cycles.

III. PRINCIPLE OF SIMPLIFICATION OF VARIABLE MEAN VALUE AND TWO-WAVE METHOD

We use the biparametric cycle count method to conduct counting of certain load mechanisms, and they were not at all equivalent to the usable load spectrums which were worked out. If we want to work out the load spectrums we must also conduct simplification treatment on counting results according to certain simplification principles. Here, we primarily introduce two kinds of principles of simplification.

1. Principle of Simplification of Variable Mean Value

Before we discuss the principle of simplification of variable mean value, we will first briefly discuss the principle of simplification of constant mean value.

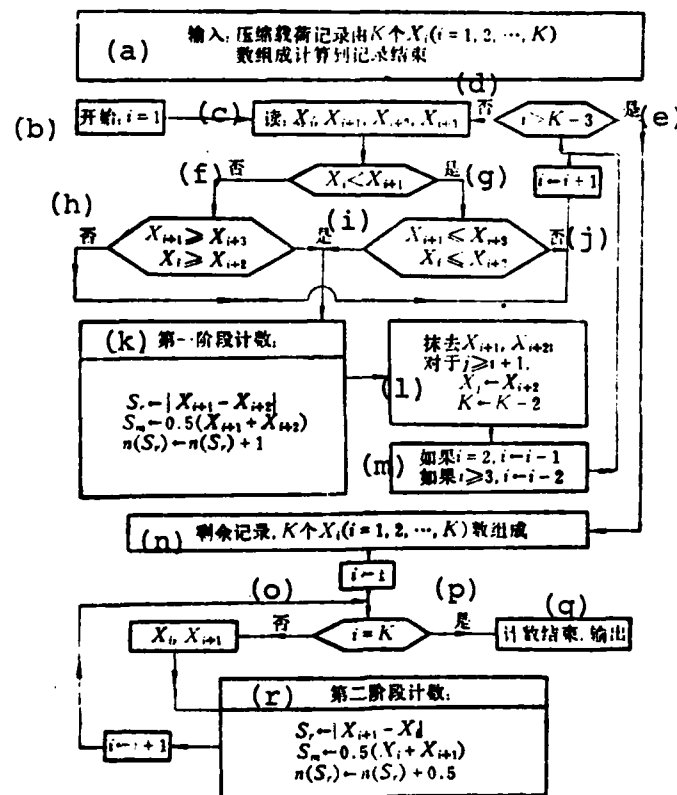


Fig. 2. Flow chart of biparametric cycle count method.

Key: (a) Input; compression load record composed of K number of X_i ($i=1, 2, \dots, K$) to compute recorded

conclusions: (b) Beginning; (c) Read; (d) No; (e) Yes; (f) No; (g) Yes; (h) No; (i) Yes; (j) No; (k) First phase counting; (l) Erase...as to ...; (m) If...if...; (n) Remaining record...number composition; (o) No; (p) Yes; (q) Counting conclusion, output; (r) Second phase counting.

The so-called principle of simplification of constant mean value refers to after the load mechanism are counted according to the biparametric count method, seeking the total

arithmetic mean \bar{S}_M of each mean value S_{mi} , all the mean values are simplified towards \bar{S}_M , and range S_r is fixed and invariant. In order to consider the variation range of the mean value, at the same time we seek the total standard difference σ_{mo} . The load spectrums worked out according to the constant mean value simplification principle are called the constant mean value load spectrums.

The principle of simplification of the variable mean value refers to after counting according to the biparametric counting method, seeking the corresponding average mean value S_{mj} of each level of range S_{rj} , the range is fixed and invariant. At the same time, we seek the standard difference σ_{mj} , that is:

$$S_{mj} = \frac{\sum_{i=1}^{v_{j1}} S_{mi} + 0.5 \sum_{i=1}^{v_{j2}} S_{mi}}{v_{j1} + 0.5 v_{j2}} \quad (1)$$

$$\sigma_{mj} = \sqrt{(S_{mi}^2)_j - (\bar{S}_{mi})^2} \quad (2)$$

In the formulae:

S_{mj} is the weighted mean value that corresponds to S_{rj} , $j=1, 2, \dots, n$: here n is the range group of numbers.

S_{rj} is the set of central values of the j range ($S_{r_{lower}} \sim S_{r_{higher}}$).

S_{mi} is the i average value in the j range set : $i=1, 2, \dots, v_{j1}$ (or v_{j2});

v_{j1} is the frequency of the whole cycle in the j range set;

v_{j2} is the frequency of a half-cycle in the j range set;

$(S_{mi}^2)_j$ is the weighted mean value of the square of S_{mi} in the j range set.

The load spectrum that is drawn up according to the principles of simplification of the variable mean value is called

the variable mean value load spectrum. When we find the frequency distribution of range S_{rj} of the variable mean value spectrum, mean value S_{mj} , and standard difference σ_{mj} , we can still use the matrix to carry out computations[11].

From the above, we can see that the range of the variable mean value spectrum and the constant mean value spectrum are the same, what is different is that the constant mean value spectrum is given according to the method of total weighted average, and its mean value is invariant; the variable mean value spectrum is given according to the method of partial weighted mean value, and its mean value is variable (see Fig. 3). Actually, the fatigue loads that fighter planes sustain in flight not only have amplitude that continually change, but the mean values also continually change. Therefore the principle of simplification of the variable mean value can actually reflect the fatigue load and the fatigue damage that the fighter plane sustains even more than the principle of simplification of constant mean value.

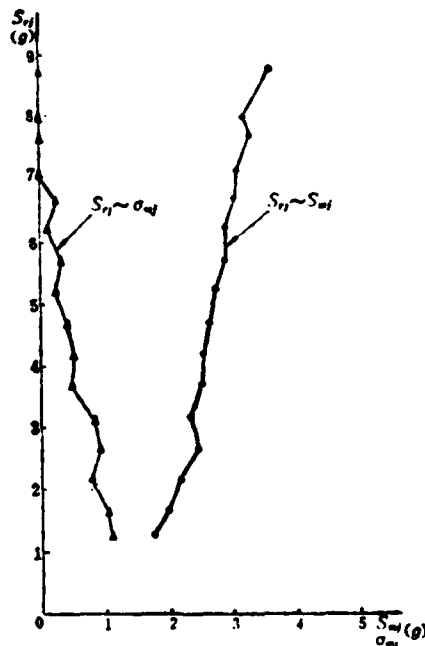


Fig. 3. The relationship between range S_{rj} , range S_{mj} , and standard difference σ_{mj} .

2. Principle of Simplification of the Two-Wave Method

Before we discuss the principle of simplification of the two-wave method, we will first briefly discuss the principle of simplification of equal damage.

The so-called principle of simplification of equal damage refers to after counting according to the biparametric count method, based on the principle of equal damage[12], we can simplify the stress cycle under any mean stress S_{mi} to a certain fixed mean stress, such as a simplification reaching the total mean value \bar{S}_M of the mean value. By revising Goodman's figure (Fig. 4), its equivalent range S_{req} can be given by the following formula:

$$S_{req} = S_{ri} \left(\frac{\sigma_b - \bar{S}_M}{\sigma_b - S_{mi}} \right) \quad (3)$$

In the formula, S_{ri} and S_{mi} respectively are the range and mean value before simplification. σ_b is the static stretch intensity of the material.

Because fighter plane fatigue load takes maneuvering as primary and is not symmetrical in relation to 1 g, this then causes the degree of irregularity of the load to be fairly large. Practice proves that the influence of the degree of load irregularity on fatigue damage is quite large[13]. Therefore it is necessary to divide the fighter plane fatigue load into primary wave and secondary wave[10]. The comparatively large load wave motion that is primarily caused by maneuvering movement is called the primary wave, and the comparatively small load wave motion that is primarily caused by gusts of wind or preparation movements is called the secondary wave. Moreover, we consider that these two categories of load come from two different mother bodies,

and therefore we separately carry out statistical drawing of the spectrum. This dividing of the fighter plane load into primary wave and secondary wave to carry out the principle of simplification is called "the two-wave method".

The concrete method of computation is as follows: following the counting of the stochastic load mechanism according to the biparametric count method, we use certain criteria to divide the counting results into primary wave and secondary wave [12].

Primary wave spectrum computation: making its minimum value $S_{\min} = l_g$ corresponding stress, the range carries out equivalent conversion according to the equal damage principle. In formula (3), \bar{S}_m is converted into S_{meq} and letting $S_{\text{meq}} = S_{\min} + 0.5 S_{\text{req}}$, by substituting into formula (3) we can obtain through arrangement:

$$S_{\text{req}} = \frac{S_{\text{ri}}(\sigma_b - S_{\min})}{\sigma_b - S_{\min} + 0.5 S_{\text{ri}}} \quad (4)$$

Secondary wave spectrum computation: the computation is completely identical with the equal damage spectrum, that is, we first find the total mean value \bar{S}_m of all the secondary waves and the range carries out equivalent conversion according to the equal damage principle. The computation formula is the same as in formula (3).

The putting together of the primary wave spectrum and the secondary wave spectrum is the load spectrum two-wave method.

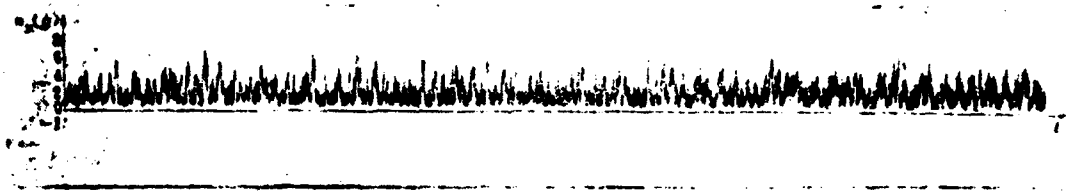


Fig. 5. Fighter plane 50 hours typical random spectrum

The fighter plane 50 hours typical random spectrum was taken as the primary input, two different counting methods (using the fatigue counting method to represent the single parametric method) and four different principles of simplification were used, and we computed the following five kinds of load spectrums: fatigue counting method load spectrum, constant mean value load spectrum, variable mean value load spectrum, equal damage load spectrum, and biparametric method load spectrum. The results of the computations are shown in Fig. 6.

Based on the random spectrum and the five load spectrums that were computed, we carried out grouped contrast tests on a PC160N hydraulic servo fatigue test aircraft[15]. The test material is the LY12-CZ aluminum alloy made in China. A center porous plate specimen is used, stress concentration coefficient $K_t=4$, specimen width $W=45\text{mm}$, thickness $B=2.5\text{mm}$, at the $1g$ stress level used in the tests the corresponding stress is $\sigma_{1g}=3.55\text{kg/mm}^2$, and the load corresponding to $1g$ is $P_{1g}=320\text{kg}$. The loading order, except for random spectrum, is low-high-low, the loading method is tension-compression and loading frequency is 5 hertz. The number of each group of specimen is 6. See Fig. 7 for the form and dimensions of the specimen. Contrast test results are shown in Table 1.

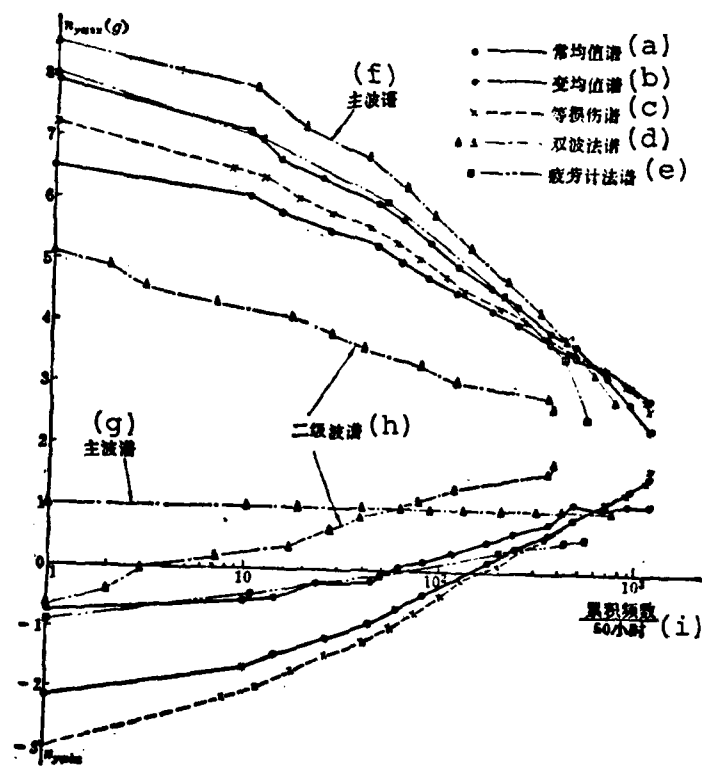


Fig. 6. Five load spectrums that were computed.

Key: (a) Constant mean value spectrum; (b) Variable mean value spectrum; (c) Equal damage spectrum; (d) Two-wave method spectrum; (e) Fatigue counting method spectrum; (f) Primary wave spectrum; (g) Primary wave spectrum; (h) Secondary wave spectrum; (i) Accumulated frequency.

50 hours

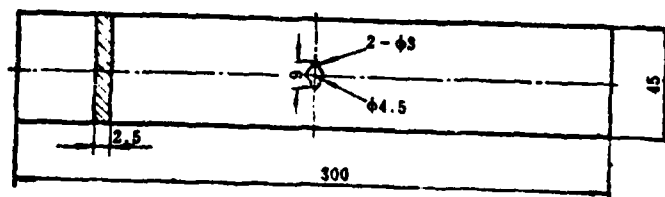


Fig. 7. Specimen

		(h)	(i)	(j)	(k)	(l)	(m)	(n)
(a)	谱 型	每加载周 期循环数	序 号	试 件 号	破坏循环数	加载周数 (块数)	疲劳寿命 (小时)	几何平均寿命 (小时)
(b)	随机谱	1106	1	54	66665	60.3	3011	2787
			2	14	56650	51.2	2561	
			3	50	65201	59.0	2948	
			4	03	53111	48.3	2415	
			5	04	60283	54.5	2725	
			6	05	69208	62.6	3129	
(c)	疲劳计法谱	547	1	27	52800	96.5	4816	4011
			2	52	37562	68.7	3433	
			3	60	43071	78.7	3937	
			4	28	44026	80.5	4021	
			5	23	43213	79.0	3950	
(d)	常均值谱	1105	1	49	97879	88.6	4429	3737
			2	2	71702	67.6	3380	
			3	8	91267	82.6	4130	
			4	42	78060	70.6	3532	
			5	9	79158	71.6	3582	
			6	19	76952	69.6	3482	
(e)	变均值谱	1105	1	10	58230	52.7	2635	2778
			2	41	65910	59.6	2882	
			3	55	69252	62.7	3134	
			4	36	69294	62.7	3135	
			5	18	56708	51.3	2566	
			6	25	51293	46.4	2321	
(f)	双波谱	1106	1	11	64632	58.4	2922	2863
			2	47	56916	51.5	2573	
			3	51	58211	52.7	2632	
			4	3	63518	57.4	2872	
			5	43	63542	57.5	2873	
			6	22	74568	67.4	3372	
(g)	等值谱	1106	1	39	41589	37.6	1880	1712
			2	37	36100	32.6	1632	
			3	48	35950	32.5	1625	

Table 1. Overview table of contrast test results.
Key: (a) Spectrum type; (b) Random spectrum; (c) Fatigue counting method spectrum; (d) Constant mean value spectrum; (e) Variable mean value spectrum; (f) Two-wave method spectrum; (g) Equal damage spectrum; (h) Number of each added load period cycle; (i) Order number; (j) Specimen number; (k) Ruined cycle number; (l) Added load period number; (m) Fatigue life (hours); (n) Geometric average life (hours);

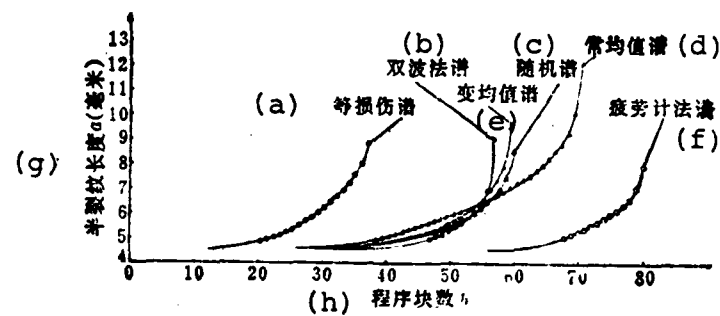


Fig. 8. Curve of crack expansion of typical specimen.

Key: (a) Equal damage spectrum; (b) Two-wave method spectrum; (c) Random spectrum; (d) Constant mean value spectrum; (e) Variable mean value spectrum; (f) Fatigue counting method spectrum; (g) Semi-crack length a (mm); (h) Sequence block number h .

We processed each group of test results according to the data processing method of grouped contrast tests. The survival frequency is taken as 50%, the degree of confidence is taken as 95% and after examinations of F and t we obtained the deduced comparison of the body of specimen life of each group. The results are shown in Table 2. The curve of crack expansion that represents the typical specimen of each load spectrum is as shown in Fig. 8.

At the same time, we also used Miner's linear cumulative damage principle to approximately estimate the fatigue life of five kinds of load spectrum[16]. The results are shown in Table 2.

In the fatigue counting method spectrum, because the total cumulative frequency number of the positive pole is more than that of the negative pole, therefore when doing fatigue tests and conducting life estimates, after pairing each corresponding positive and negative pole, the surplus positive pole frequency pairs with lg[17].

From Table 1, Table 2, Fig. 6, and Fig. 8 we can see that:

(1) The dispersion for the number of breakdown cycles for each group of specimens is relatively small.

(2) The variable tendency of the tested life of each load spectrum and the estimated life basically agree.

(3) The life-times given by the four kinds of load spectrums which are worked out by using the biparametric count method are even closer to the random spectrum life than the life that the single parametric fatigue count method spectrum gives.

(4) In the four load spectrums of the biparametric count method, as compared with the random spectrum, the life of the constant mean value spectrum is the longest, the life of the equal damage spectrum is the shortest, the life of the variable mean value spectrum and the random spectrum are practically identical, and the two-wave method spectrum also is comparatively close to the life of the random spectrum.

Why can the fatigue life that each load spectrum gives have these differences? Reference [18] carries out detailed analysis from the three areas of load spectrum, fatigue, and crack. Here, for convenience of discussion, we give the comparisons of the extreme values of each load spectrum (Table 3), and briefly analyze as follows:

(1) The fatigue counting method is a non-cyclic single parametric counting method. It does not possess those advantages of the biparametric cycle count method discussed in the above section. At the same time, according to our understanding, the fatigue counting method is a type of quasi-cumulative counting which is processed according to the cumulative counting method. As to a fighter plane with a fairly large degree of

irregularity and a non-symmetrical load mechanism, the fatigue counting method cannot only neglect some comparatively low secondary waves, but can also do so for some comparatively high secondary waves and even some primary waves. In the 50 hour random spectrum, the total cumulative frequency number of its counting becomes 547 times from random spectrum 1106 times. Additionally, the level differences of the fatigue counting method that we used are comparatively large, the level value of each level takes the prescribed minimum. These factors then cause the life of the fatigue counting method spectrum to be approximately 44% higher than the random spectrum life.

(2) Comparing the amplitude value (or range) and the mean value, the contribution of the amplitude value on the damage plays an important role. Holland's NLR method spectrum is simplified according to the constant mean value, its amplitude value (or range) is fixed and invariant, and it basically and realistically reflects the information of the variation of amplitude value in the random load mechanism. It is seemingly feasible but after all it does not consider the influence of the mean value variation on the damage. Moreover, after simplification the load spectrum possesses symmetry. Comparing it with the random spectrum, the largest maximum value in the load cycle reduces, the smallest minimum value increases (according to the absolute value, similarly hereinafter) and the degree of distortion is fairly large, causing the constant mean value spectrum life to be approximately 34% higher than the random spectrum life.

(3) The range of the variable mean value spectrum is the same as the constant mean value spectrum. At the same time, we consider the influence of the mean value (variation). Their largest load and smallest load as well as the frequency of each load that emerges is almost the same as those of the random spectrum, basically keeping the original features of the

random spectrum load size and frequency. What is different, however, is that it takes the random loading sequence of the random spectrum and changes it into a loading sequence according to the low-high-low arrangement. Because we take 50 hours as one loading period, the period number (that is, the loading sequence block number) is far greater than 20, and basically belongs to a short period of loading. Therefore the influence of the loading sequence on the life is very small. Its life is then extremely close to the random spectrum life, only 0.3% lower.

Table 2. Life Comparison of each load spectrum

(a) 内 容	(b) 谱 型	(c) 随 机 谱	(d) 疲 劳 计 法 谱	(e) 常 均 值 谱	(f) 变 均 值 谱	(g) 等 损 伤 谱	(h) 双 波 法 谱
(i) 估计寿命 L_i (小时)			3628	3180	2641	2486	2654
(j) 试验寿命 L_i (小时)		2787	4011	3737	2778	1712	2863
(k) L_{50i}/L_{50m}			1.237~1.674	1.171~1.534	无显著差别 (n)		无显著差别 (o)
(l) L_i/\bar{L}_{ran} (子样)			1.439	1.341	0.997	0.614	1.027
(m) $(\bar{L}_i - \bar{L}_{ran})/\bar{L}_{ran}$			43.9%	34.1%	-0.3%	-38.6%	2.7%

(p) ● L_i —各种载荷谱子样的几何平均寿命;

(q) ● L_{50i} 、 L_{50m} —分别为各种程序谱和随机谱母体中值寿命。

Key: (a) Content; (b) Spectrum type; (c) Random spectrum; (d) Fatigue count method spectrum; (e) Constant mean value; (f) Variable mean value; (g) Equal damage; (h) Two-wave method spectrum; (i) Estimated life L_i (hours); (j) Tested life L_i (hours); (k) L_{50i}/L_{50} random; (l) \bar{L}_i/\bar{L}_{ran} random(sub); (m) $(\bar{L}_i - \bar{L}_{ran})/\bar{L}_{ran}$; (n) No marked difference; (o) No marked difference; (p) ① L_i is the geometric average life of each load spectrum sub type; (q) ② L_{50i} and L_{50} random separately are the central body life of each ordered spectrum and random spectrum.

Table 3. Comparison of the extreme values of each load spectrum.

(a) 谱型	(b) 50小时	(c) 累积频数	(d) 最大的极大值 $n_{\max\max}(g)$	(e) 最小的极小值 $n_{\min\min}(g)$	$n_{\min} < 0$ 的次数 (f)
(g) 随机谱		1106	8.0(1次)(o)	-0.8(2次)(v)	52
(h) 疲劳计法谱		547	8.0(1次)(p)	-0.75(1次)(w)	33
(i) 常均值谱		1105	6.53(1次)(q)	-2.12(1次)(x)	113
(j) 变均值谱		1105	7.94(1次)(r)	-0.71(1次)(y)	44
(k) 等损伤谱		1106	7.24(1次)(s)	-2.94(1次)(z)	123
(l) 双波 (m) 主波谱		741	8.52(1次)(t)	1.0(741次)(aa)	0
(n) 二级波谱		365	5.16(1次)(u)	-0.67(1次)(bb)	3

Key: (a) Spectrum type; (b) 50 hours; (c) Accumulated frequency number; (d) Largest extreme value $n_{\max\max}(g)$; (e) Smallest extreme value $n_{\min\min}(g)$; (f) Number of times of $n_{\min} < 0$;
 (g) Random spectrum; (h) Fatigue count method spectrum; (i) Constant mean value spectrum; (j) Variable mean value spectrum; (k) Equal damage; (l) Two-wave method; (m) Primary wave spectrum; (n) Secondary wave spectrum; (o) (1 time); (p) (1 time); (q) (1 time); (r) (1 time); (s) (1 time); (t) (1 time); (u) (1 time); (v) (2 times); (w) (1 time); (x) (1 time); (y) (1 time); (z) (1 time); (aa) (1 time); (bb) (1 time).

It can be seen from this that the variable mean value spectrum that we proposed both maintains the advantages of the NLR method spectrum (using the range to count a mean value count method, the range of the spectrum after simplification is fixed and invariant etc.), and overcomes the shortcomings of the NLR method spectrum (we considered the influence of mean value variation, the non-symmetry that the spectrum possesses after simplification, small distortion degree, etc.). Moreover, the test facilities that we now have also make it easy to realize the loading requirements of this spectrum. Therefore, the principle of simplification of variable mean value is most appropriate for working out the load spectrum that the fighter plane uses.

(4) Although the equal damage spectrum uses the principle of equal damage to consider the influence of mean value, yet because this spectrum does not consider the characteristics of fighter plane fatigue loads, we also used the revised Goodman

figure. The spectrum after simplification is even larger than the degree of distortion of the constant mean value spectrum, the amplitude value of each level of load is much larger than that of the random spectrum, and therefore its life is only approximately 61% of the random spectrum life.

(5) Even though the largest maximum value and the smallest minimum value in the primary wave spectrum of the two-wave method both are bigger than in the random spectrum, it does not realistically maintain the original features of the random spectrum as does the variable mean value spectrum. Yet it is converted according to the principle of equal damage and at the same time considers the special points that the fighter plane load takes the maneuvers as primary, does not have symmetrical load, and its load has a large degree of irregularity, etc. Therefore its life and random spectrum are also fairly close (approximately 3% higher) and as a result using it to work out the fighter plane load spectrum is also feasible and effective.

From the above discussion we can see that the variable mean value spectrum and the equal damage spectrum in the same way use mathematical methods (i.e. weighted average) for treatment, and the differences in the results are very large. However, the variable mean value spectrum and the two-wave method spectrum use completely different principles of simplification for treatment so that the differences in obtained results are very minute, and are also closest to the random spectrum. This then tells us that the applications of any mechanical principle and mathematical method all have certain premises and conditions. Therefore when determining a principle of simplification, what is important does not lie in the employed simplification method itself, but when adopting a certain simplification method the degree of distortion of its spectrum type should be reduced to the minimum. In this way, we can then cause the damage of the simplified spectrum to be close to the actual damage of the

random spectrum. This is also to say, we certainly must choose the principle of simplification according to the true conditions of a certain type of random spectrum. For example, even though the constant mean value spectrum and the equal damage spectrum are not suitable for working out the fighter plane usable load spectrum, as to random load mechanism such as gusts of wind, stochastic vibration, etc. that have symmetry, these two kinds of principles of simplification are perhaps feasible.

Even though variable mean value spectrums and two-wave method spectrums corresponding to other spectrums are more able to authentically reflect fighter plane fatigue load, yet these two spectrums also have their own inadequacies. The ranges of variable mean value spectrums and mean values are both variable and belong to the probability distribution of binary variables; statistical analysis is fairly complex. The criteria of the two-wave method spectrum divided waves possess certain indeterminateness, and frequently we must concretely determine them on the basis of experience. At the same time, in the above several spectrums, the computation of the two-wave method spectrum is the most complex.

V. CONCLUDING REMARKS

By means of the theoretical analysis of the biparametric cycle count method and the principle of simplification of variable mean value and two-wave method as well as the comparison of test results and estimated results, we can conclude the following two points:

(1) The load spectrum that is worked out using the biparametric cycle count method is even closer to the actual random load spectrum than the load spectrum that is worked out using the single parametric count method.

(2) In the four load spectrums worked out by the biparametric cycle count method, as to the fighter plane, the life that is given by the variable mean value and two-wave method is the closest to the life of the random spectrum. As a result, the principle of simplification of the variable mean value and the two-wave method is the most suitable for working out the fighter plane usable load spectrum.

On this basis, we propose:

(1) When working out the usable load spectrum for each type of aircraft, it is best to use the biparametric cycle count method;

(2) When working out the usable load spectrum for fighter planes, it is best to use the principle of simplification of the variable mean value or the two-wave method.

References

- [1] Jong Moo Lee, Experimental Random Loading Characteristics in Structure Fatigue and Design, Published on Demand by University Microfilms International, Ann Arbor, Michigan, U.S.A., London, England, 1975.
- [2] O. Buxbaum, Methods Stress-Measurement Analysis for Fatigue Life Evaluation, AGARD-LS-No. 62, 1973.5.
- [3] Wu Fumin and Zhang Baofa, "Statistical Treatment of Random Load-Time Mechanisms," Xi Bei Gong Ye Da Xue "Ke Ji Zi Liao," [Northwestern Polytechnical University "Science and Technical Materials"], No. 655, 1978-7.
- [4] J.B. de Jonge, The Monitoring of Fatigue Loading, ICAS Paper No. 70-31, 1970.
- [5] G.M. Van Kijk, Statistical Load Data Processing, NASA SP309, pp. 565-588, 1971.4.
- [6] Cycle Counting and Fatigue Damage, Journal of Society of Engineers, 1976.9 (Vol. 15-13).

- [7] Michael A. Landy, Mitchell P. Kaplan and Joseph A. Reiman, Derivation and Analysis of Loading Spectra of USAF Aircraft, AD A023528 (Report ASD-TR-76-1), 1976.1.
- [8] "New Determination of Fighter Aircraft Fatigue Performance," Fei Ji Pi Lao Shi Yan Yi Wen Ji (Yi) [Collection of Translated Documents on Aircraft Fatigue Tests (1)], Base 011 Technology Intelligence Center, pp. 1-20.
- [9] Cycle Counting and Fatigue Damage, Tu Ying Can Kao Zi Liao [Going to England For Reference Materials], for text translation see Foreign Aeronautics Technology, 1978, aircraft 21.
- [10] Gao Zhentong, "Working Out of Fatigue Load Spectrum," Hang Kong Xue Bao [Journal of Aeronautics], 1980, Vol. 2.
- [11] Jiang Zuguo and Huang Wuqi, Ji Shu Fa Ji Jian Hua Yuan Ze Zai He Pu Ji Suan Bao Gao [Report on Load Spectrum Computations of Counting Method and Principle of Simplification], 1980.2.
- [12] Charles Lipsop and Robert C. Juvinall, Handbook of Stress and Strength, The Macmillan Company, 1963.
- [13] T. Hans Dippeling, A.M.L. Mech, E.A.F.R. Ae.S., Loading Statistical as a Basis of Structural and Mechanical Design, Engineer's Digest, 1962, 3.4.5.
- [14] Guan Yu Kai Zhan Ji Shu Fa Da Bi Shi Yan De Bao Gao [Report on Development of a Counting Method For Contrasting Tests], Research Institute 630, 1978.12.
- [15] Gu Mingda, Zhang Shijie and Wu Dejun, Ji Shu Fa Ji Ta Jian Hua Yuan Ze Dui Bi Shi Yan Bao Gao [Report on Counting Methods and Their Principles of Simplification for Contrasting Tests], Research Institute 621, 1980.2.
- [16] Jiang Zu Guo, Geng Ren, An Bu Tong Ji Shu Fa Ji Jian Hua Yuan Ze De Shou Ming Gu Suan [Life Estimates According to Different Counting Methods and Principles of Simplification], Research Institute 630, 1980.2.
- [17] John Scott Atkinson, Jr., A Study of Spectrum Loading and Range-Pair Counting Method Effects on Cumulative Damage, AD A039651, 1977.3.
- [18] Ji Shu Fa Ji Jian Hua Yuan Ze Yan Jiu Bao Gao [Report on Research of Counting Methods and Principles of Simplification], Research Team on Aircraft Load Spectrum, Penned by Jiang Zuguo, Research Institute 630, 1980.3.

A GENERAL FORMULA OF STRESS INTENSITY FACTORS FOR CT SPECIMENS

Wang Keren
(Institute of Mechanics, Academia Sinica)

Abstract

A general formula ((5), (7), (8) for the stress intensity factors of the compact tension specimens is derived from a simple mechanical analysis and can be applied to a wide range of H/W and a/W . In comparison to the boundary collocation method, errors of its results are less than 1% (the errors of most of the data are less than 0.5%).

The fundamental functions K_b and K_s are obtained in this paper by fitting the boundary collocation method used by Srawley [1,2] and others. During fitting, it has been found that there are five K values incompatible in references [1 and 2] but they confirmed the recalculated results in reference [3].

Use of the formulas in this paper can also conveniently calculate the compliance of the specimens. The results are also found to be satisfactory.

I. INTRODUCTION

Compact tension specimens are extensively applied crack mechanic specimens. The demarcating work of their stress intensity factors are extremely important.

In references [1 and 2], Srawley and others use the boundary collocation method to compute the stress intensity factors of different H/W and a/W dimension compact tension specimens. To date, it has been the primary basis of crack mechanic tests. Later, Fan Tianyou[3] used the same method, slightly enlarged the range of a/W and made computations. The majority of the

results were identical with the results of references [1 and 2], but also had numerical differences reaching 3%. To date, there still is no general analytical formula to compute the stress intensity factors when there are arbitrary N/W and a/W values. When a/W and H/W values are comparatively small, because the variation of the K value is very sudden, interpolation is sometimes very difficult, and the analytical formula is very useful.

This paper uses simple mechanical analysis, and proposes a general formula for compact tension specimens. In comparing the results of the formula with values that tally in references [1, 2, and 3] (if the values of the errors are less than 1%, it occupies more than 90%), the errors are all within 1%. As to the results that do not tally in references [1, 2, and 3], the analysis that this paper provides can be regarded as a basis for further differentiation.

II. ANALYSIS

When considering the specimen shown in Fig. 1(a), its half-height is H , its width is W^* and its crack length is a^* . Under the effects of the end section shearing force P and bending moment M , the stress intensity factors separately are \bar{K}_b^* and \bar{K}_s^* . Again considering the specimen shown in Fig. 1(b), its half-height still is H , its ligament width $W-a$ is equal to ligament width W^*-a^* of the (a) specimen and its crack length a then is arbitrary. Under the effects of end section shearing force P and bending moment M , its corresponding stress intensity factors are \bar{K}_s and \bar{K}_b . The specimen in Fig. 1(b) can be regarded as a section of the specimen in Fig. 1(a), as shown by the dotted line in Fig. 1(a). Bending moment M acting on the (a) specimen corresponds to the same bending moment M acting on the (b) specimen. Therefore we have $\bar{K}_b = \bar{K}_b^*$, and it has no relation to either a or a^* . When shearing force P acts on the (a) specimen, this corresponds to shearing force P as well as bending moment

$P(a^*-a)$ acting on the (b) specimen. Thus we have:

$$\bar{K}_s + \frac{P(a^* - a)}{M} \bar{K}_s = \bar{K}_s^* \quad (1)$$

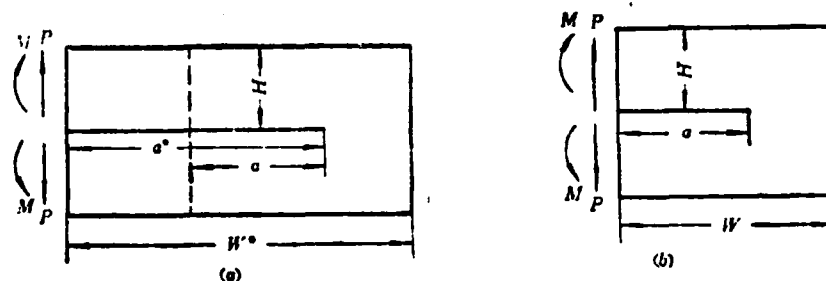


Fig. 1. Specimen

Making:

$$\bar{K}_s^* = \bar{K}_s - \frac{Pa^*}{M} \bar{K}_s \quad (2)$$

and noting that $\bar{K}_b = \bar{K}_b^*$, we obtain

$$\bar{K}_s = \bar{K}_s^* + \frac{Pa}{M} \bar{K}_s \quad (3)$$

Because \bar{K}_s and \bar{K}_b^* have no relation with the selection of a^* , therefore \bar{K}_s^{**} also should have no relation with the selection of a^* . Making

$$\left. \begin{aligned} K_s &= \frac{\bar{K}_s^* B \sqrt{W - a}}{P} \\ K_b &= \frac{\bar{K}_b^* B \sqrt{(W - a)^2}}{M} \\ K &= \frac{\bar{K}_s B \sqrt{W}}{P} \end{aligned} \right\} \quad (4)$$

(B is the specimen thickness), and substituting formula (3) thus we obtain:

$$K = \sqrt{\frac{1}{1 - \frac{a}{W}}} \left(K_s + \frac{a/W}{1 - \frac{a}{W}} K_b \right) \quad (5)$$

K_s and K_b are both the function of:

$$h = \frac{H}{W - a} = \frac{H/W}{1 - a/W} \quad (6)$$

Formula (5) then is the fundamental formula that we use. K_b and K_s are the fundamental functions.

III. DETERMINATION OF K_s and K_b

As to the different h values, based on the data of references [1 and 2], we use the interpolation method to obtain the stress intensity factors under each a/W value and corresponding H/W value. Substituting formula (5), under the significance of the minimum second power, we determine the values of K_b and K_s . Later we drew the curves of $K_b \sim h$ and $K_s \sim h$, making some slight revisions on some irregular values. We discovered that K_b and K_s can very accurately be described by the following formulas:

$$\left. \begin{aligned} K_s &= \frac{2.51}{1 - e^{-3.01h^{1.100}}} & h \geq 0.8 \\ K_s &= 1.848 + \frac{0.728}{h} & h < 0.8 \end{aligned} \right\} \quad (7)$$

$$\left. \begin{aligned} K_b &= \frac{3.98}{1 - e^{-2.047h^{1.25}}} & h \geq 1 \\ K_b &= \frac{11.13h^2 - 13.13h + 11.17}{h(h+1)} & h < 1 \end{aligned} \right\} \quad (8)$$

We list the corresponding K_s and K_b values of the related h value of the data in references [1 and 2] in Table 1. When the h value is comparatively large, due to the greater amount of interpolation data, therefore our determined K_b and K_s values are comparatively accurate; when the h value is very small, partial data can only be obtained based on extrapolation, and precision is comparatively poor. Generally speaking, when $h \geq 0.4$, our determined K_b and K_s values are very precise.

Table 1. K_b and K_s values

h	K_b	K_s	h	K_b	K_s
≥ 2	3.98	2.51	0.75	5.78	2.82
1.667	4.00	2.52	0.714	6.10	2.87
1.6	4.01	2.53	0.667	6.63	2.94
1.5	4.03	2.53	0.625	7.20	3.01
1.429	4.06	2.54	0.571	8.13	3.12
1.333	4.11	2.55	0.5	9.85	3.30
1.25	4.17	2.56	0.476	10.59	3.38
1.2	4.22	2.58	0.417	12.93	3.60
1.143	4.29	2.59	0.4	13.75	3.67
1.111	4.34	2.60	0.357	16.30	3.89
1.0	4.57	2.64	0.333	18.07	4.03
0.952	4.71	2.66	0.313	19.88	4.18
0.857	5.08	2.73	0.286	22.67	4.40
0.833	5.21	2.74	0.250	27.47	4.76
0.8	5.41	2.76			

When the h value is very large, K_s and K_b separately tend to become constant 2.51 and 3.98. Substituting formula (5), we thus obtain $K=$

$$\sqrt{\frac{1}{1 - \frac{a}{W}}} \left(3.98 \frac{\frac{a}{W}}{1 - \frac{a}{W}} + 2.51 \right) \quad (9)$$

This then is the asymptotic solution that Koiter obtained [6].

IV. ANALYSIS OF RESULTS COMPUTED IN REFERENCES [1 and 2]

We used formulas (5), (7) and (8) to recalculate all of the results in references [1 and 2], and these are listed in Table 2. The values in references [1 and 2] are listed in Table 3. Comparing the two, the majority of the differences in the data are within 0.5%. In Table 4, we list the five data that have differences exceeding 1%. In the table, we simultaneously list the computed results in reference [3]. Reference [3] uses the same kind of computation method (boundary collocation method) to recalculate all of the data in references [1 and 2]. The computed results only have five places where differences exceed 1%, and they are in complete accord with our computed results. From the point of view of numerical computations, reference [3] shows that the computed results of references [1 and 2] are not correct in several places. Our computed results further confirm this conclusion. The tests take the values of $a/W=0.6$ and $H/W=0.2$ as examples to show this. Their corresponding h value is:

$$h = \frac{H/W}{1 - a/W} = 0.5$$

Table 5 lists the H/W values corresponding to $h=0.5$ when there are different a/W values as well as the K values that are obtained from the interpolation of the data of references [1 and 2]. In the table, we simultaneously list the computed results in formula (5) when $K_p=9.85$ and $K_s=3.30$. From Table 5 it is not hard to see that this data of 28.01 in references [1 and 2] really does not coordinate with other data (the errors of other data are all within 0.5%).

Table 2. Computed results of formula (5)
(K value of compact tension specimen)

$H/W \backslash a/W$	0.2	0.3	0.4	0.5	0.6	0.7	0.8	0.9
0.2	13.00	16.87	20.76	24.63	28.59	33.60	46.78	121.29
0.25	10.23	12.99	15.77	18.60	21.84	27.20	43.02	121.21
0.333	7.63	9.46	11.36	13.53	16.69	23.24	41.12	121.21
0.4	6.45	7.90	9.50	11.55	15.01	22.15	41.21	121.21
0.5	5.38	6.55	8.03	10.20	13.94	21.65	41.21	121.21
0.6	4.77	5.86	7.34	9.61	13.57	21.56	41.21	121.21
0.667	4.52	5.60	7.09	9.41	13.48	21.54	41.21	121.21
0.8	4.23	5.29	6.83	9.24	13.42	21.54	41.21	121.21
1.0	4.03	5.11	6.70	9.19	13.41	21.54	41.21	121.21

Table 3. Computed results of Srawley and others [1,2]
(K value of compact tension specimen)

$H/W \backslash a/W$	0.2	0.3	0.4	0.5	0.6	0.7	0.8
0.2	12.90	16.85	20.72	24.49	28.01	33.42	
0.25	10.20	13.00	15.76	18.57	22.35	26.81	
0.333	7.65	9.35	11.34	13.53	16.64	23.16	
0.4	6.44	7.87	9.46	11.54	15.00	22.20	41.13
0.5	5.36	6.52	8.00	10.18	13.98	21.56	41.01
0.6	4.75	5.84	7.33	9.63	13.62	21.53	41.04
0.667		5.59	7.10	9.45	13.52	21.54	
0.8	4.21	5.31	6.86	9.29	13.44	21.53	40.85
1.0	3.99	5.14	6.74	9.22	13.42	21.53	40.01

Table 4. Five data with errors exceeding 1%

		(1)	(2)	(3)	(4)
a/W	H/W	文献[1、2]内的K值	(5)式的计算结果	误差(%)	文献[3]内的K值
0.3	1/3	9.35	9.46	1.2	9.45
0.6	0.2	28.01	28.59	2.1	28.57
0.6	0.25	22.35	21.84	2.3	21.75
0.7	0.25	26.81	27.20	1.5	27.17
0.8	1.0	40.01	41.21	3.0	41.24

Key: (1) K value in references [1 and 2]; (2) Computed results of formula (5); (3) Errors (%); (4) K value in reference [3].

Table 5. K value when h=0.5

a/W	H/W	文献(1、2)内的K值 (1)	(5)式的计算结果 (2)
0.2	0.4	6.44	6.45
0.3	0.35	9.00(插值)(3)	8.99
0.4	0.3	12.80(插值)(4)	12.74
0.5	0.25	18.57	18.60
0.6	0.2	28.01	28.59

Key: (1) K values in referenced [1 and 2]; (2) Computed results of formula (5); (3) Interpolation; (4) Interpolation.

V. Flexibility value

Gross, Roberts and Srawley [7] use the boundary collocation method to compute the flexibility of the different a/W values when H/W=0.8, 0.6, 0.55 and 0.48. Later, Roberts [8] also used the same method to conduct computations when H/W=0.6, the largest differences of the two reached 2%. Generally speaking, when using the boundary collocation method to find the stress intensity factors, because it only uses the coefficient of the first item of Williams' expansion, in general convergence is comparatively good; as to displacement, then we must use all coefficients, and thus convergence is comparatively poor. On the basis of the Irwin-Kies formula, the flexibility value can be obtained from the stress intensity factor integral:

$$BE'C - BE'C_0 = \int_0^{a/W} \left(\frac{\bar{K} B \sqrt{W}}{P} \right)^2 d\left(\frac{a}{W}\right) \quad (10)$$

Here C is specimen flexibility, C_0 is corresponding flexibility of the specimen when there are no cracks, $E'=E$ (plane stress) and $E'=E/(1-\nu^2)$ (plane strain).

From the results listed in the table we see that their differences are approximately within 2%. What is computed in references [7 and 8] is the displacement on the crack surface; when a/W is very small, it has corresponding differences with the added load displacement. Thus we see that the results obtained by our computations are applicable. By applying formulas (5), (7), (8) and (10) it is very easy to obtain the flexibility value of the arbitrary H/W and a/W values.

Table 6. Flexibility value.						
$\frac{H}{W}$	$\frac{a}{W}$	文献[7]内的 (1) BE'C	文献[8]内的 (2) BE'C	(10)式计算的 (3) BE'C-BE'C ₀	采用的 (4) BE'C ₀	(10)式计算的 (5) BE'C
0.8	0.3	11.81		9.34		12.04
	0.4	19.28		16.59		19.29
	0.5	32.14		29.28	2.70	31.98
	0.6	57.34		54.33		57.03
	0.7	116.0		113.10		115.80
0.6	0.3	14.27	14.48	11.76		14.36
	0.4	22.97	23.22	20.40		23.00
	0.5	37.02	37.2	34.54	2.60	37.14
	0.6	63.32	63.2	60.72		63.32
	0.7	122.1	119.8	119.94		122.54
0.55	0.3	15.13		13.00		15.50
	0.4	25.06		22.40		25.90
	0.5	39.88		37.44	2.50	39.94
	0.6	66.93		64.48		66.98
	0.7	126.70		124.20		126.70
0.48	0.3	18.08		15.62		18.07
	0.4	29.47		26.77		29.22
	0.5	46.23		43.88	2.45	46.33
	0.6	75.23		73.12		75.57
	0.7	137.0		134.45		136.90

Key: (1) BE'C in reference [7]; (2) BE'C in reference [8];
 (3) BE'C-BE'C₀ computed from formula (10); (4) BE'C₀ which
 was used; (5) BE'C computed from formula (10).

VI. Discussion

On the basis of our deductions, formula (5) cannot be suitable when a/W is very small. We give the values of $a/W=0.1$ in Table 7, and make comparisons with the results in reference [3]. Among them, the differences are relatively large when $H/W=0.20$ and $H/W>0.6$. When $H/W=0.20$, because the h value is small, the K_D and K_S values obtained are not accurate enough. When $H/W>0.6$, the a/W value is possibly too small that is if it is

compared to the H/W value. Formula (5) already is not accurate enough.

Table 7. K value when $\frac{a}{W}=0.1$

	(1)	(2)
$\frac{H}{W}$	文献(3)内的K值	(5)式的计算值
0.20	9.08	9.20
0.25	7.42	7.48
0.333	5.83	5.83
0.40	5.03	5.05
0.50	4.26	4.32
0.60	3.72	3.88
0.667	3.49	3.67
0.80	3.19	3.43
1.0	2.93	3.25

Key: (1) K values in reference [3];
(2) Values computed from formula (5).

References

- [1] Srawley, J.E., Gross, B., Mat. Res. Stand., 7(1967), 4,155.
- [2] Srawley, J.E., Gross, B., Eng.Fracture Mech.,4(1972),587.
- [3] Fan Tianyou, Ke Xue Tong Bao [Science Bulletin], 21(1976),494.
- [4] Irwin, G.R., Kies, J.A., Weld. J. (Res. Suppl.)3(1954),1935.
- [5] Gross, B., Srawley, J.E., NASA TN D-3092(1965).
- [6] Benthien, J.P., Koiter, W.T., Mechanics of Fracture, Vol. 1 (ed. Sih, G.C.), 1973.
- [7] Gross, B., Roberts, E.Jr., Srawley, J.E., Int. J. Fracture Mechanics 4(1968), 3, 267.
- [8] Roberts, E. Jr., Mat. Res. Stand., 9(1969), 27.

A FINITE ELEMENT METHOD FOR LOCAL STABILITY OF A STIFFENED PANEL IN AXIAL COMPRESSION

Liu Dongchang
Aircraft Strength Institute

Abstract

This paper is a research report on the problem of using a finite element method for local stability of a stiffened panel in axial compression. Proceeding from the symmetry analysis for the mode of buckling deformation, a local unit computation model is proposed. The limitations of the typical unit computation model are pointed out for the structures with unsymmetric modes of buckling deformation. Therefore, we determined the universal adaptability of the local unit in stability calculations. For the rivet-joint structure, we analyzed the assumption of simplification for the attachment of covering and stiffness, improved the computation model for the rivet-joint structure and ensured the rationality of the computation results. Furthermore, we discussed two principles for simplifying the computation model. On this basis, we carried out further simplification of the computation model and thereby saved on computer internal storage and raised throughput speed. Lastly, this paper gives computation curves and test results, and analyzes the moment distribution method.

I. PREFACE

In recent years, the problem of using a finite element method for the local stability of a structure has aroused peoples' attention. In particular is the analysis made by J.S. Przmieniecki[1] in 1973 on local stability of a stiffened panel. He used the large deflection strain-displacement relationship to establish a rigidity matrix of panel elements. We consider

his work in the theoretical area to be extremely important. However, his computed structure and its mode of buckling deformation is symmetrical, and the computation model that is used is a typical unit computation model (as shown in Figs. 1(a) and (b)). In actual structures, such as model "Z", angular model, etc. stiffened panels, the mode of buckling deformation of the covering is asymmetrical (as shown in Figs. 1(c) and (d)). In this way, the computation model of the typical unit is limited. Additionally, it is worth noting that reference [2] carries out the same kind of research and computations on rivet-joint and glue-joint stiffened panels. However, because they did not differentiate between their attachment forms, therefore some results are not very ideal.

This paper considers the differences of asymmetrical conditions and attachment forms in actual structures, and we carry out research in the following areas:

(1) Firstly, setting out from the viewpoint of rigidity, we analyze the symmetry of the mode of buckling deformation of the structure and propose the computation model of the local unit. As to the structures with asymmetric mode of buckling deformation, we propose the use of the computation model of the typical unit. What is obtained is the computed results of false structures, and this is not reasonable.

(2) We distinguish the differences of the attachment forms of stiffened panels. In rivet-joint stiffened panels, we analyze the assumption of simplification for the attachment of the covering and the stiffeners. We make improvements on the original computation model.

(3) We clarify the two principles of the simplified computation model.

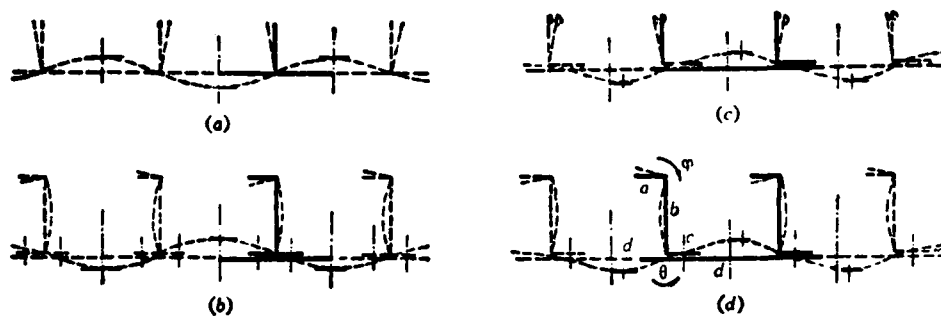


Fig. 1. Two different deformation modes.

Key: (a) The whole siffened panel and typical unit of the symmetry of the deformation mode; (b) The rivet-joint stiffened panel and typical unit of the symmetry of the deformation mode; (c) The glue-joint stiffened panel and local unit of the unsymmetry of the deformation mode; (d) The rivet-joint stiffened panel and the local unit of the unsymmetry of the deformation mode.

In the report, we also give the computed curve and test results of several kinds of stiffened panels, and make comparisons with the computed curves of references [4, 5, and 6] that use the moment of force distribution method. Additionally, in the conclusion we analyze the moment of force distribution method and similar assumptions that are used when selecting the computation model, and propose that the finite element method can obtain comparatively good computation results.

II. SOLVING THE FINITE ELEMENT METHOD OF THE LOCAL STABILITY PROBLEM

If the stiffened panels under the effect of axial compression load have local buckling, its deformation after buckling is as shown in Fig. 2. When computing its local buckling stress, we did not need to conduct computations on the whole structure, it was only necessary to take the local unit or typical unit as our computed object (as shown in Figs. 2(b) and (c)). It longitudinally takes the length between two adjacent wave nodal lines,

and regards the linking of other sections as its edge element or boundary condition for processing.

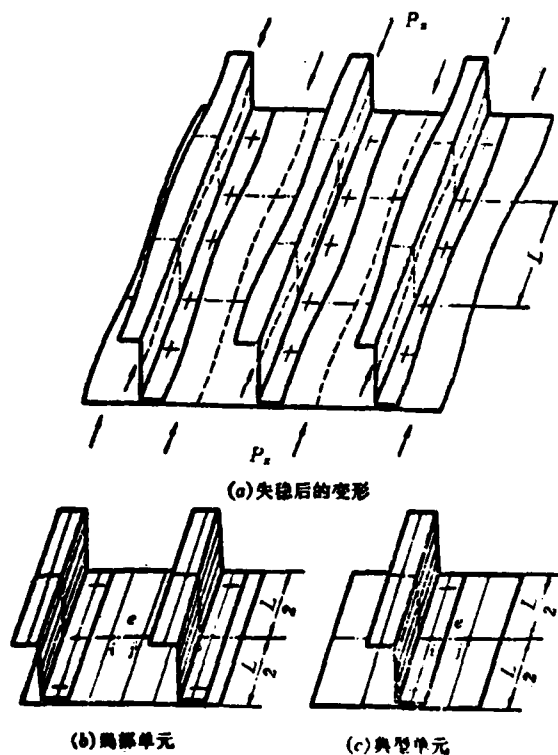


Fig. 2. The computed object of deformation and selection after buckling of the "Z" model stiffened panel.

Key: (a) Deformation after buckling; (b) Local unit; (c) Typical unit.

1. Panel Strip Element

We disperse the computed objects into finite panel strip elements (see Figs. 2(b) and (c)). Among them, we let one element e be linked with the adjacent element from nodal

points i and j . Additionally, based on the deformation mode we give the mechanical conditions and boundary conditions, and in this way the local unit and typical unit shown in Figs. 2(b) and (c) then become corresponding computation models.

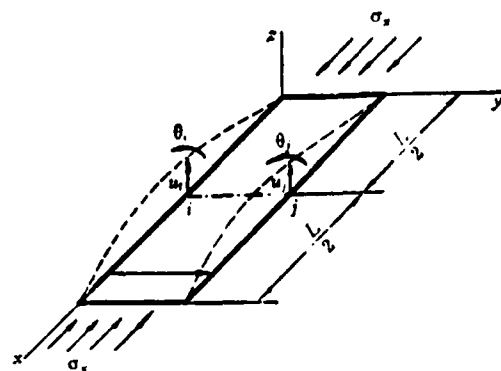


Fig. 3. Panel strip element

As to the panel strip elements (see Fig. 3), we assume that displacement function U_z follows the variation of direction x and assumes a sinusoidal form. Its length is buckling semi-wave-length L . In this way, the normal displacement function can be expressed as:

$$U_z = Y(\eta) \sin \frac{\pi x}{L} \quad (1)$$

In the formula, $\eta = y/b$ and b is the width of the panel strip element.

Assuming the two nodal points of element e are i and j , nodal point displacement is expressed by u_i , θ_i , u_j , and θ_j . Among these, u_i and u_j are normal displacement, θ_i and θ_j are the angles of rotation winding around the x axis.

2. Element Rigidity Matrix

On the basis of the formula of the large deflection strain-displacement relationship, we consider the assumption that the inside rigidity is greater than the outside rigidity, omit the high order small mass and write it into matrix form:

$$\epsilon = \begin{pmatrix} \epsilon_x \\ \epsilon_y \\ \epsilon_{xy} \end{pmatrix} = \begin{pmatrix} \frac{\partial U_x}{\partial x} \\ \frac{\partial U_y}{\partial y} \\ \frac{\partial U_x}{\partial y} + \frac{\partial U_y}{\partial x} \end{pmatrix} + \begin{pmatrix} \frac{1}{2} \left(\frac{\partial U_x}{\partial x} \right)^2 \\ \frac{1}{2} \left(\frac{\partial U_x}{\partial y} \right)^2 \\ \frac{\partial U_x}{\partial x} \frac{\partial U_x}{\partial y} \end{pmatrix} \quad (2)$$

Assuming $Y(\eta)$ is the cubic polynomial expression of η , its four coefficients can use nodal point displacements u_i , θ_i , u_j and θ_j for determination. Thus formula (1) can be expressed as:

$$U_x = A(\eta) \sin \frac{\pi x}{L} U^e \quad (3)$$

In the formula

$$\begin{aligned} U^e &= (u_i, \theta_i, u_j, \theta_j)^T \\ A(\eta) &= (a_1(\eta), a_2(\eta), a_3(\eta), a_4(\eta)) \\ \left. \begin{aligned} a_1(\eta) &= 1 - 3\eta^2 + 2\eta^3 \\ a_2(\eta) &= (\eta - 2\eta^2 + \eta^3) b \\ a_3(\eta) &= 3\eta^2 - 2\eta^3 \\ a_4(\eta) &= (-\eta^2 + \eta^3) b \end{aligned} \right\} \quad (4) \end{aligned}$$

On the basis of thin panel assumptions, utilizing the strain energy formula, we derive the elasticity-rigidity matrix and the geometric rigidity matrix of element e (for the process of derivation please refer to reference [1]; it is omitted from this paper).

$$K_e^* = K_{e1}^*(1/L^3) + K_{e2}^*(1/L) + K_{e3}^*(L) \quad (5)$$

In the formula

$$K_{e1}^*(1/L^3) = \frac{\pi^4 E t^3 b}{10080 (1 - \nu^2) L^3} \begin{pmatrix} 156 & & & \\ 22b & 4b^2 & \text{对(a)} & \\ 54 & 13b & 156 & \\ -13b & -3b^2 & -22b & 4b^2 \end{pmatrix}$$

$$K_{e2}^*(1/L) = \frac{\pi^2 E t^3}{360 (1 - \nu^2) b L} \begin{pmatrix} 36 & & & \\ (3 + 15\nu)b & 4b^2 & \text{对(b)} & \\ -36 & -3b & 36 & \\ 3b & -b^2 & -(3 + 15\nu)b & 4b^2 \end{pmatrix}$$

$$K_{e3}^*(L) = \frac{E t^3 L}{24 (1 - \nu^2) b^3} \begin{pmatrix} 12 & & & \\ 6b & 4b^2 & \text{对(c)} & \\ -12 & -6b & 12 & \\ 6b & 2b^2 & -6b & 4b^2 \end{pmatrix}$$

$$K_{ex}^* = K_{ex}^*(1/L) = \frac{\hat{\sigma}_x \pi^2 b t}{840 L} \begin{pmatrix} 156 & & & \\ 22b & 4b^2 & \text{对(d)} & \\ 54 & 13b & 156 & \\ -13b & -3b^2 & -22b & 4b^2 \end{pmatrix}$$

Key: (a) Symmetry; (b) Symmetry; (c) Symmetry;
(d) Symmetry.

In the formulas, b and t separately are the panel width and panel thickness of element e ; E and ν are the material elasticity modulus and Poisson's ratio; $\hat{\sigma}_x$ and L are axial compression buckling stress and buckling semi-wavelength.

3. Total Rigidity Matrix and Characteristic Equation

The element rigidity matrix is superposed according to the element's nodal point number and any element in its matrix K is:

$$k_{ij} = \sum_e k_{ij} \quad (6)$$

The lower symbols i and j separately express the i line and the j row of matrix K , e is the number of the panel strip elements.

After the total rigidity matrix forms, we must cross out the related lines and rows with displacement as zero. Thus we obtain a new balance system of equations, written as:

$$KU = P \quad (7)$$

The external load is expressed as the multiple of certain reference load P^* :

$$P = \lambda P^*$$

Because $\hat{\delta}_x$ is in proportion to the exterior load, therefore:

$$K_{Gx} = \lambda K_{Gx}^*$$

Then, formula (7) can be written as:

$$(K_s + \lambda K_{Gx}^*)U = P \quad (8)$$

When the panel deflection infinitely increases, then

$$|K_s + \lambda K_{Gx}^*| = 0$$

expresses the structural buckling. It is further rewritten as:

$$\left| -K_s^{-1} \cdot K_{Gx}^* - \frac{1}{\lambda} I \right| = 0 \quad (9)$$

In the formula, K_E and K_{Gx} are the total elasticity-rigidity and geometric rigidity matrices, I is the equivalent unit matrix. In this way, the problem of solving local buckling stress is then turned into the problem of finding the largest

characteristic root $(1/\lambda)_{\max}$ of the real matrix $(-K_E^{-1} \cdot K_{Gx}^*)$ in mathematics.

As to the condition of single axial compression, taking reference stress $\hat{\sigma}_x^* = -1\text{kg/mm}^2$, matrix $(-K_E^{-1} \cdot K_{Gx}^*)$ then becomes a positive definite matrix. In this way, the reciprocal λ_{\min} of the largest characteristic root $(1/\lambda)_{\max}$ that is obtained is equal in numerical value to load buckling stress $\hat{\sigma}_x$.

III. DISCUSSION OF COMPUTATION MODEL AND ANALYSIS OF COMPUTED RESULTS

1. The Concept of Two Computation Models and Analysis of Symmetry

For convenience of narration, this paper introduces the concepts of the two technical terms of typical units and local units and the symmetric mode of buckling deformation.

We call the computation models that are used in references [1 and 2] typical units (the section in Fig. 4 that is encircled by a dot-dash line). We can see that the computation model of the typical unit (Fig. 4(e)) is a "typical unit" that is cut out from in the entire structure. The constraint effect that is provided on the typical unit with other panel units that are linked to the typical unit is reflected by the condition of zero angular displacement. Naturally, it is assumed that the boundary constraint conditions of zero angular displacement of the covering's center point utilizes the characteristics of the symmetric mode of deformation.

In the whole structure, the local unit is the section encircled by the double dot-dash line in Fig. 4. Additionally, in the "Z" model stiffened panel shown in Fig. 1(d), the "Z" model stiffened panel strip is also a local unit. We can consider that

the local unit takes the "local" (panel unit) that is computed and "boundary constraint conditions" together as the object of our research. Specifically, the computation model of the local unit (as shown in Fig. 4(d)) regards the stiffened strip as the "boundary constraint condition" of the covering ("local"), the ventral panel b of the "Z" model stiffened strip ("local") takes the top and bottom pointed edges as its "boundary constraint conditions". In local unit computations, they are a unified body that cannot be separated. From this we can see that the computation model of the unit is regarding each computed "local" along with its "boundary condition" together as our computed object. In comparing this kind of computed object and the typical unit, the "boundary constraint conditions" that it in itself bears is its important distinguishing feature.

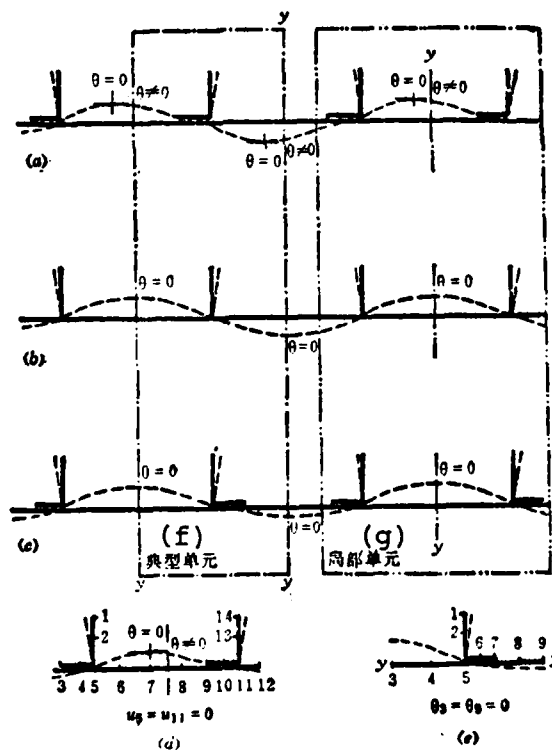


Fig. 4. (see next page)

Fig. 4. Comparison of the deformation mode and computation model of two structures.

Key: (a) Deformation mode of glue-joint stiffened panel; (b) Deformation mode of entire stiffened panel; (c) Deformation mode of false structure; (d) Computation model of local unit; (e) Computation model of typical unit; (f) Typical unit; (g) Local unit.

We call elements other than the local unit the edge elements of the local unit. The influence of edge elements on the buckling stress of local units is very small and can be overlooked. The physical significance of this conclusion will be discussed in the third section of this article.

As to one type of structure, if the geometric form of the cross section is symmetrical, we call it a symmetrical structure (such as the entire stiffened panel shown in Fig. 1(a)). For every symmetrical structure, the constraint effect that is provided by each symmetrical panel unit on "local" buckling deformation (including the constraint effect of finite curves deformation and rotational deformation) is symmetrical. The deformation mode after its buckling also will be symmetrical. Additionally, as to the "Z" model stiffened strip, its top and bottom pointed edges are positioned in the two sides of its ventral panel (the geometric form is unsymmetrical), but the rigidity constraint effect that is provided by it on the ventral panel is equivalent to slotted type "(]" — the geometric form is symmetrical) stiffened strip. As to the stiffened panel shown in Fig. 1(b), the rigidity constraint effect that is provided by the stiffened strip on the covering is symmetrical. Naturally, the deformation mode after the buckling of the later two structures is also necessarily symmetrical. From this it is given that if the rigid constraint effect that is provided by each panel unit of the structure on certain "local" (for example,

the covering, ventral panels, etc.) is symmetrical, we then call the structure that possesses this type of mechanical property a symmetrical structure. However, in engineering practice another kind of structure that is extensively applied (for example, the stiffened panels shown in Figs. 1(c) and (d)) does not possess the above-mentioned characteristics, and the deformation mode after its buckling is not symmetrical. We call this kind of structure an asymmetrical structure.

2. Comparison of the Local Unit and Typical Unit

The asymmetrical structure takes the glue-joint stiffened panel as an example, and the deformation mode after its buckling is asymmetrical (see Fig. 4(a)). If we regard the typical unit as our computed object (as shown in Fig. 4(e)), its computed result corresponds to computing a false structure (as shown in Fig. 4(c)). Comparing the three deformation modes of (a), (b), and (c) of Fig. 4, the angle of rotation of the entire stiffened panel at "y-y" is zero. This is in agreement with the assumption of the typical unit. However, the deformation mode of the glue-joint stiffened panel is asymmetrical and its angle of rotation at "y-y" is then not equal to zero. If this structure in the same way uses the computation model of the typical unit, it is then very obviously equal to changing the asymmetrical structure into the symmetrical structure as shown in Fig. 4(c). Of course, the comparison of this kind of structure and the original structure changes the deformation mode of the structure (the deformation mode of a false structure).

The computation model of the local unit (as shown in Fig. 4(d)) links the computed "local" together with the "boundary constraint condition" as the computed object, avoiding the assumption that "the angle of rotation is zero" in the typical unit, making its buckling deformation mode a deformation mode that is a lifelike

and real structure. By comparing Figs. 4(a) and (d) we can see that the deformation mode of the local unit is identical with the deformation mode of the whole structure.

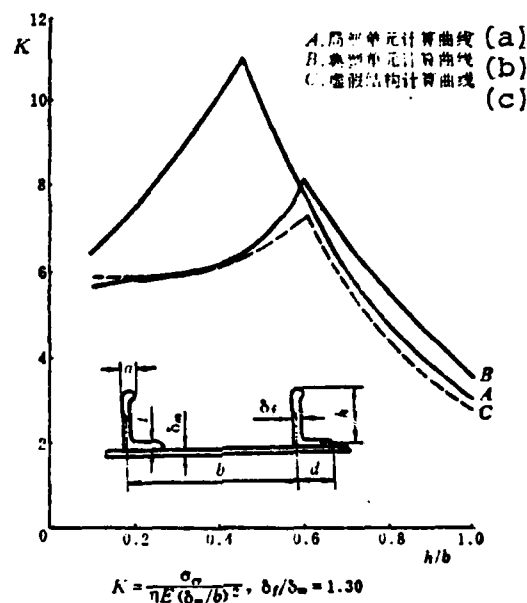


Fig. 5. Curve of local buckling stress coefficient of glue-joint stiffened panel.
Key: (a) Computed curve of local unit; (b) Computed curve of typical unit; (c) Computed curve of false structure.

Fig. 5 gives the curve of the buckling stress coefficient $K-h/b$ of the glue-joint stiffened panel.* We can see that the computed curve of the typical unit and the curve of the false

* Regarding the glue-joint stiffened panels, we still have not seen any literature that has given its computed curve. Some material explains problems of related areas and only suggests the use of the method of rivet-joint structures to conduct computations. (But even less discussed is what the computed results are. However, as to what the computed results are is even less often discussed). Additionally, in buckling stress coefficient $K = \frac{\sigma_{cr}}{\eta E (\delta_m/b)^2}$, σ_{cr} is the local buckling stress and η is the moulded correction coefficient (see reference [5]).

structure are comparatively close.

In Fig. 6, we give the curve of the buckling stress coefficient $k-h/b$ of the "Z" model rivet-joint stiffened panel. In it, computed curve B of the local unit and curve A given in reference [4] are comparatively close, and computed curve C of the typical unit and computed curve D of the false structure are comparatively close.

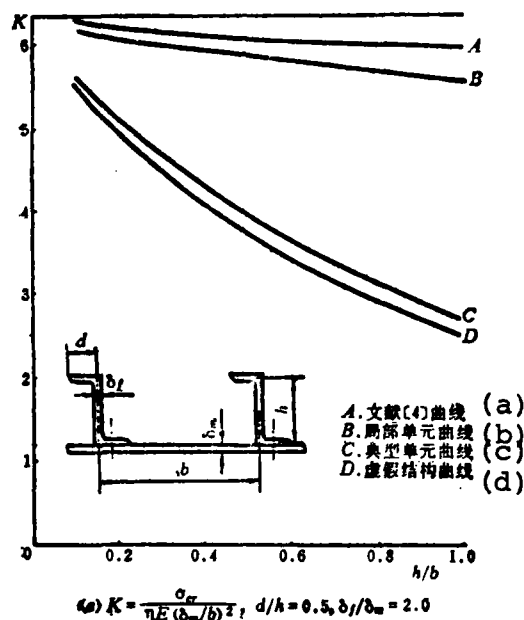


Fig. 6. Curve of local buckling stress coefficient of "Z" model rivet-joint stiffened panel.

Key: (a) Curve of reference [4]; (b) Curve of local unit; (c) Curve of typical unit; (d) Curve of false structure.

(See page 84 for rest of Fig. 6)

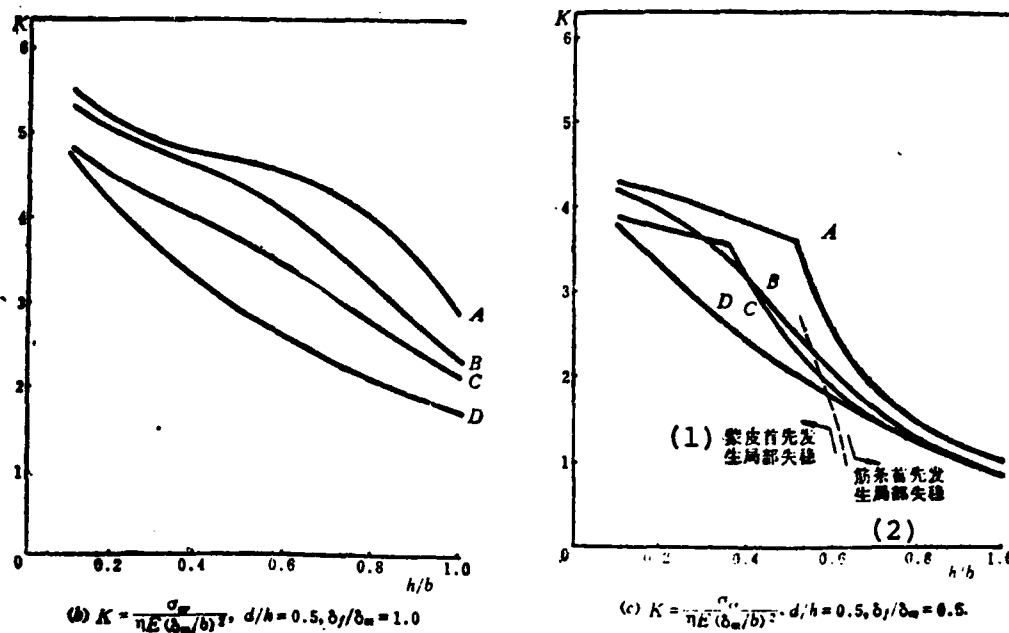


Fig. 6. Curve of Local buckling stress coefficient of "Z" model rivet-joint stiffened panel.

Key: (1) Local buckling first occurs on covering; (2) Local buckling first occurs on stiffened strip.

Additionally, the whole stiffened panel that has a symmetric mode of deformation in the same way uses the two computation models to carry out computations. From Fig. 7 we see that the computed curve of the local unit, curve A of reference [5] and computed curve C of the typical unit are all comparatively close. To sum up, we can conclude that in general structural computations, the local unit possesses universal practical significance.

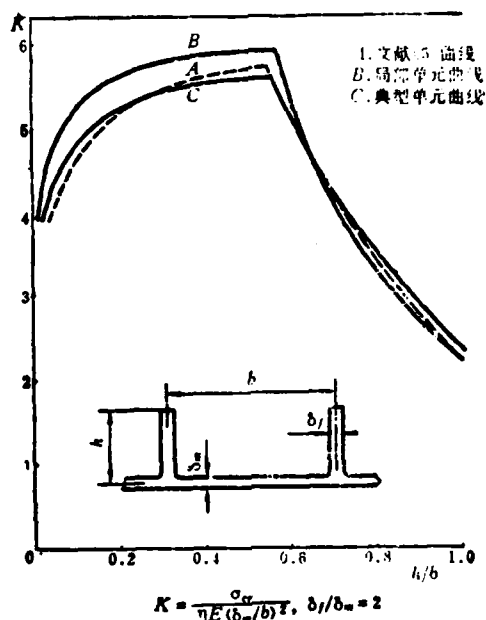


Fig. 7. Curve of local buckling stress coefficient of entire stiffened panel.
 Key: (A) Curve of reference [5]; (B) Curve of local unit; (C) Curve of typical unit.

3. Improvement and Simplification of the Computation Model

Previously, in local stability computations of rivet-joint stiffened panels, the section of contact of the stiffened strip with the covering has often been regarded as the entire body for consideration [2]. We consider that the deformation of rivet-joint structures on the rivet line are coordinated and consistent; deformation of other structures then is not coordinated and consistent. If it is treated according to the entire link, it will certainly strengthen the mutual constraints of each panel unit of the stiffened panel and thus raise the local buckling stress. In order to make the computation model close to the true linked form, we made improvements on the computation model of the rivet-joint stiffened panels. The computation model

shown in Fig. 8(a) is improved by Fig. 8(b). We can see that the thickness of the original computation model, the stiffened panel pointed edge and the element of the covering contact section is the sum of the thicknesses of the two panel elements; the improved computation model, the pointed edge and the covering only have common nodal points on the rivet line. The computed results of the improved computation model and the original computation model are listed in Table 1. In order to make comparisons, Table 1 also lists the computed results of the test results and the moment of force distribution method [6]. The computed results of the improved computation model are basically consistent with them. Yet, comparing the values of the computed results of the original computation model with the test values, errors all exceed 60%. Additionally, Fig. 9 gives the computed curve and test points of the "I" rivet-joint stiffened panel, and the test points are close to the computed curve of the improved computation model.

Table 1. Comparison of rivet-joint structure computed results and test values

(a) 结构名称	(b)	(c)	(d)	(e)	(f)
	计算模型	改进的计算模型	原来的计算模型	力矩分配法结果	实验结果
PS2-40		2.464	3.984	2.85	2.53
PS2-50		4.677	9.283	4.70	4.48
PS2-60		2.554	5.200	3.35	2.72
PS1-6		2.933	4.712	3.04	2.80
PS1-19		4.621	6.647	4.50	3.70
I-铆接(g)		4.439	6.117	4.20	3.59

Key: (a) Structure name; (b) Computation model; (c) Improved computation model; (d) Original computation model; (e) Moment distribution; (f) Test results; (g) Rivet-joint.

In the process of solving the eigenmatrix, it is necessary to shift all of the elements of the matrix and if we use the external storage unit of the computer then it is extremely difficult. Therefore starting from the computation model of the simplified structure, we use a matrix of fairly small scale to compute a comparatively complicated structure and its significance then appears to be especially important.

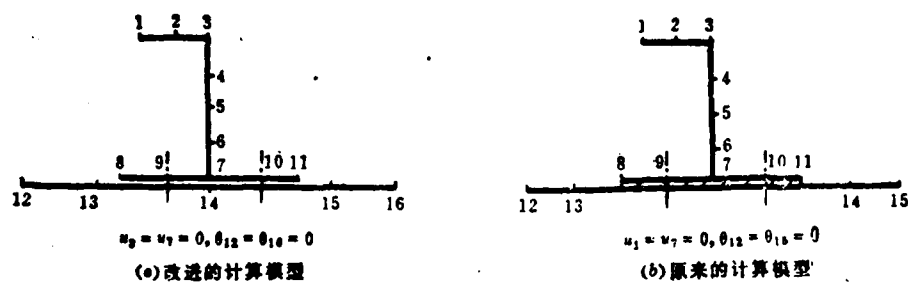


Fig. 8. Comparison of two different computation models of rivet-joint structures.
Key: (a) Improved computation model; (b) Original computation model.

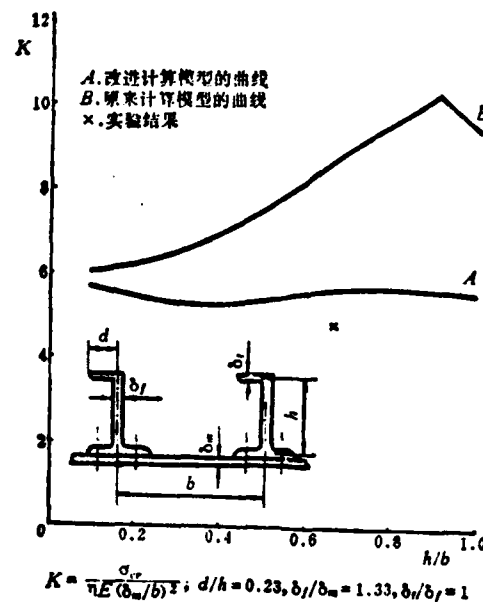


Fig. 9. Local buckling stress coefficient and test results of rivet-joint stiffened panel.
 Key: A. Curve of improved computation model; B. Curve of original computation curve; x. Test results.

The computation of the local unit and the typical unit referred to in the previous section are actually already simplified. Below are the primary newly clarified two principles for simplifying the computation model:

First, utilizing the characteristics of the symmetric mode of buckling deformation, we can use the condition of zero angular displacement to substitute the constraint effect provided by the partial panel unit for the computed object.

Second, the influence of the edge element on the local unit is very small and we can use a computation model of a local unit to substitute for the computation of an entire structure.

Symmetrical structures, using the typical unit to substitute

for the entire structure computation, carry out simplification based on the first principle. Further, we can also make simplifications such as those shown in Figs. 10(a) and (b). Naturally, the previous type of simplification regardless of the saving of computer internal storage will also raise the speed of solving the problem. Both are worth promoting. However, the later simplification causes the typical unit and the local unit to further simplify the results that were obtained. This cannot be overlooked. The computed model shown in Figs. 10(a) and (b) separately reduce 4 and 8 elements. Due to this type of simplification, computer internal storage is cut down 50% and the speed of solving the problem is raised approximately three-fold. Its computed results are also comparatively dependable and therefore the simplification of the computed model can attain the results of getting twice the result with half the effort.

By the whole structure being regarded as the computed object, there are no usable values in the real solution. Because the computer internal storage necessary for this kind of computation model is extremely large and the speed of solving the problem is extremely slow, these cannot be enabled by a small computer. But from the computed results we see that the necessity of doing this is not great and if we still regard the entire structure as the computed object then it is somewhat "seeking far and wide for what is close at hand." Therefore we propose the second principle to simplify the computation model. We now give the following explanation regarding the physical significance of the local unit: the computation model of the local unit of the stiffened structure is a unified body from the covering and includetaking the two root stiffened strips and its "boundary constraints". This kind of computation model causes the rigid support that is provided by the stiffened strip on the covering to reflect that the influence in the total rigid matrix and the edge element on the intermediate covering is very small. This

viewpoint can obtain further proof of this fact of "the stiffened strip acts as the spacing wave" from the test phenomenon.

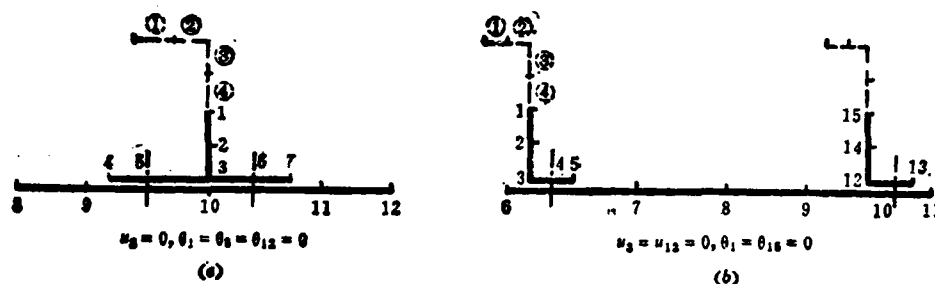


Fig. 10. Simplified computation model

IV. CONCLUSION

In the previous sections we carried out analysis of computation models. In the conclusion we will discuss several problems of the moment of force distribution method.

The moment of force distribution method [4, 5, and 6] is an extremely effective method in local stability computations. It is worked out into composed loose-leaf material by the English Royal Academy. It is drawn into curves for several kinds of typical structures [4, 5]. Because the scope of aircraft structural parameters is very large, reference [6] gives the rigid curves of some simple panel elements. Therefore, based on the standard panel element being linked with the rigidity criterion, we can compute the local buckling stress of the structure. Although this method can obtain satisfactory results for very many structures, computing is an extremely overelaborate procedure.

Additionally, the moment of force distribution method

considers that when a structure buckles, the attachment line of each formed panel element remains invariant in space. The panel elements converging on the same attachment line rotate by means of the same angular winding attachment line. We think that only considering that the angle of rotation of the attachment line convergence points are the same is not enough, and we must also see whether or not the displacement and angles of rotation of the points on the corresponding panel element are symmetrical. The moment of force distribution method does not discuss the symmetry of the deformation mode after buckling of the corresponding panel element. In fact it considers that the displacement and angles of rotation of the corresponding panel element are symmetrical, and based on this kind of assumption gives computation formulas and numerous curves. Clearly this consideration is very suitable for symmetrical structures. However, as to the asymmetrical rivet-joint (or spot-welded) stiffened structures, the buckling deformation mode is not symmetrical. The moment of force distribution method assumes this structure's independent effect on each composed panel element, and only moves the rotation with the attachment line of other panel elements (it does not move the rivet-joint line rotation). In this way, the originally unsymmetrical structure becomes a symmetrical structure. In the computation process, there obviously is an approximate processing method.

As to the glue-joint stiffened panel, the glue-joint panel elements link into an "entire body". Naturally, the rigidity of the link of this entire body panel element to some extent increases more than that of the single point. However, the moment of force distribution method does not consider this increase, but utilizes the same assumption as with rivet-joint conditions [6]. This kind of assumption clearly has great differences with the real structures.

From the three curves (a), (b), and (c) in Fig. 6 we see that computed curve A of the moment of force distribution method has a higher K value than curve B of the local unit. The reason for this is that, aside from its regarding the asymmetrical structure with symmetrical structure processing, it also expresses the two end bending moments of ventral panel b (see Fig. 1(d)) of the "Z" model stiffened strip as the two equivalent symmetrical moments of force (model II) that correspond to angle of rotation $\frac{1}{2}(\theta + \phi)$ and mutually superposes with the two equivalent unsymmetrical moments of force (model III) that correspond to angle of rotation $\frac{1}{2}(\phi - \theta)$ [4,6]. However, the unsymmetrical moment of force is not the buckling form that was sought, leading to an even higher K value.

The finite element method is extremely convenient for computation model processing, it completely does not need to use the above unrealistic assumptions.

The computation model of the local unit omits the edge element. Mechanically, it has obvious physical significance, but mathematically it still lacks the conclusion of computed error analysis.

Comrades Tong Xianxin, Fan Shirong, Rong Hongqun, and others made corrections and rendered assistance in the process of completing this paper. The computer program was compiled with the help of Comrade Chen Wenpu. I would like to express my thanks here to all of these people.

References

- [1] J.S. Przemieniecki, Finite Element Structural Analysis of Local Instability, AIAA J. Vol. 11, No. 1973. pp 33-39.
- [2] "Preliminary Research on the Finite Element Method For Local Buckling Stress of Stiffened Panel in Axial Compression", Fu Dan Da Xue Bao [Fu Dan University Journal], Vol. 3-4, 1974, pp 74-84.

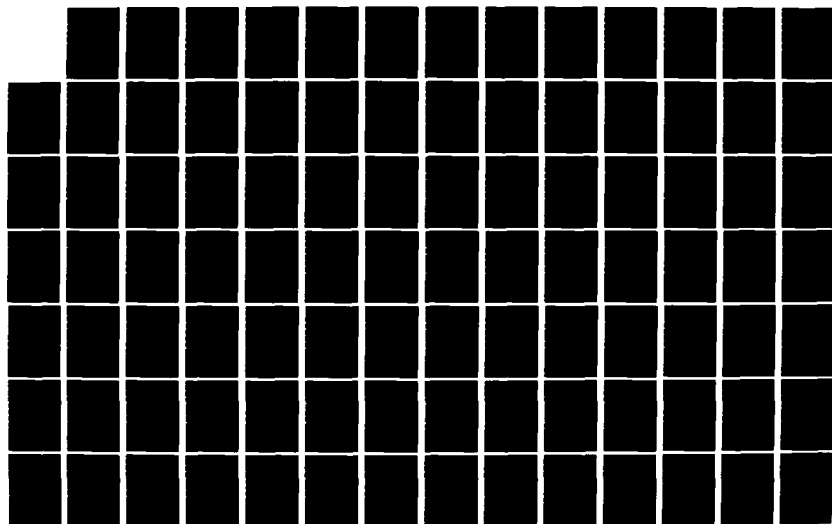
AD-A127 983

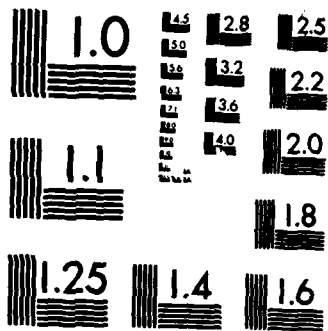
ACTA AERONAUTICA ET ASTRONAUTICA SINICA(U) FOREIGN
TECHNOLOGY DIV WRIGHT-PATTERSON AFB OH F QIAN ET AL.
04 MAR 83 FTD-ID(R5)T-0664-82

2/3

UNCLASSIFIED

F/G 20/4 NL





MICROCOPY RESOLUTION TEST CHART
NATIONAL BUREAU OF STANDARDS-1963-A

References (continued)

- [3] O.C. Zienkiewicz, The Finite Element Method in Engineering Science (1971) pp 413-432.
- [4] ESDU 7104, Local Buckling of Compression Panel with Flanged Stringers.
- [5] ENGINEERING SCIENCES DATA ITEN No. 70003: Local Buckling of Compression Panels with Unflanged Integral Stiffeners.
- [6] Engineering Sciences Data, Aeronautical Series Structures Sub-Series, Vol. 2, 02.01.28 Information on the Use of Data Sheets 02.01.29 To 02.01.37 (1957).

A UNIVERSAL METHOD FOR SOLVING THE TWO-DIMENSIONAL CASCADE WITH FREE STREAMLINE BOUNDARIES

Chen Jingyi
Institute of Engineering Thermophysics, Academia Sinica

ABSTRACT

This paper proposes a new solution method of two-dimensional cascade in which the free streamline boundary conditions can be satisfied. This is a cross-iterative calculation method between two correlated flow fields. The two-dimensional subsonic flow field problem for calculating the upstream and downstream regions of the ordinary cascade, the splitter blade cascade and the tandem cascade is discussed from a unified viewpoint. The computer program can be used for these three cases.

A physical condition of minimum disturbance of the flow field is proposed for calculating the splitter blade cascades and tandem cascades so that the rate of flow distribution ratio of the two blade channels formed by the splitter blade or the splitter stream surface can be calculated.

Some results of numerical calculations are presented and compared with the experimental data. The calculations and comparisons have proved preliminarily the rationality of both the method in this paper and the proposed physical condition for calculating the rate of flow distribution ratio. Some useful ideas are also given concerning the aerodynamic design of the splitter blade impellers.

I. FOREWORD

Related literature on the calculation of two-dimensional subsonic speed cascade flow fields are too numerous to mention

individually. We can say it is a mature problem, but the designers with considerable ingenuity, in order to meet the needs of modern high speed and high load blade mechanism, also developed some splitter blade cascades (also called long-short blade cascades) and tandem cascades (also called slot cascades) with new and original structures. All of them have excellent effects on improving the performances of the blade mechanisms. This poses new requirements for workers carrying out aerodynamic calculations of the blade mechanism. Furthermore, even the calculations of the upstream and downstream regions of the ordinary blade are very hard to process. The common characteristics of the above conditions are that they all have existing free streamline boundaries, and the difficult point in the computation method lies in how to satisfy the free streamline boundary conditions. This paper sets out from this phenomenon, discusses their flow characteristics in a unified manner and proposes a cross-iterative universal method between the two correlated flow fields.

II. THE FREE STREAMLINE AND THE BOUNDARY CONDITIONS OF THE FREE STREAMLINE

Subsonic flow field computations of the ordinary cascade can be regarded as the processing of the inner boundary value problem. If the solution is sought in the inner region of the closed boundary $A'ABB'D'DCC'$ (Fig. 1(a)) but is different from the typical inner boundary value problem, at this time one part of boundary AB and CD is the solid boundary of the blade and its form is fixed; the other part is then the fluid boundary, generally called the free streamline boundary, or seeing that they flow through the blade's front and back stationary points, it is also called the stagnant streamline boundary. For example, in order to determine their form in $A'A, C'C, BB'$, and DD' shown in Fig. 1(a), it is necessary to introduce new physical conditions. These are the cyclic conditions that are derived from annular

cascade characteristics. The velocity vectors on A'A and C'C, and BB' and DD' are then corresponding and equivalent. Now looking at the splitter blade cascade shown in Fig. 1(b), the entire solution region is still the inner boundary value problem for closed boundary A'ABB'D'DCC', but as to closed boundary ES'FP' an outer boundary value problem also forms. In order to solve and simultaneously satisfy these two groups of boundary value conditions, we can assume there is a free streamline (the stagnant streamline of a small splitter blade) E'E and FF', and the whole solution region is artificially divided into the two regions of A'ABB'F'FEE' and E'EFF'D'DCC'. When this cascade is solved the conditions it must satisfy are:

1. A'A and C'C and BB' and DD' should satisfy the cyclic conditions which are called the stagnant streamline conditions of a large blade.
2. E'E and FF' should satisfy the linking conditions of the two regions which are called the stagnant streamline conditions of a small blade.
3. Determine the physical conditions of the rate of flow distribution ratio of the two regions.

The first is the same as for the ordinary cascade. The second and the third then are the new problems brought by splitter cascades.

The solution of tandem cascades is completely the same as that for splitter blade cascades. This can very easily be seen from A'ABB'D'DCC' in Fig. 1(c) or in the solution region that is enclosed by E'EFF'H'HGG'. Noting which regions can be computed, so long as they satisfy the previously stated three conditions of computing the splitter blade cascade, then we see from the cyclic conditions that the flow fields in regions A'ABB'F'FEE'

and $C'CDD'H'HGG'$ are equivalent.

There is also the contained separation region condition as shown in Fig. 1(d) which in the same way should satisfy the cyclic conditions of stagnant streamline $A'A$ and $C'C$ and BB' and DD' . However, what free streamline ss' should satisfy is the linking conditions of the two flow regions with different properties and aside from this also must establish and determine the physical conditions of the rate of flow ratio. In analyzing this flow phenomenon, we must consider the characteristics of the three-dimensional flow of the actual viscous gas. This problem is attracting the interest of many research workers.

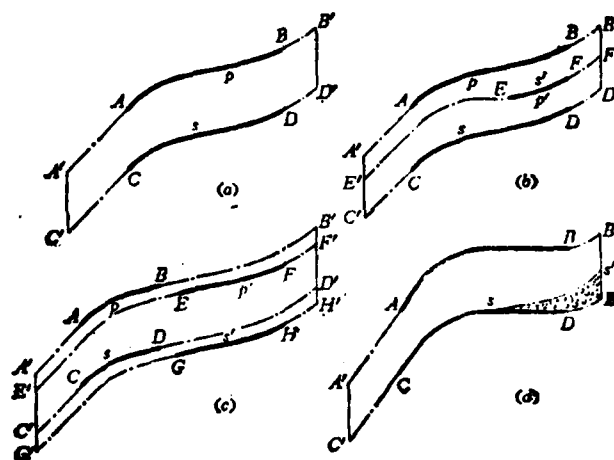


Fig. 1

III. COMPUTATION METHOD OF ORDINARY CASCADE UPSTREAM AND DOWNSTREAM REGION FLOW FIELDS

When using the streamline iteration method to compute the two-dimensional cascade flow field, to date there still is no suitable method as to how to cause the upstream and downstream regions to

satisfy the stagnant streamline conditions. The solution method in reference [1] makes the approximate assumption that the circumferential velocity distribution is a linear pattern. Reference [2] develops a method of iteration root extraction for the stagnant streamline position of a point adjacent to the blade head according to the cyclic conditions. However, it is difficult to extend it to tandem conditions. This paper proposes a universal solution method of cross-iteration between two correlated flow fields, in which one flow field is the original flow field constructed by the given solution region A'ABB'D'DCC', and the other which uses any free streamline in the original flow field — usually a free streamline with a rate of flow ratio of 0.5 is selected as the boundary based on flow field E'EFF'H'HGG' composed from a cascade pitch width — is called the correlated flow field of the original flow field (Fig. 2). We can see that the correlated flow field is the problem of the composite inner boundary and outer boundary values of a splitter blade. Beginning from the previously mentioned conditions, when actually computing we should artificially regard C'C and DD' as separately belonging to the two streamlines of C'CsDD' and C'CpDD'. Its center section separately belongs to surface p and surface s of blade CD and the two end sections then coincide with each other. Thus it automatically satisfies the linking conditions. When the solution must differentiate the flow iteration, that is the front and back sections of blade CD use a given rate of flow, and in EFDC and CDHG each is half according to the given rate of flow (when E'F in the original flow field is a 0.5 flow streamline), yet streamline iteration still is carried out in a unified manner in the whole region.* It is the same as the

* The idea of this unified solution is proposed by Professor Wu Zhonghua and the computations used for the long-short cascades were developed by Comrade Liu Diankui. Professor Wu Zhonghua also pointed out the importance of computing the rate of flow distribution ratio. The author expresses sincere gratitude for their guidance and suggestions.

ordinary cascade solution up until the streamline and velocity of the whole field converge on the small arbitrary fixed amount.

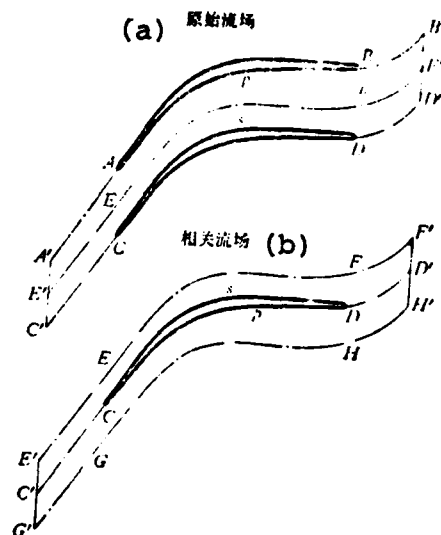


Fig. 2.
Key: (a) Original flow field: (b)
Correlated flow field.

Now we will analyze the mutual influence of the two correlated flow fields. We begin computations from the original flow field. Because the stagnant streamline boundaries $A'A$ and BB' (and the corresponding $C'C$ and DD') are arbitrarily given, therefore the velocity on its surface generally cannot be correspondingly equivalent according to cyclic conditions, but on free streamline $E'F'$ the velocity clearly has only one value. Afterwards, we shift to correlated flow field computations. At this time, streamlines $A'B'$, $E'F'$, and $C'D'$ in the original flow field will successively turn into the streamlines $C'pD'$, $E'F'$, and $G'H'$ and CsD' in the correlated flow field and then the mutual transformation of the boundary streamlines and inside streamlines will occur. Its result is that the velocity on

E'E and G'G, and FF' and HH' will not again be correspondingly equal (although as the boundary streamline its form is invariant). What is even more interesting is that the forms of C'C and DD' will be variable but their velocity becomes single. This is the stagnant streamline condition which is hopefully satisfied in the original flow field. Therefore the correlated flow field computation is equivalent to making corrections once on the form of stagnant streamline C'C and DD'. It can well be regarded as a new, even more reasonable assumption to newly shift to the original flow field. In this way, the computation of the two correlated flow fields repeatedly cross-iterate until they mutually coincide, then on the stagnant streamline C'C and DD' (and corresponding A'A and BB') both satisfy the cyclic conditions. This is the required end solution.

The basic steps of the computing formula and each flow field solution are presented in reference [2], and so we will not repeat them here. Using the above method to newly compute the turbine cascade with an inlet of $M=0.42$ given in reference [3], the result is satisfactory and the entire upstream and downstream regions both satisfy the cyclic conditions of the stagnant streamline very well (Fig. 3).

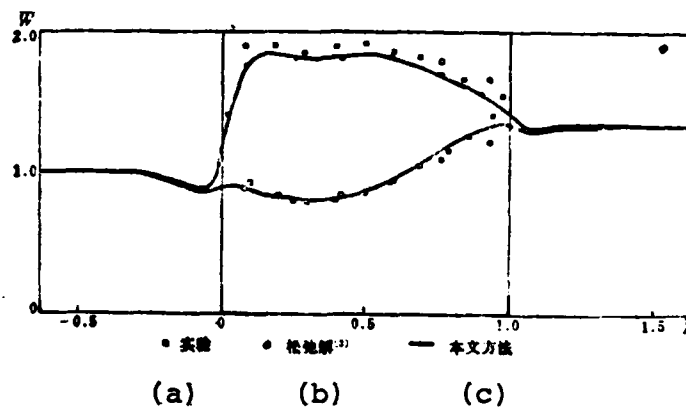


Fig. 3.

Key: (a) Test; (b) Relaxation solution [3];
(c) Method of this paper.

We carried out many tests on cross-iteration formulas of the two correlated flow fields; we can utilize the original flow field as the basic flow field, and every iteration will accomplish streamline convergence. However, with the correlated flow field as the corrected flow field, every iteration of the cross method only corrects the streamline once; we can also use the synchronous iteration method of immediate crossing between the two flow fields (all only make one streamline correction). Whether or not the computations are completed is determined according to the two standards of the precision of the two correlated flow field streamlines coinciding with each other and the precision of the original flow field streamline convergence. They both require a streamline angular coordinate error of not more than 0.0002. Computations show that these two coordinates basically can be synchronously reached.

Additionally, we also carried out tests based on a method proposed in reference [2], but we extended it to many computation points for separate root extraction on the upstream and downstream. Because we have not given consideration to the

characteristics of both the front and rear influences of the subsonic flow field, at this time we can only succeed to approximately satisfy the cyclic conditions. Therefore, we can assume that with the so-called method of solving the direct problem according to the pattern of the inverse problem it is hard to obtain satisfactory convergence precision.

IV. COMPUTATION METHOD FOR THE SPLITTER BLADE CASCADE AND THE TANDEM CASCADE

Referring to Fig. 1(c), with the first region A'ABB'D'DCC' found from the cascade viewed as the original flow field, and the second region E'EFF'H'HGG' formed from the cascade viewed as the correlated flow field, then they are the same as the ordinary cascade. Using the computed cross-iterations of these two flow fields, we thus can at one stroke obtain results to simultaneously satisfy the stagnant streamline conditions of the two cascades. Clearly this solution method also is in the same way suitable for splitter blade cascades and therefore we can use the three conditions together as a universal computation procedure. Partial examples of applying this computer program are as follows:

1. Splitter blade cascade: The computed example takes a tested centrifugal impeller and in the coordinates $L \sim \varphi$ (L is the meridian streamline length, φ is the angular coordinate) Fig. 4 shows its blade model line that is close to the inner wall rotation surface. Fig. 5 is an assumed splitter blade plan which is constructed by placing the small blade in the cascade channel center with the radius of the same kind of model line as the large blade. In the computations, the temporarily assumed rate of flow ratio is 0.49, that is $G_1 = 0.496$ and comparing the velocity distribution obtained in the computations which is shown in Fig. 7 to the ps load of the ordinary cascade (Fig. 6), the splitter blade cascade obtains satisfactory uniform load

results. The streamline distribution is also shown in Figs. 4 and 5. After contrasting we can clearly see that the streamline which the small blade gives rise to is newly distributed.

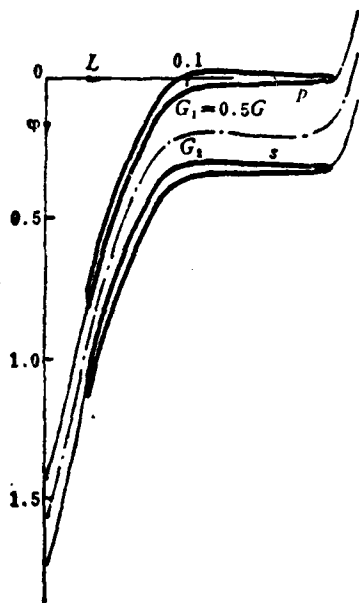


Fig. 4

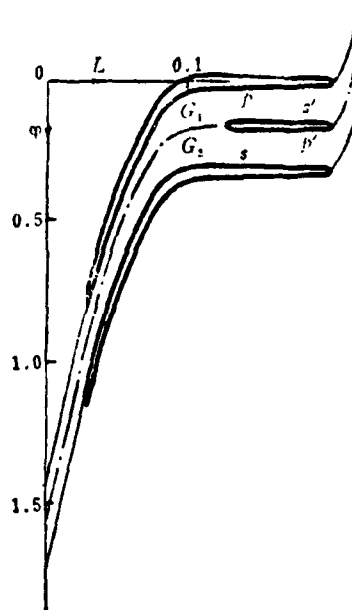


Fig. 5

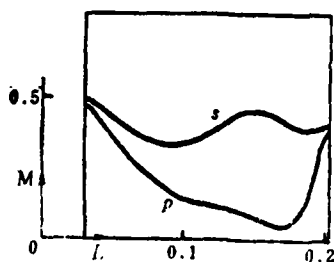


Fig. 6

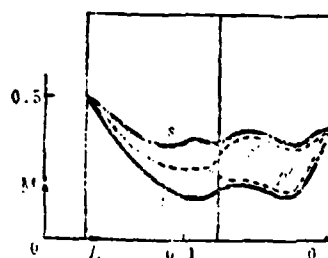


Fig. 7

2. Tandem cascades: The computer example takes a designed plan of a backward bent impeller and Fig. 8 is its cascade model that is close to the exterior wall rotation surface. Fig. 9 is an assumed tandem impeller plan. In the computations, the temporarily assumed rate of flow ratio is 0.77 ($G_1=0.77G$),

and the velocity distribution is shown in Figs. 10 and 11. Especially note that the first cascade velocity distribution which is expressed by solid line p_s merges into one line in the second cascade and the second cascade velocity distribution which is expressed by dotted line $p's'$ also merges into one line in the first cascade. This shows that the stagnant streamline conditions of the first and second cascades all obtain satisfaction. The streamline distributions (Figs. 8 and 9) clearly indicate the mutual influence of the two cascades which causes the streamline turning to emerge in the tandem slot.

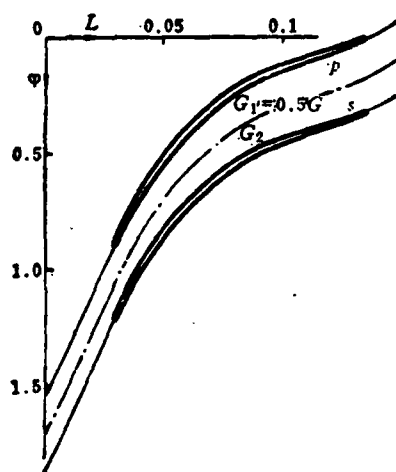


Fig. 8

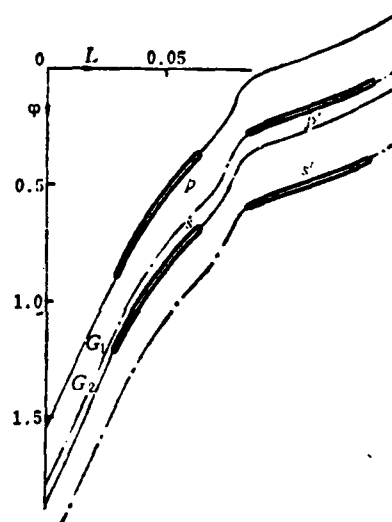


Fig. 9

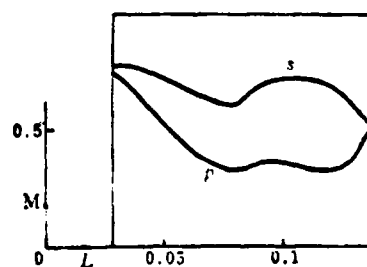


Fig. 10

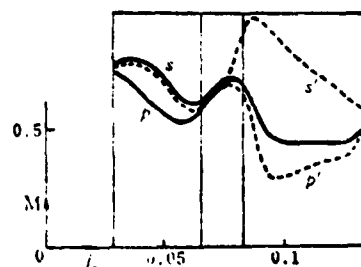


Fig. 11

All streamlines have places of sudden turning, for example the space area of the tandem impeller and the outlet area of the centrifugal impeller (including the splitter blade plan). In the computations with each iteration, the amount of streamline modification is very small and convergence is extremely slow. This is the same phenomenon as the extreme sensitivity of the velocity distribution of the front and back edges of the blade on the stationary point position; but the back ones are even more extreme — a sharp point emerges on the streamline turning and a singular point emerges in the flow field computations. Therefore, it is not possible for stringent stationary point computations to utilize the streamline iteration method.

V. PHYSICAL CONDITIONS AND COMPUTATION METHOD OF DETERMINING RATE OF FLOW DISTRIBUTION RATIO

How the rate of flow distribution ratio between the two blade channels that are formed by splitter blades or splitter surfaces is determined is a problem that urgently needs to be solved in splitter cascade and in tandem cascade computations.* This paper proposes the physical conditions of a flow field with minimum disturbance, wherein we can compute and obtain the rate of flow. Its basic idea is to take the splitter blade as a source of flow field disturbance, because when there is subsonic flow its disturbance must spread towards the whole field thereby causing the new distribution of the original non-splitter blade flow field streamline. Therefore, we will use the root mean square value

$$\bar{\varphi} = \sqrt{\left(\sum_{j=1}^n \varphi_j^2\right) / n}$$

(in which n is the nodal point number), of the difference of the streamline angular coordinates on all of the

* Reference [4] correctly raised this point in the beginning of the 1960's.

nodal points of the two flow fields of contained and not contained splitter blades to express this disturbance amount; on the other hand, many extreme value phenomena are similar in physics, and from the point of view of energy dissemination this new distribution should adhere to the principles of minimum disturbance. In mathematics, this will manifest as the functional relationship that possesses minimum extreme value which exists between the rate of flow distribution ratio and the flow field disturbance quantity. From this relationship we can then compute and satisfy the rate of flow ratio of the minimum disturbance conditions which is also the rate of flow ratio of the actual flow.

Below, we will further explain by means of a few specific examples:

1. In Fig. 12(a), if the small blade is immeasurably thin and its form is completely identical with the streamline of the original flow field without a small blade, then we cannot bring about the new streamline distribution and the rate of flow ratio also has no variation. At this time, minimum disturbance conditions are automatically satisfied.

2. In Fig. 12(b), from the upstream region of the small blade we see that the streamline has no new distribution, and seemingly the rate of flow ratio also is invariable. However, from the downstream region minimum disturbance conditions we see that the rate of flow distribution should reduce the variation towards G_1 .

3. In Fig. 12(c), from the upstream region minimum disturbance conditions we see that $G_1 > G_2$, and from the downstream region we see that $G_1 < G_2$. The actual rate of flow ratio should be determined by the minimum disturbance conditions of the whole field.

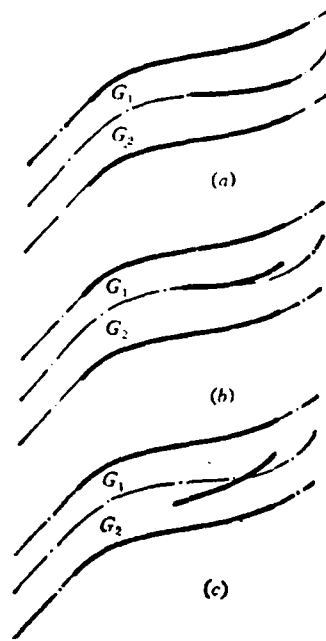


Fig. 12.

In actual computations, we can start out from an arbitrarily assumed rate of flow ratio. By comparing the flow field parameters that the computations obtain and the original flow field parameters of the source without disturbance, and using the previously mentioned root mean square value for expression, the computer program can use any root extraction method to compute and satisfy the rate of flow ratio of minimum disturbance conditions.

According to this method we newly compute the splitter blade cascade introduced in the previous section. Fig. 13 gives its iteration root extraction procedure. Computed results prove the existence of minimum extreme values, the rate of flow ratio at this time is $G_1=0.417G$ and the corresponding velocity distribution is shown in Fig. 14.

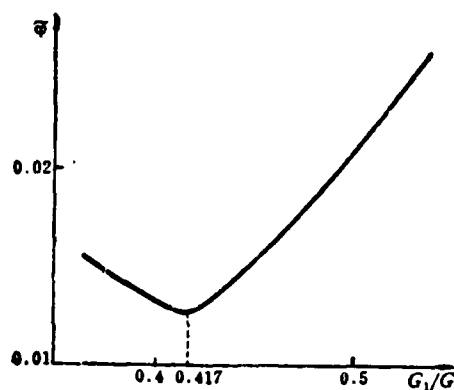


Fig. 13

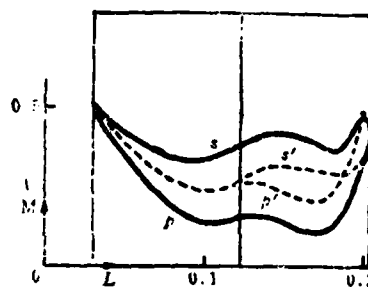


Fig. 14

Contrasting with Fig. 7 we see that at this time the load sustained by the splitter blade is much smaller than the splitter blade load when the rate of flow ratio is 0.49. Moreover, velocity distribution crossing also occurs in the area of the outlet. This is because the rate of flow of the splitter blade outlet section simultaneously endures the constraints of the stagnant streamline conditions of the large and small blades (they are frequently mutually contradictory). What corresponds with this is possibly a separated flow condition. For this reason, we can see the importance of determining rate of flow ratio computations. When the rate of flow ratio is 0.49 we can no doubt obtain satisfactory uniform load results but the rate of flow ratio and the uniform load effect in reality are not like this. This shows that there are considerable beneficial conclusions for the actual design. A splitter blade design with the same kind of form as the large blade laying in the center of the blade channel is not completely reasonable, and specialized computation and design should be conducted on both the position and the form of the splitter blade.

In order to further test and verify the rationality of this computation method, we utilized the exploratory research carried

out in the 1960's presented in reference [5] — test data on large and small cascades with expanded surge margins.*

Fig. 15 is the sectional drawing of these large and small cascades and the ordinary cascades that are compared with them; Fig. 16 is the comparison of computations and tests under an angle of attack in which the comparison of the ordinary cascade is perfectly satisfactory; the rate of flow ratio that the computations obtained of the large and small cascades according to the principle of minimum disturbance is $G_1=0.47G$ (it is not $0.5G$) and the corresponding pressure distribution basically is also satisfactory. Fig. 17 gives the computed results of the other two rate of flow ratios (0.45 and 0.5). We can see that the rate of flow ratio goes from 0.5 to 0.47 and again to 0.45. The variation of the large and small cascade pressure distribution is very marked and therefore the common customary formulated rate of flow ratio is 0.5. Thus the designers can satisfy the uniform load results that the computations obtain but the experiments prove that this does not coincide with reality. Conversely, if the computation method is not dependable, for example the rate of flow ratio that is obtained tends to lower to 0.45, then again it is possible to create a false impression that a small cascade cannot bear a load at all. Additionally, the pressure distribution of a cross type which appears in the small cascade of Fig. 16 can be improved through a particular design of the small blade. This is also precisely the place where the aerodynamic design workers can give full play to creativity.

* The author is deeply grateful to Professor Cui Qiya for his enthusiastic support and guidance for this paper.

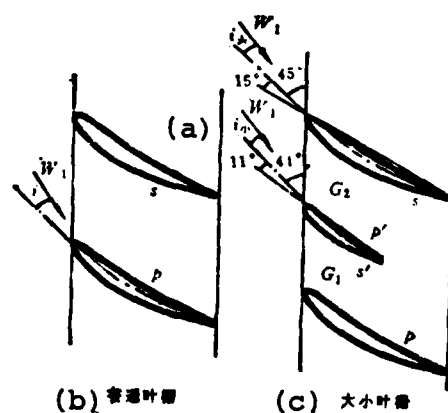


Fig. 15.
Key: (a) Ordinary cascade;
(b) Small; (c) Large and
small cascades.

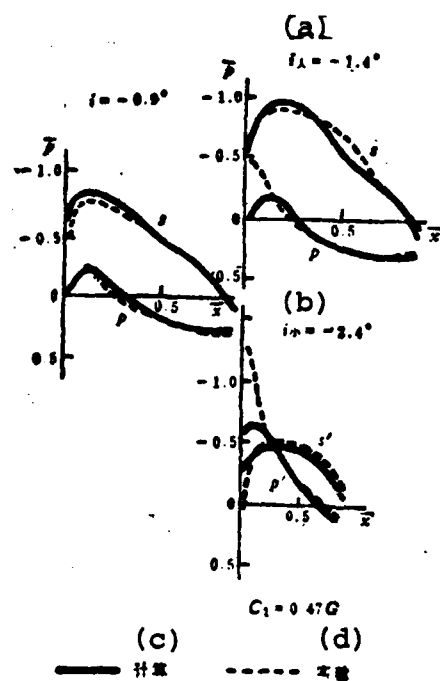


Fig. 16.
Key: (a) Large; (b) Small;
(c) Computed; (d) Tested.

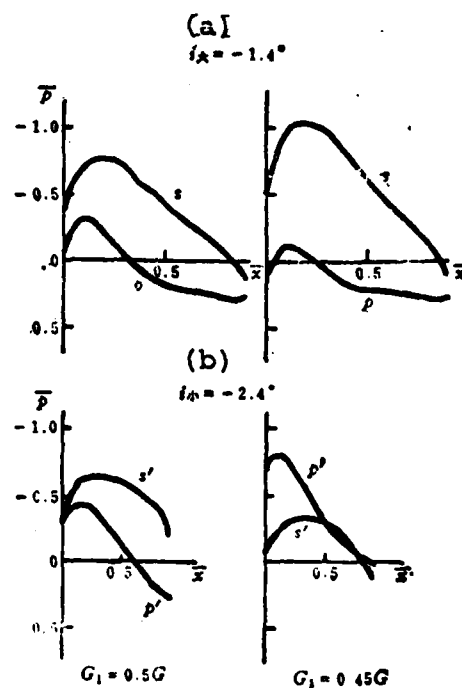


Fig. 17.
Key: (a) Large; (b) Small.

VI. CONCLUDING REMARKS

This paper, based on the annular cascade characteristics of impeller machinery, proposes two correlated flow fields that are equal to one another and which can also be mutually switched. On this basis, we developed a computation method for the superposition of the solution region. It can cause each parameter to be separately computed in its most suitable region.

The method for computing the rate of flow distribution ratio that was proposed is compared with the tests. Its preliminary results are satisfactory. Therefore, the method of this paper hopefully can become a useful tool for specialized design carried out on splitter blade impellers and for flow field analysis.

We can also obtain a significant revelation from the method in this paper: although some of the aerodynamic components with new and original structures, such as splitter blade cascades or tandem cascades, have mathematical problem formations different from the ordinary cascade, the thermodynamic equations that they adhere to are still invariant and thus still abide by the same subsonic flow patterns under the assumptions of stability and without viscosity. Therefore, so long as we establish and satisfy the peculiar physical conditions of these new and original cascades, then using some solution techniques we can still transform them into solutions that use the same method as ordinary cascades. This is also the reason that the method and computer program in this paper can be universal for ordinary cascades, splitter blade cascades and tandem cascades.

The conditions of tandem cascades still await further computation analysis and comparison.

The principles of this paper can be extended to computations of three-dimensional flow fields.

References

- [1] Wilkinson, D.H., ARC RM3704, 1972.
- [2] Chen Jingyi and Liu Diankui, Ye Lun Ji Xie Qi Dong Ji Suan, She Ji Yu Shi Yan Jiao Liu Hui Wen Ji [Collected Essays from the Symposium on Aerodynamic Computations, Design, and Experiments of Impeller Machinery], 1976.
- [3] Wu Zhonghua, NACA TN 2407, 1951.
- [4] Kramer, J.J., etc., NASA TN D-1186, 1962.
- [5] Cui Qiya, Zhou Sheng, Lu Renfu, Zhang Lianchi, Gong Cheng Re Wu Li Xue Bao [Engineering Thermophysics Journal], Vol. 1, No. 2, 1980.

TESTS FOR INLET DISTORTION IN A TWO-SPOOL TURBOJET ENGINE ON THE GROUND TEST BED

Jiang Feng
Shenyang Liming Machinery Company

Abstract

Tests and their results for the effects of the inlet total pressure distortion on the performance and stability of a two-spool turbojet engine are presented. The tests are carried out on ground test beds. The engine is a two-spool turbojet engine with a three-stage low pressure compressor and three-stage high pressure compressor, a medium supercharging ratio and afterburning.

The steady state circumferential pressure distortion is created by the 90° fan-shaped mesh. We determined the relational curve of the mesh with different blockage ratios or distortion amplitude produced by the congruent mesh which follows the engine's inlet rate of flow.

Under distortion and non-distortion conditions, we separately determined the surge boundary line and operating line for an engine with first stage supersonic compressor blades with two different types of aspect ratios, gave the surge margin change patterns of the low pressure compressor and high pressure compressor, and carried out preliminary analysis by constrasting test results.

When the area of the engine jet nozzle was changed from 100% to 142% and we carried out fully steady and dynamic tests with and without distortion, the engine did not have unsteady operation. When there was no distortion, the operating line followed the variation curve of the jet nozzle area ratio.

The fuel flow step device used for the tests were successively designed and debugged by the Shenyang Liming Machinery Company and the two-spool turbojet engine was surged 42 times. We separately obtained 84 surge points for the high pressure and low pressure compressors as well as the oscillograph curve of the surging process and briefly analyzed the variation characteristics of the parameters of the surging process.

LIST OF SYMBOLS

π_c	supercharging
G	rate of flow
n	rotational speed
p	pressure
T	temperature
\bar{D}	degree of inequality
DC90°	index number of pressure distortion

FOOTNOTES

1	low pressure compressor; low pressure compressor inlet section
2	high pressure compressor; high pressure compressor outlet section
x	low pressure compressor outlet section
T	fuel
B	air
hs	conversion
4	turbine rear section
dy	low pressure
gy	high pressure
*	stagnant parameter
—	corresponding value

I. POSING THE PROBLEM

Supersonic aircraft with M number greater than 2, due to such factors as maneuvering flight, spent gas induction of launched weapons and uncoordinated changes in inlet duct/engine operating conditions, will bring about inlet distortion. This is an outstanding problem in the development of supersonic propulsion systems.

Distortion reduces the compressor surge margin and when it is severe it causes stalling, surging and even stopping in space. Especially near the flight boundaries of high altitude low surface speed, when the margin of the stability of the compressor is comparatively tense, it can bring about the decline of the anti-disturbance ability of the propulsion system and influences flight safety and fighting applications. Therefore, determining the engine stability operation margin and the anti-distortion ability is indispensable work in the development of new types of propulsion systems.

II. TEST DEVICES

ENGINE: The first stage compressor uses two aspect ratio blade models for separate tests which are arranged in Table 1. Blade model 5P has a small chord length and a total of 31 blades; model GO2 has a chord length which is increased by $1/3$ and the blade number is reduced to 24.

DISTORTION DEVICE: It is glued on the steel-made wide strip bracket by the three 90° fan-shaped wire meshes of items 4, 12 and 72 and positioned in the engine inlet's front 0.75 diameter section. It produces the necessary circumferential total pressure static-state distortion (see Fig. 1).

TABLE I

Mesh number		4	4+12	4+72
Blockage ratio (%)	14.5	25	25+30	25+69
Nominal distortion degree	0	0.07	0.11	0.17
GO2 test	test	test	test	test
5P test	test		test	

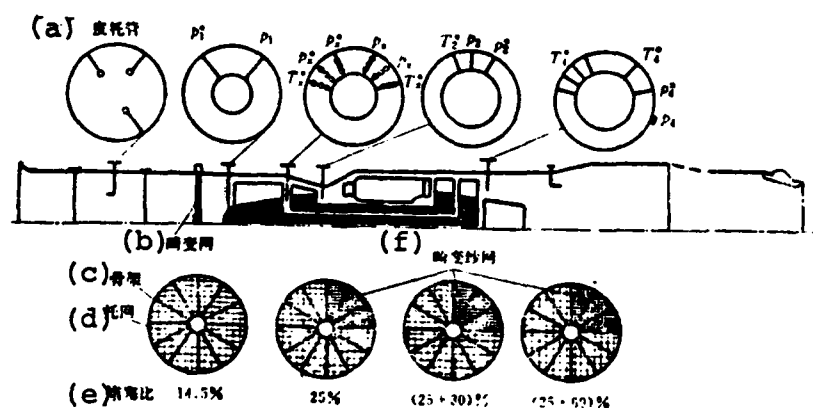


Fig. 1. Simplified diagram of installed position of distortion device and measured affected section.
Key: (a) Pitot tube; (b) Distortion mesh; (c) Framework; (d) Bracket mesh; (e) Blockage ratio; (f) Distortion wire mesh.

MEASURING DEVICE: Fig. 1 shows the inlet disturbance flow device, inlet measuring section, low pressure compressor inlet distortion measuring rake, low pressure compressor outlet and the turbine rear total static pressure, the equipment position of the measured affected section of the total temperature, and the measuring point number. The air inlet measuring section installation has a Pitot tube and combination solid pressure sensor. The low pressure compressor inlet distortion measuring rake is a total pressure radial ten point composite affected section, the undistorted region is a total pressure five point affected section, and this section only uses the steady-state to determine the distortion amplitude. High and low pressure compressor

outlet section total static pressures both utilize the solid pressure sensor. Each parameter is designed with steady-state and dynamic-state measuring devices and in the process of each surge the starting point uses a steady-state system with fairly high precision to carry out immediate calibration on the dynamic-state system.

FUEL STEP AND ITS DEVICE: In some forced surge plans, after tests, we select the fuel step as the means of forced surge for the characteristics of the two-spool turbojet engine and the conditions of the equipment. A sudden sharp increase of the fuel amount to a certain value and maintained for more than 0.4 seconds is called the fuel step. It gives rise to engine fast speed acceleration. Because the temperature of the combustion chamber outlet rapidly rises, the fuel flow of a high temperature and high specific volume produces flow accumulation in front of the blocked turbine guide causing the pressure to suddenly increase and giving rise to stalling and surging of the high pressure compressor. Later, depending on the supercharge effect of the increase of the pressure of the surge hammer blow waves forward dissemination, it causes the upstream expulsion to successively surge forward with the low pressure compressor and obtain a surge point. Tests indicate that because the two-spool turbojet engine surge resistant ability is fairly strong, the ground high rotational speed surge is difficult. The fuel step device must give suitable fuel step amounts and fuel step amounts according to the different surge starting conditions of the engine and then the forced surge goal can be reached.

The fuel step device of this test is accomplished by meticulously retrofitting and debugging the auxiliary fuel pump of the ground facility and engine fuel adjustor. It can suddenly increase over 2 1/2 times in 0.1 to 0.2 seconds with supplied fuel, ensuring that the engine will surge under suitable fuel step amount and fuel step speed.

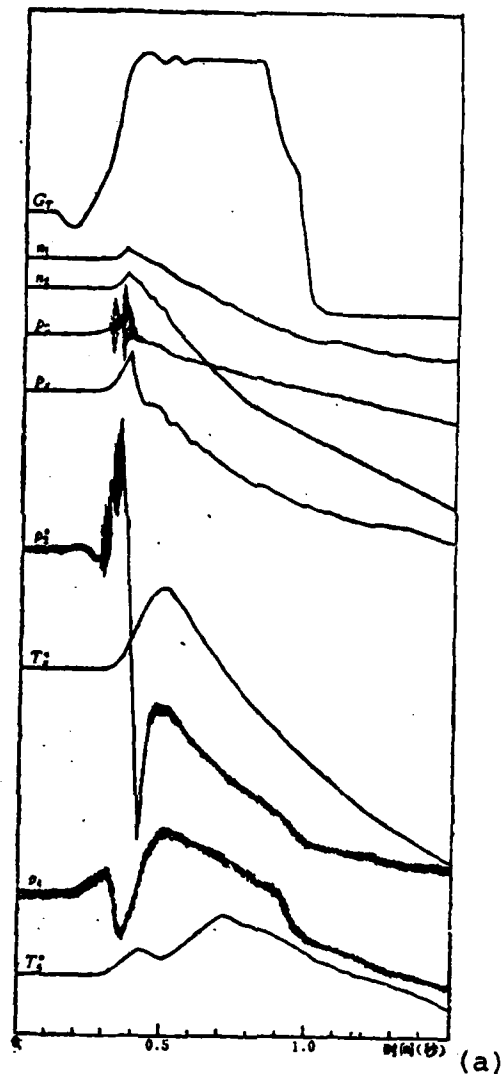


Fig. 2. Fuel step surge process.
Key: (a) Time (seconds).

III. DISCUSSION OF TEST RESULTS

1. Influence of Nozzle Area Variation on Operating Line

Using uniform flow field experiment curves as examples, the engine nozzle area increases from normal state 100% to 113% and 142%, the low pressure compressor operation line shifts on the

left, the pressure ratio increases approximately 3% and the rate of flow reduces approximately 4%. The high pressure compressor's variation direction is opposite and moreover it is more sudden than that of the low pressure compressor. The pressure ratio drops approximately 11% and the rate of flow increases approximately 8.5% (see Figs. 3 and 4).

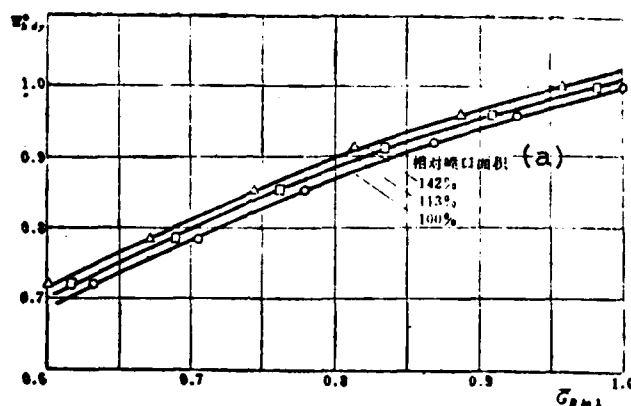


Fig. 3. Influence of nozzle area transformation on low pressure compressor operating line.
Key: (a) Relative nozzle area.

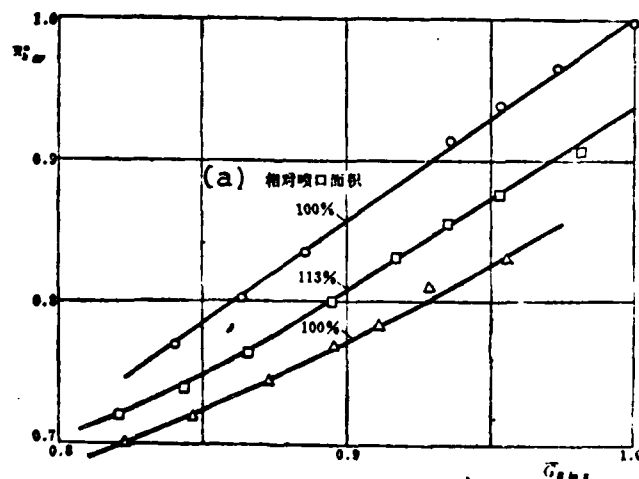


Fig. 4. Influence of nozzle area transformation on high pressure compressor operating line.
Key: (a) Relative nozzle area.

Because the nozzle magnification gives rise to a very small shift of the low pressure compressor's operating line, it continually increases the area to 188% and the surge margin still does not have a large reduction so that it cannot cause the operating line to intersect with the surge boundary. This proves that by depending on this method alone, we cannot obtain the low pressure compressor's surge point.

2. Pressure Distortion

As to model GO2, based on the wire mesh of the three blockage ratios selected in Table 1, we determined the functional relation curve of the engine's conversion rate of airflow following unequal degrees \bar{D} and $DC90^\circ$ (Figs. 5 and 6). \bar{D} variation is comparatively sudden, $DC90^\circ$ is basically invariant in the range of low rate of flow and the high rotational speed then rises. But whether \bar{D} or $DC90^\circ$, it follows the wire mesh blockage ratio more strikingly than different changes. This explains that the distortion amplitude primarily hinges on the porosity of the mesh (see Table 2).

3. Characteristics of Surge

The curve of fuel step surge selected from 42 surge oscillographs under conditions of quasi-uniform air inlet is an example for analyzing the engine's primary parameter variation characteristics (see Fig. 2).

The fuel flow assumes a step type jump increase. It jump increases from the initial value to a level peak approximately requiring 0.15 to 0.2 seconds. After the level peak is maintained for 0.4 seconds it cuts off the step switch and stalls the throttle.

The pattern of the curves of the high pressure compressor

outlet's static pressure and total pressure are identical. Prior to the surge, because the fuel step and the acceleration pressure rise, first the stalled wave pattern emerges but the pressure average value has no steep drop until the stalled wave pattern intermittence. This stall is the gradual type and it cannot bring about surge. After the intermittence, the second stall wave pattern that immediately emerges is different from the first wave. At the place where the wave crest swells, the pressure average value falls suddenly and there is a sudden change pattern stall. A steep drop in pressure indicates high pressure compressor surge and at this time the amount of fuel still does not increase to peak level. Moreover, soon afterwards it again continues to be maintained for over 0.4 seconds. This can affirm that a steep drop of pressure is an important characteristic which brings about surge. Aside from this, high pressure compressor rotor rotational speed also steps down from the increased peak because of surge and is synchronous with the average value reaction of the pressure of the compressor outlet. It can use a distinctly indicated curve of rotational speed with fluctuation that is not large to determine the surge point-time coordinates.

In approximately ten milliseconds, the forward transmitted hammer blow wave produced by the high pressure surge causes the pressure in the low pressure compressor outlet to suddenly drop from rising peak value and low pressure surge. However, the test of 42 surges and the acceleration process of 18 fuel steps have not found that the stall wave patterns below low pressure compressor surge uniformly and directly surge. Yet, the high pressure compressor always first stalls and afterwards surges or does not surge.

After surge, the compressor outlet temperature continually rises for a period of time and then drops. This is because the temperature thermoelectric couple time constant is greater than

that incurred in the pressure sensor. Surge causes the compressor outlet's pressure, rotational speed and temperature (after slightly slowing) to drop. By comparing the fuel step wave pattern we can confirm what causes unreduced fuel. This is the basic characteristic of compressor surge in the engine. When the fuel step is maintained for 0.4 seconds, the surge causes the low pressure rotational speed to drop 0.6 fold, the static pressure in the low pressure compressor outlet to drop 0.84 fold, the high pressure to drop 0.75 fold and the pressure in the high pressure outlet to drop 0.96 fold.

The turbine rear pressure oscillograph curve and fuel step begins to rise with the acceleration and then very quickly the turbine conductor upstream throttle causes the downstream rate of flow pressure to be insufficient and reduced until surge occurs and the rate of airflow suddenly drops. The uncombusted fuel pulls to the back of the turbine with the result that there is continuous combustion in the afterburner which causes the pressure to rise again. Therefore, at the same time that the sonic boom occurs, the tail nozzle emits a reddish-orange color flame of disorderly pulsation. Generally, the nozzle flame blast is the macroscopic indication of engine surge.

The sudden rise of fuel step surge rotational speed is small, that of the speed compressor approximately increases 3.5%, and that of the low pressure compressor approximately increases 3%. In the tests, when retreating surge is fairly slow, there is the phenomenon of repeated and continuous surge and each surge cycle pattern was more or less the same as the above mentioned conditions. In two times, the surge peak interval was approximately 0.1 seconds and therefore the frequency of longitudinal oscillation is approximately 10 hertz.

4. Influence of Distortion on GO2 Compressor

When the nozzle area is 100%, three kinds of distortion bring about the variations of the low and high pressure compressor surge boundary lines and operating lines shown in Figs. 7, 8, 12 and 13 are the relation of the conversion rate of flow and supercharging ratio: Figs. 7 and 8 are the relational curves of the conversion rotational speed and supercharging ratio. With the enlargement of the wire mesh blockage ratio and the increase of the distortion amplitude, the low pressure compressor surge boundaries noticeably drop, the operating line also has a slight decline, and the surge margin loss enlarges. This pattern coincides with the test results of component tests and foreign literature. The response curve of the high pressure compressor to distortion is identical with the flow pressure compressor's variation tendencies, yet the influence must be much lighter.

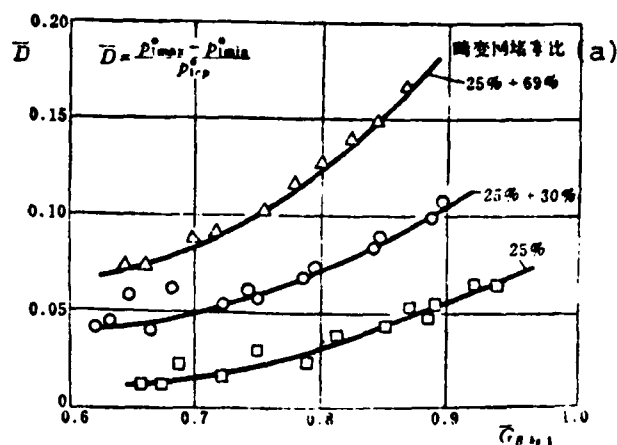


Fig. 5. Curve of relationship of distortion index and engine conversion rate of flow.

Key: (a) Distortion mesh blockage ratio.

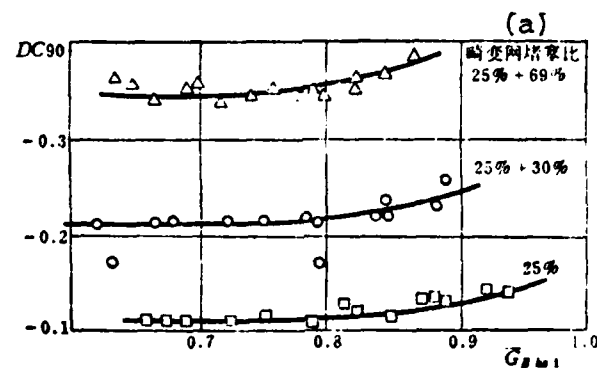


Fig. 6. Curve of relationship of distortion index and engine air-flow rate.
Key: (a) Distortion mesh blockage ratio.

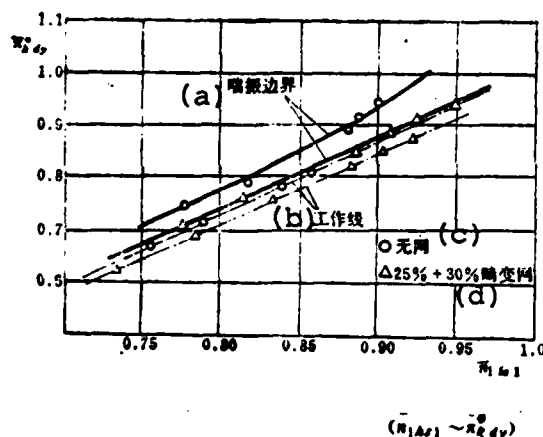


Fig. 7. Influence of (GO2) distortion on L.P. compressor.
Key: (a) Surge boundary; (b) Operating line; (c) No mesh; (d) Mesh.

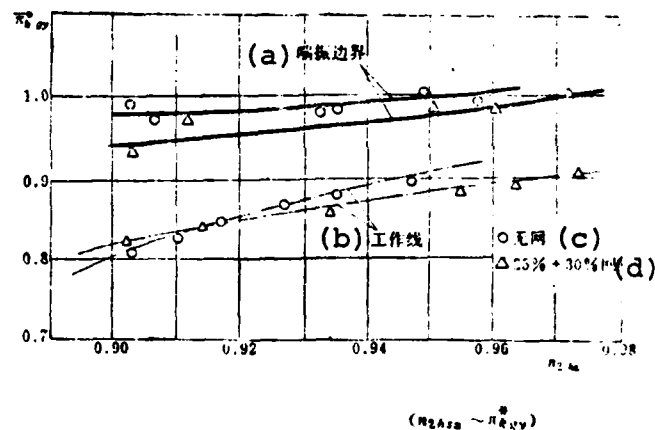


Fig. 8. Influence of (GO2) distortion on H.P. compressor.
Key: (a) Surge boundary; (b) Operating line; (c) No mesh; (d) Mesh.

Table 2. Wire mesh blockage ratio and distortion index value when relative rate of flow is 0.9.
Key: (a) Blockage ratio.

(a) 堵塞比	DC90°	\bar{D}
25%	-0.14	0.088
25% + 30%	-0.244	0.107
25% + 69%	-0.38	0.168

$$\bar{D} = \frac{P_{max}^* - P_{min}^*}{P_{0.9}^*}$$

$$DC90^\circ = \frac{P_{0.9+90}^* - P_{0.9}^*}{-\frac{1}{2} \rho v^2}$$

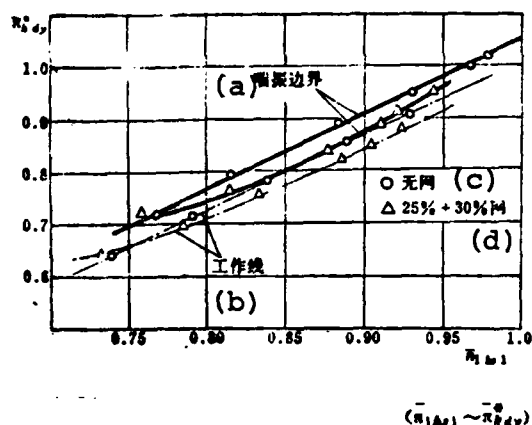


Fig. 9. Influence of (5P) distortion on L.P. compressor. Key: (a) Surge boundary; (b) Operating line; (c) No mesh; (d) Mesh.

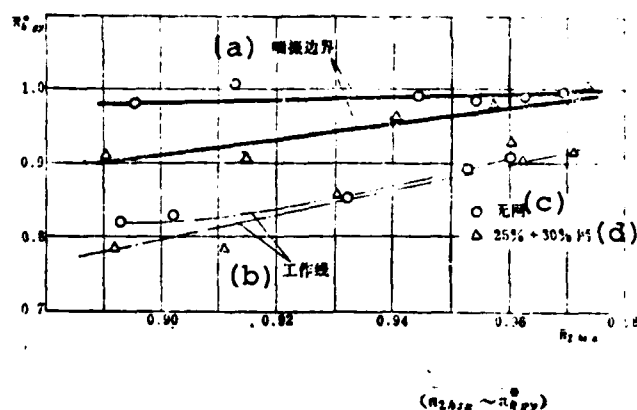


Fig. 10. Influence of (5P) distortion on H.P. compressor. Key: (a) Surge boundary; (b) Operating line; (c) No mesh; (d) Mesh.

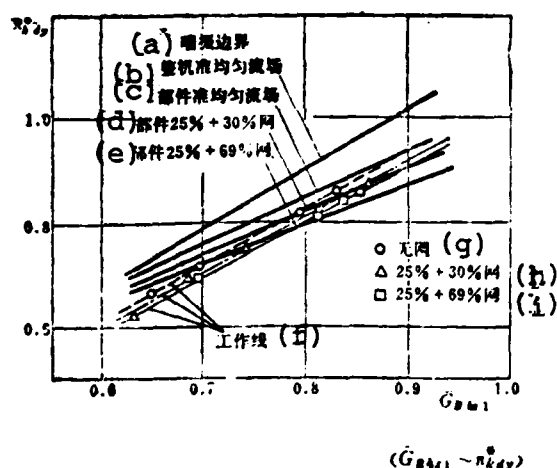


Fig. 11. Comparison of surge boundaries of whole aircraft test and component test. Key: (a) Surge boundary; (b) Quasi-uniform flow field of whole aircraft; (c) Quasi-uniform flow field of component; (d) Component 25% + 30% mesh; (e) Component 25% + 69% mesh; (f) Operating line; (g) No mesh; (h) Mesh; (i) Mesh.

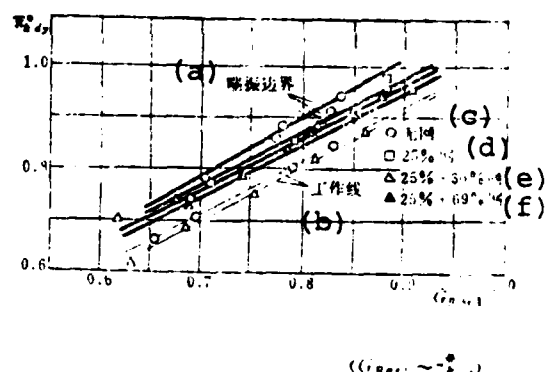


Fig. 12. Influence of (G02) distortion on L.P. compressor. Key: (a) Surge boundary; (b) Operating line; (c) No mesh; (d) Mesh; (e) Mesh; (f) mesh.

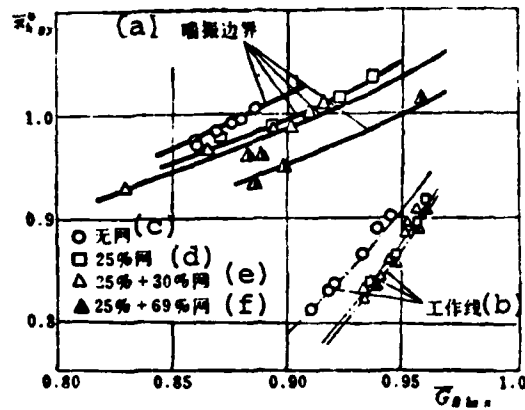


Fig. 13: Influence of (G02) distortion on H.P. compressor. ($\bar{G}_{02} \sim \pi_{02}^*$)
 Key: (a) Surge boundary; (b) Operating line; (c) No mesh; (d) Mesh; (e) Mesh; (f) Mesh.

On the basis of the characteristics of this test, we use the supercharging ratio surge margin under equal convergence rotational speed to measure the influence of distortion:

$$SM\% = \left(\frac{\pi_{02}^{(a)}}{\pi_{02}^{(b)}} - 1 \right) \times 100\%$$

Key: (a) Surge point;
 (b) Operating point.

When the unequal degree \bar{D} approximately 0.11 distortion flow field is compared to the quasi-uniform flow field, the low pressure compressor surge margin almost loses one-half, it rises with the rotational speed and the loss increases. See Table 3.

TABLE 3: SURGE MARGIN CHANGES WITH CONVERSION ROTATIONAL SPEED GO2 LOW PRESSURE COMPRESSOR

Conversion rotational speed (%)	95	90	85	80	75
Undistorted surge margin (%)	10.06	8.45	6.62	7.26	7.50
Surge margin under $D \approx 0.11$ distortion (%)	4.5	4.18	3.77	3.70	4.55
Distortion causing surge margin loss (%)	5.56	4.27	2.85	3.56	3.02
Relative margin loss (%)	55.3	50.5	43.05	49.0	39.56

Note: Relative margin loss = $\frac{\text{surge margin loss under distortion}}{\text{surge margin under no distortion}} \%$

GO2 HIGH PRESSURE COMPRESSOR

Conversion rotational speed (%)	95	94	92	90
Undistorted surge margin (%)	10.79	11.75	15.1	18.81
Surge margin under $D=0.11$ distortion (%)	10.59	10.87	12.72	14.68
Distortion causing surge margin loss (%)	0.2	0.88	2.38	4.13
Relative margin loss (%)	1.85	7.49	15.76	21.96

The distortion that the high pressure compressor bears is the surplus amount after low pressure compressor attenuation. According to the parallel compressor theory, the attenuation of distortion depends on a compressor without stall to additionally raise the supercharging ratio to a certain quantity. Distortion brings about a large surge margin loss. On the one hand, this confirms that this compressor is fairly sensitive to distortion; on the other hand, it also explains that it bears fairly large attenuated distortion load which causes the surplus distortion amount of its outlet to drop and alleviates the distortion load of the downstream components. Therefore, distortion of the low pressure compressor and high pressure compressor bring about the existing mutually compensatory relationship of surge margin

losses. Tests also show that in low pressure compressors the response to sensitive high rotational speed and high pressure compressor relative surge margin loss are minimal.

5. Influence of Distortion on 5P Compressor

When contrasted conditions are alike, the tendency of the responsive properties of the 5P compressor on distortion corresponds with that of the G02 and quantitative differences are not large. Figs. 9, 10, 14, 15 and Table 4 show this relationship.

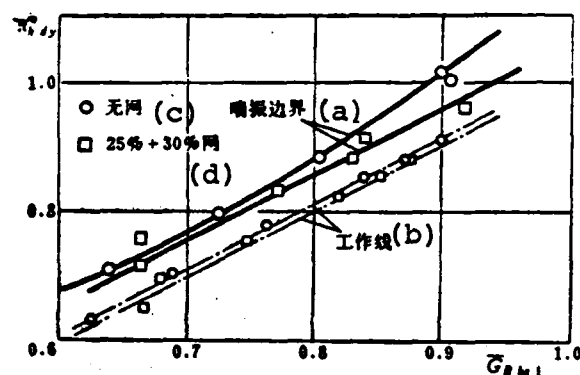


Fig. 14. Influence of distortion (5P) on L.P. compressor ($\bar{G}_{L.P.} \sim \pi_{L.P.}^2$)
Key: (a) Surge boundary; (b) Operating line; (c) No mesh; (d) Mesh.

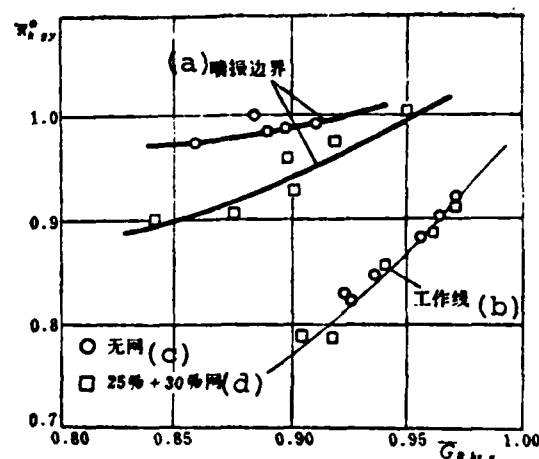


Fig. 15. Influence of distortion (5P) on H.P. compressor. ($\bar{G}_{H.P.} \sim \pi_{H.P.}^2$)
Key: (a) Surge boundary; (b) Operating line; (c) No mesh; (d) Mesh.

TABLE 4: 5P LOW PRESSURE COMPRESSOR

Conversion rotational speed (%)	95	90	85	80	75
Quasi-uniform flow field surge margin (%)	3.75	4.42	4.81	4.88	4.91
Surge margin under $\bar{D}=0.11$ distortion (%)		3.15	4.20	4.13	3.51
Distortion causing surge margin loss (%)		1.27	0.61	0.75	1.34
Relative margin loss (%)		28.73	12.68	15.37	27.29

5P HIGH PRESSURE COMPRESSOR

Conversion rotational speed (%)	96	94	92	90
Quasi-uniform flow field surge margin (%)	9.833	13.97	17.12	18.81
Surge margin under $\bar{D}=0.11$ distortion (%)	7.59	8.95	10.91	13.23
Distortion causing surge margin loss (%)	2.24	5.02	6.21	5.54
Relative margin loss (%)	22.8	35.93	36.27	29.45

The 5P and GO2 low pressure compressors are comparable. The quasi-uniform inlet surge margin is fairly low, the distortion surge boundary form is a curve, the operating line's drop amplitude following distortion is relatively large and therefore the surge margin loss is fairly small. Under distortion conditions, the two can actually use surge margin quantities to balance. The high pressure compressor then is opposite; the response of the 5 P on distortion is larger than that of the GO2.

When the engine of the two models is under distortion conditions, low pressure and high pressure compressor surge margin loss have a mutually compensatory effect. This reflects that the distortion's attenuation is actually obtained by depending on the compressor's surge margin loss and confirms the value of the

parallel compressor theory's qualitative analysis.

6. Comparison of Test Results of Components and the Whole Aircraft

Fig. 11 is the comparison of results of the GO2 low pressure compressor component test and the whole aircraft test. Under similar inlet conditions, the surge boundaries of the whole aircraft test are all higher than those of the component's test. Moreover, aside from quasi-uniform flow field, all distortion inlet conditions and the surge margin boundaries of the components test intersect with the operating lines measured from the whole aircraft. The larger the degree of distortion, the lower the intersecting rotational speed. If we use the surge margin boundaries of the component distortion test to evaluate the anti-distortion capabilities of the whole aircraft operation's low pressure compressor, we can naturally obtain the absurd theory that the engine cannot have stable operation.

In actuality, under the same distortion conditions as the above component's test, the engine underwent a multiple of various tests, enrolling tests on steady-state rotational speed properties, the thrust and pull of acceleration and deceleration and the fast speed convergent-divergent nozzle. The engine all along had operational stability. The differences of the two results show that we cannot use component tests of anti-distortion capabilities to evaluate the anti-distortion of the whole aircraft. The two have shared patterns of response to the distortion and they also have different characteristics. This also obtains verification in contrasting tests of other aircraft. Aside from this, the two blade effect results of the GO2 and 5P with different aspect ratios also reflect various differences in component tests and whole aircraft tests.

Analysis considers that the basic reason for variation of low

pressure compressor surge boundaries and anti-distortion capabilities in components and the engine lies in the compressor being a three-dimensional flow. The system conditions, interaction between components and the different surge process quasi-steady state and dynamic state differences all have influence. These factors are very complex; some change the degree of distortion attenuation and some regulate various levels of load causing above all weak links of stall by this level of rotation shifting to different levels, etc. Theoretical analysis can no doubt be carried out yet further tests and research are required for testing and verifying the theory.

IV. BRIEF CONCLUSION

(1) The fuel step is a good, useful forced surge method for bed tests of two-spool turbojet engines. The range of surge is fairly wide, excess temperature is brief and the retreat surge is dependable. Its weaknesses are surge velocity is quick, dynamic-state measurement precision is low and the amount of data processing work is large.

(2) The quasi-uniform flow field increases the engine nozzle area ratio. When the low pressure compressor operating line rises the high pressure compressor operating line drops. The drop quantity of the latter is greater than the increase quantity of the former.

(3) The quasi-uniform flow field GO2 model's low pressure compressor surge margin is in a conversion rotational speed between 95 and 75%, approximately between 10.06 and 6.62% and drops with the decline of the rotational speed. The high pressure compressor is in a conversion rotational speed between 96 and 90%, the surge margin increases from 10.8% to 18.8%, and it increases with the decline of the rotational speed. In the test range, the

high pressure compressor surge margin is higher than that of the low pressure compressor. The tendency of variation of the surge margin of low pressure and high pressure compressors coincides with the theory and similar foreign tests.

(4) When the engine conversion rate of airflow is 0.9, ground beds using the three 90° fan-shaped distortion wire meshes of 25%, (25+30)%, and (25-69)% can cause the distortion index to be $\bar{D}=0.068, 0.107, 0.166$; $DC90^\circ=-0.14, -0.244, -0.38$.

(5) Distortion causes the high pressure compressor's surge boundaries and operating line to drop, and the useable surge margin drops. When the degree of distortion enlarges, the surge boundary reduction is fairly large, the operating line reduction is fairly small, and the surge margin loss increases.

(6) When we install the two-blade engines of GO2 and 5P with quasi-uniform flow fields, the GO2 low pressure compressor surge boundaries are fairly high and the surge margin is slightly higher than 5P. The high pressure compressor is basically the same. With the same distortion conditions ($\bar{D}\approx 0.11$), in low pressure compressor surge margin loss, GO2 is larger than 5P. The high pressure compressor is opposite. The 5P surge margin loss is larger than that of the GO2 and is larger than the differences between the low pressor compressor.

(7) The surge boundary lines of low pressure compressor whole aircraft distortion tests are generally higher than distortion test values. The 5P and GO2 aspect ratio blade effect results are also different. This not only explains that the inlet distortion conditions influence the compressor surge boundary line and characteristic line, but also the interaction between the outlet conditions and system components, and the difference between the quasi-steady state and dynamic state of the inlet process also have marked influence. Therefore, the independent component test

properties cannot replace the matching component properties of the whole engine, and the component test results that are under specially designated conditions cannot be used to evaluate the performance and stability of the components in the whole aircraft system. This proves that whole aircraft distortion tests are completely necessary.

Those participating in this test were Liu Jicheng, Jiang Xunyi, Zhou Yuwen, Shi Yalin, Teng Shouzhen, and others.

References

- [1] "A Unified Theory on Air Inlet Channel/Engine Compatibility", AIAA Paper No. 72-115.
- [2] Engine Compression System Surge Line Evaluation Techniques, G. E. Paper, No. 76-015, 1976. Mu Nihei, Di San Ci Kong Qi Fa Dong Ji Guo Ji Tao Lun Hui. [The Third International Conference on the Air Engine].
- [3] Guo Wai Hang Kong. "Suspension Stall Problem of the F100 Engine". May 1979, [Foreign Aviation].
- [4] "The Influence of Intake Flow Distortion on Stall, Surge, and Acceleration Margin of the Intake Guide Blade Turbojet Engine with Installed Adjustable Compressor," NASA RMF 54K 26.
- [5] "Performance and Stall Boundaries of an Afterburning Turbojet Engine When There is No Inlet Flow Field Distortion," NASA TMX - 1947.

FUNDAMENTAL INVESTIGATION OF JET ENGINE IGNITION OF FUELD SPRAYS AND ITS APPLICATION

Chen Nengkun
Beijing Institute of Aeronautics and Astronautics

Abstract

Based on recent results of fundamental research work on jet engine ignition of fuel sprays, it is concluded that the present store energy in high energy ignition equipment should not be further increased. The effective approaches for improving ignition performance are to improve the quality of fuel sprays, to sustain optimal spark time, to keep the electric pole distance a little more than the quenching distance and to heat the starting fuel etc.

I. PREFACE

The problem of jet engine ignition under the condition of low ground temperatures and low pressure at high altitude has become especially serious. For a long time, research work done on the problem of electric spark ignition basically was divided into two categories: (1) on engine or combustion chamber component testers: this type of research was limited to only solving certain concrete problems. (2) Basic research of the ignition problem carried out on small model testers; the goal was to differentiate and clarify various influential factors. This possesses common guiding significance for the design of ignition systems [4-6] and has value for widespread applications. It also advances the development of the basic theory of electric spark ignition.

II. MODEL OF THE BASIC THEORY OF ELECTRIC SPARK IGNITION

How a structure causes an electric spark to be able to ignite combustible gas mixtures has been a major subject of

ignition research for a long time. People have proposed various theories on ignition through tests, analysis, and conjecture. The majority of these theories are based on this concept: if there generally is an instantaneous ignition source of an electric spark it must supply sufficient energy for a combustible gas mixture so that it produces a critical small volume of blazing air mass. It is able to satisfy the necessary conditions for flame dissemination; the velocity of the hot air mass producing a quantity of heat surpasses the velocity of the above-mentioned air mass losing a quantity of heat. This threshold energy is defined as the minimum ignition energy, and the dimension of this critical small volume is defined as the quenching distance, and less than this distance causes ignition failure due to the effects of ambient radiation.

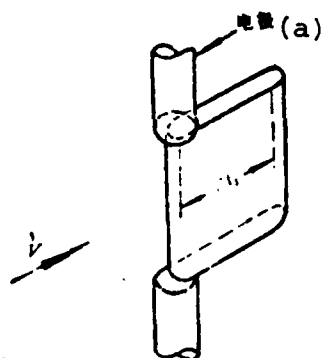


Fig. 1. Theoretical model formed by the spark core of a flowing combustible gas mixture.
Key: (a) Electrode.

Fig. 1 shows the theoretical model of the ignition of a flowing combustible gas mixture [11]. The route of the spark discharge established a high temperature hot air cylinder volume between the electrodes, the influence of the airflow makes this volume, and if the heat nucleus extends towards the downstream

direction, it becomes an oblate rectangular parallelepiped. Under good conditions, the growing heat rate of the chemical reaction on the nucleus surface (i.e., the flame peak) can surpass the losing heat rate of turbulent diffusion. Then the spark nucleus will continuously expand and cause ignition to be successful. Otherwise, the temperature in the nucleus will continuously decline until the reaction completely stops and ignition fails. Therefore, a similar crucial point is the critical dimensions. That is, in the time that the temperature of the nucleus drops to the temperature of the normal flame of the gas mixture, whether or not the spark nucleus has already grown to the above dimensions.

As to the theoretical model of the flowing air fuel spray ignition, the temperature within the nucleus on the one hand stems from the spark energy, and on the other hand stems from the heat energy released by minimum drip rapid vaporization. Later, because heat diffusion goes to a fresh gas mixture that has contact with the exterior of the nucleus and the droplets that remain from the vaporization in the nucleus, the temperature rapidly declines. The key factor of ignition is whether or not these droplets in the nucleus can rapidly vaporize and combust to produce an ample quantity of heat so that before the nucleus shrinks to its critical dimensions, it compensates for the heat loss.

III. A SYNOPSIS OF THE FUNDAMENTAL RESEARCH RESULTS

The laboratory research of ignition of kerosene sprays in flowing air is carried out in two steps: first under constant pressure and constant temperature, and next under low pressure, low temperature and low pressure, high temperature. Fig. 2 shows the test device that was used. The results of typical significance that were obtained under constant pressure and constant temperature are shown in Figs. 3-5.

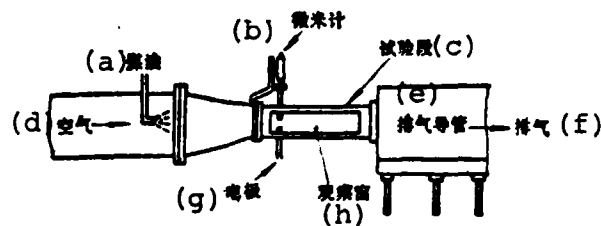


Fig. 2. Simplified diagram of test device.

Key: (a) Kerosene; (b) Micrometer; (c) Test section; (d) Air; (e) Exhaust pipe; (f) Exhaust pipe; (g) Electrode; (h) Observation window.

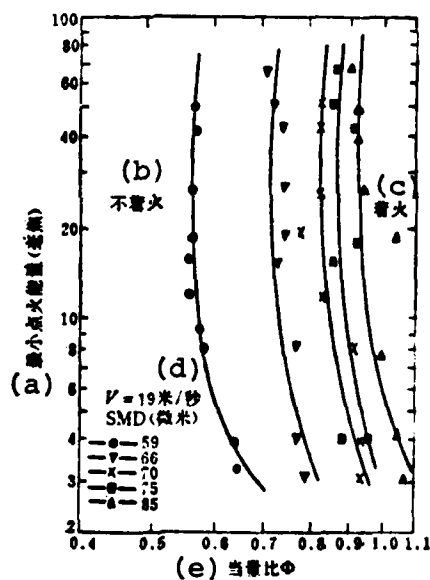


Fig. 3. Influence of spray quality on lean fuel ignition limit.

Key: (a) Minimum ignition energy (millijoules); (b) No ignition; (c) Ignition; (d) $V=19\text{m/second}$, SMD (micron); (e) Equivalent proportion ϕ .

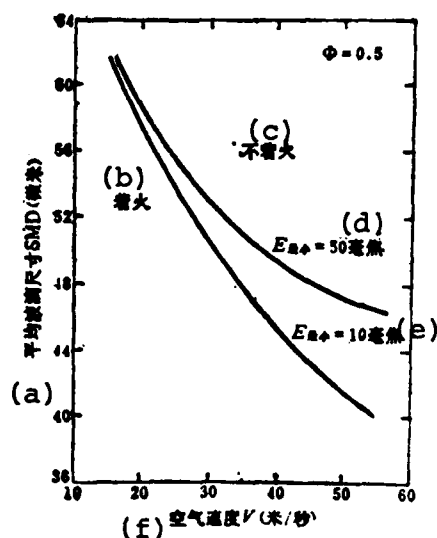


Fig. 4. Influence of flow velocity on ignition limit. Key: (a) Average droplet dimension SMD (microns); (b) Ignition; (c) No ignition; (d) $E_{\min} = 50$ millijoule; (e) $E_{\min} = 10$ millijoule; (f) Air velocity V (m/sec.).

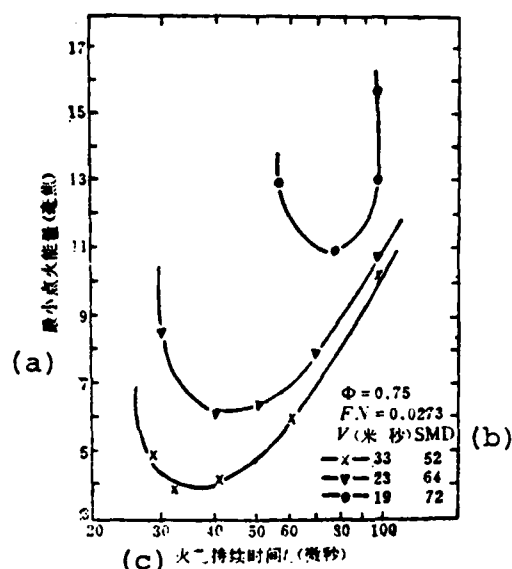


Fig. 5. Influence of flow velocity and spray quality on optimum spark duration. Key: (a) Minimum ignition energy (millijoules); (b) V (m/seconds) SMD; (c) Spark duration (microns).

Fig. 3 shows that when spray quality improves, the ignition limit of lean fuel reaches very great expansion, thus showing the strong influence of the spray quality on the performance of the ignition. When the spark energy is fairly large, increasing the spark energy already cannot attain any advantage. On the one hand, this is due to the very poor effectiveness of electric energy under high spark energy turning into thermal energy, and on the other hand, it is because expanding the lean fuel ignition limit then reduces the total fuel in the spark nucleus and the vaporization rate. At this time the most effective method for increasing the fuel vaporization rate to improve ignition is to raise the quality of the spray, but the advantage of reducing SMD (Sauter mean diameter) is not linear, and under a relatively small SMD it is even more noticeable.

Fig. 4 shows the unbeneficial influence of the flow velocity on the ignition limit. This aspect is because turbulent flow increases with the velocity causing the heat loss in the spark nucleus to increase. At the same time, it is also because under a comparatively high flow velocity, spark discharge heats an even larger amount of flowing fresh gas mixture. All of these cause the temperature in the spark nucleus to drop thus reducing the fuel evaporation rate and the chemical reaction rate in the nucleus. At the same time, only when SMD is less than 50 microns and the spark energy is also fairly small, can we then use the method of increasing the spark energy to improve ignition performance. Fig. 5 shows that not only is the total energy of the spark very important for ignition, but also the release speed of this energy is also very important. If the time is very short, then most of the energy is lost by shock wave form and if time duration is very long, then the spark energy is also not beneficial to ignition because it is added to the exceedingly large volume of gas mixture and reduces the temperature.

The results of typical significance that were obtained under low pressure, low temperature and low pressure, high temperature are shown in Figs. 6-9.

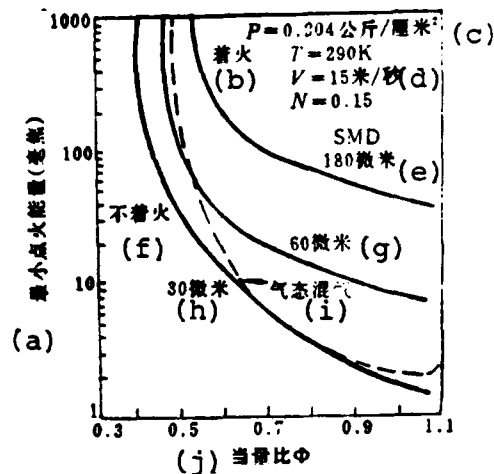


Fig. 6. Influence of spray quality and fuel-air ratio on minimum ignition energy. Key: (a) Minimum ignition energy (millijoules); (b) Ignition; (c) kg/cm^2 ; (d) m/seconds; (e) Micron; (f) No ignition; (g) Micron; (h) Micron; (i) Gaseous mixture; (j) Equivalent proportion Φ .

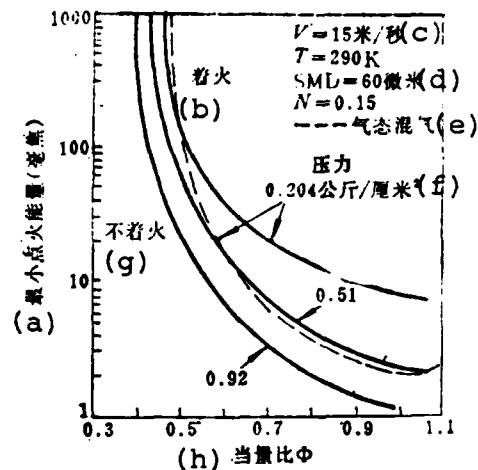


Fig. 7. Influence of air pressure and fuel-air ratio on minimum ignition energy. Key: (a) Minimum ignition energy (millijoules); (b) Ignition; (c) m/seconds; (d) Micron; (e) Gaseous mixture; (f) Pressure, kg/cm^2 ; (g) No ignition; (h) Equivalent proportion Φ .

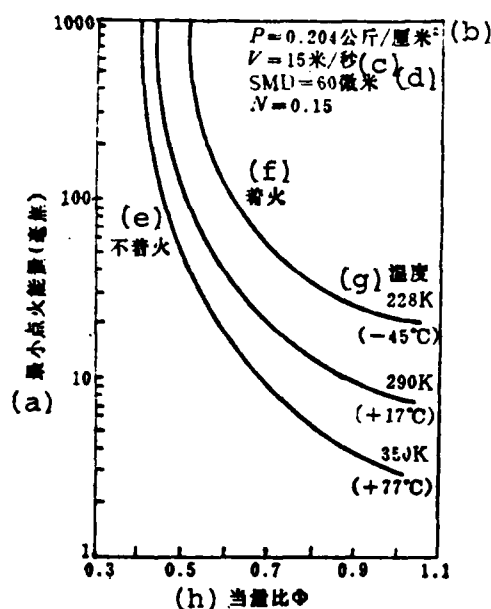


Fig. 8. Influence of air temperature and fuel-air ratio on minimum ignition energy.

Key: (a) Minimum ignition energy (millijoules); (b) kg/cm²; (c) m/seconds; (d) Micron; (e) No ignition; (f) Ignition; (g) Temperature; (h) Equivalent proportion Φ .

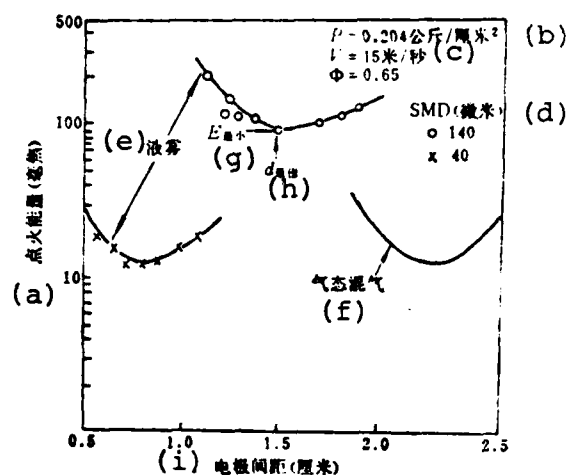


Fig. 9. Influence of spray quality on optimum electrode distance.

Key: (a) Ignition energy (millijoules); (b) kg/cm²; (c) (m/seconds; (d) Micron; (e) Liquid spray; (f) Gaseous mixture; (g) Minimum; (h) Optimum; (i) Electrode distance (cm).

IV. FUNDAMENTAL RESEARCH RESULTS AND PRACTICAL APPLICATION

Fundamental research results for the problem of the ignition of jet engine combustion chambers under atmospheric pressure, especially under low pressure, low temperature conditions of simulated engine high altitude re-ignition, possess general guiding significance and extensive application value.

1. Ignition Devise
- (1) Ignition Energy

From the related figures we can clearly see that under test conditions the largest minimum ignition energy is no more than 100 plus millijoules and in the region which cannot ignite, it is also of no use to add more energy. Especially when the spray quality is comparatively poor, this method of using increased energy cannot be effective for improving ignition. However, in the high energy ignition device that is now popularly used both domestically and abroad, the stored energy of the electric capacity is generally 12 joules. Some people [12] have carried out detailed experimental research on ignition energy loss and transformation conditions and discovered that the majority of the loss of the 12 joules of stored energy was lost on each electric element and conducting wire; only approximately 3 joules became spark energy (in which approximately 2 joules was lost because of shock wave and microwave radiation, and the remaining inadequate 1 joule was actually used for heating the combustible gas mixture). Yet, the spark energy of these 3 joules was already large enough for engine ignition; several ten times larger than the necessary 100 millijoules. The stored energy of the increased ignition device can cause various losses to unsuitably increase but as it is actually used to heat the energy of the gas mixture it increases very little. A more primary reason is that the cause of engine ignition failure is not inadequate energy but is various other factors. Therefore, the energy of the present high energy ignition device is already more than sufficient and we should not again pursue a high-powered ignition device, otherwise it will be very difficult to have any effectiveness. We can only increase the weight and volume of the ignition device and reduce the service life of the semiconductor electrotube. Conversely, we should research using other effective measures to reduce the stored energy of the present high energy ignition device under the prerequisite

of satisfying the engine's requirements for ignition performance.

(2) Spark Discharge Duration

In the range of test parameters that are near to actual engine conditions, we discovered the optimum spark duration to be approximately between 30 to 100 microseconds. The present high energy ignition device which was made in China must consider this problem. The actual measured results of some ignition devices are approximately 200 microseconds which is clearly too large and not advantageous for ignition.

(3) Electrode Distance and Form

We should ensure, under the most difficult ignition conditions (such as the high altitude windmill), that the electrode distance is slightly larger than its quenching distance. For the semiconductor electrotube, we should research its form and dimensions, and cause its effect on the quenching of the spark core to be reduced to a minimum.

(4) Ignition Frequency

The spark frequency of a general high energy ignition device is approximately 1~2 times/second. If we compute the spark duration at 100 microseconds, its time can reach to over ten thousand fold. We can see that the ignition frequency generally cannot have too great of an influence on the ignition process. But when the electrode distance is smaller than the quenching distance it can then be influential. This is because raising the frequency can cause the electrode temperature to rise, it reduces the effect of the electrode on the next quenching of the spark core and thus is beneficial for ignition. Yet, increasing frequency on a certain ignition device of stored energy

inevitably reduces spark energy, otherwise capacitance must be increased so that ignition device weight and volume increase.

2. Fuel Nozzle

Quality of spray has a strong influence on ignition performance. A slight reduction of the SMD (Sauter mean diameter) can then markedly improve ignition performance. To attain a very good spray, we only have the starting nozzle that uses a relatively small rate of flow number FN, and it requires a meticulously designed and machined nozzle. As to the direct ignition system, when engine ignition was started, the quality of the main nozzle spray was extremely poor, and thus it was very difficult to have a good ignition performance.

3. Ignitor Fuel-Air Ratio

Under each test condition, there existed the lean fuel ignition limit and the rich fuel ignition limit. Therefore, we should ensure that the ignitor has a suitable fuel-air ratio under various ignition conditions, including the overall fuel-air ratio and gaseous fuel-air ratio. Although general variations of fuel amount cannot be too large, the air amount, however, has very large variations following the aircraft windmill mode. Moreover, fuel temperature differences are very large due to various factors and these not only influence the overall fuel-air ratio but also influence the gaseous fuel-air ratio. Therefore, ensuring that the engine has suitable overall fuel-air ratio and gaseous fuel-air ratio under various complex conditions of applications is an important task of the ignition system design.

4. Ground Simulated High Altitude Ignition Tests

In the area of air flow, aside from simulating windmill mode combustion chamber intake pressure and velocity, we should as

fully as possible simulate low temperature. We should also correspondingly simulate the intake flow field because it also influences the fuel-air ratio. In the area of fuel, we must simulate starting gas fuel pressure and fuel temperature as well as main gas fuel pressure because the spray quality of the nozzle seriously influences ignition performance.

5. Rich Fuel Ignition Boundaries and Fuel Temperature

Lean fuel ignition boundaries only represent one part of ignition performance and to completely show ignition performance, we must also find the rich fuel ignition boundaries. What is regrettable is that all the workers on this fundamental research worry that rich fuel ignition tests will harm the safety of the equipment and so they discard this research. We must carry out detailed research on the influence of each primary parameter on rich fuel ignition boundaries. Increasing fuel temperature can markedly raise the fuel's saturation vapor pressure and also reduce the viscosity and improve the quality of the nozzle spray. All of these raise the fuel vaporization rate. The influence of fuel temperature that gives rise to variations of fuel viscosity, surface tension and saturation vapor pressure on the gaseous fuel-air ratio, and the influence of the relation between gaseous fuel-air ratio and overall fuel-air ratio on ignition performance, are important problems for future fundamental research on ignition.

V. THE DEVELOPMENT DIRECTION OF IGNITION SYSTEMS JUDGING FROM THE FUNDAMENTAL RESEARCH RESULTS

The future development of jet combustion chambers requires reducing pollution and utilizing replacement fuel. Therefore the nose sections of the flame tube will develop towards lean fuel which is pre-mixed, pre-evaporated and has comparatively high average flow speed. This will cause the ignition problem to

be even more serious. The development of increased high pressure ratio and high turbine front temperature cause the thermal load of the flame tube wall to become greater and greater and so it is necessary to strengthen the gaseous film cooling. This is a very unbeneficial factor for direct ignition. We can predict that the use of the present comparatively popular high energy ignition device's direct ignition system will, in the future, meet with very great difficulties and it will even be difficult to satisfy ignition requirements. However, from the fundamental research results, we can see that the high energy ignition device's torch ignition system possesses many strong points. First, we can design a starting nozzle with good spray quality and we can use fuel with good volatility to attain good spray. We can also utilize various modes to heat the starting fuel, raise the spray quality and increase the fuel vapor. Second, by using the torch ignitor it is comparatively easy to control the overall fuel-air ratio and the gaseous fuel-air ratio, and under the most difficult high altitude windmill ignition conditions it is easy to cause its proper coordination. Third, the torch ignitor can very well avoid the unbeneficial influence of air flow speed on ignition. Therefore, judging from satisfying the future requirements for high altitude ignition, the torch ignition system has many more advantages. Its primary weakness is that the structure and system are comparatively complex and it easily influences the air flow structure in the combustion chamber.

VI. CONCLUSION

Under atmospheric pressure and temperature that correspond to engine ground ignition starting conditions, and under low pressure and low temperature that correspond to high altitude windmill ignition starting conditions, fundamental research on kerosene spray ignition in flowing air has obtained a series of important results. Based on these fundamental research results,

the development and application of actual ignition systems are:

(1) The presently popular high energy ignition device of 12 joules stored energy is already sufficiently large. We should not again increase the stored energy.

(2) We must meticulously design and machine a starting fuel nozzle so as to attain the best spray. We should regularly check the quality of the spray of the starting nozzle for the engine in service.

(3) Optimum spark duration should be below 100 microseconds.

(4) Under the most difficult ignition conditions, the electrode distance should be slightly larger than its quenching distance and be concretely determined by the test.

(5) Heating the starting fuel is one effective measure for improving high altitude ignition performance.

(6) Under extensive ignition conditions, we should ensure that the area of the electrotube of the torch style ignitor or the direct ignition system has suitable overall fuel-air ratio and gaseous fuel-air ratio.

Furthermore, when carrying out ground simulated high altitude tests, aside from simulating combustion chamber intake pressure, velocity and flow field, it will be even better if we can simulate low pressure conditions of intake. We must conscientiously simulate starting fuel temperature and pressure as well as main fuel pressure.

References

- [1] Combustion, Flame and Explosion of Gases, second edition 1961, P. 323

References (continued)

- [2] Spark ignition of flowing gases. NACA Report 1287. 1956.
- [3] Investigation of several techniques for improving altitude-starting limits of turbojet engines. NACA RM E52103.
- [4] Ignition of kerosine fuel sprays in a flow air stream. Combustion Science and Technology 1973. Vol 8.
- [5] Ignition of Liquid Fuel Sprays at Subatmospheric Pressures. Combustion and Flame 31. P. 115(1978).
- [6] Minimum ignition energies in flowing kerosine-air mixtures. Combustion and Flame 27. P. 1(1976).
- [7] The influence of spark discharge characteristics on minimum ignition energy in flowing gases. Combustion and Flame 24. P. 99(1975).
- [8] Ignition and flame quenching in flowing gaseous mixtures. Proceedings of the Royal Society of London 357. P. 163(1977).
- [9] Spark ignition of turbulent flowing gases. AIAA 15th Aerospace sciences meeting 1977.
- [10] Evaporation characteristics of kerosine sprays injected into a flowing air stream. Combustion and Flame 26. P. 303(1976).
- [11] The influence of flow parameters on minimum ignition energy and quenching distance. Fifteenth Symposium on Combustion. P. 1473.
- [12] Влияние характеристик форсунок, температуры и физико-химических свойств топлива на пусковые качества камер сгорания ГТД. Авиационная Техника 1970 №2.

DEVELOPMENT OF AN ASTRO-INERTIAL HYBRID NAVIGATION SYSTEM AND A STAR TRACKER

Shen Gongxun, Qin Shiguang, Chang Qingzhi and Zhou Danian
Beijing Institute of Aeronautics and Astronautics

Abstract

Simple inertial or Doppler navigation has a common shortcoming that position errors are always increasing with time or distance and therefore an external reference system is required. In order to meet the needs of high accuracy and reliability for modern vehicle navigation, the development of modern navigation systems shows a tendency to hybrid navigation. This paper presents an astro-inertial hybrid navigation system which is physically more rational and accurate and has come into particular use in various modern flight vehicles. In astronavigation, a star tracker is an essential facility to obtain the measurement information of this hybrid system. This paper summarized the research and design methods of China's first domestically designed automatic star tracker and the measures taken to solve the principal technical key problems. It also presents related formulae. Experimental results have proved that the design is reasonable and has attained the expected performance indices according to which the designed star tracker on the ground is capable of tracking stars with brightness above second class at night and the brightest stars under the background of certain brightness in daytime.

I. FOREWORD

So-called hybrid navigation is simply a navigation system with many kinds of navigation means being comprehensively utilized or composing the best operations through systematic control and data processing methods. It generally takes the inertial navigation system as the primary means of navigation, uses other

auxiliary navigation equipment to provide external measurement information, and utilizes a Kalman filter method to process measurement data. In order to provide the best estimate of the inertial guidance system, later we will estimate the condition of the inertial guidance system according to the best control methods and add them to the inertial guidance system, thereby raising the precision of the inertial guidance system.

The importance of the astro-inertial navigation system lies in the astro system not having the increase and accumulation of errors with time and distance. Due to the accuracy of the celestial body position, the astro system can obtain a comparatively high degree of accuracy. Further, due to the inability of interference of the celestial body target, astronavigation has important significance in military affairs. In the combination of astronomy and inertia, the former can carry out correction of inertial errors and as a result the requirements for the inertial systems and components can be relaxed. Also, the high cost of the inertial guidance system and components then declines. Due to these advantages, as some particular strategic and tactical required weapon systems such as warning reconnaissance, bombing and antisubmarine high altitude and long range aircraft as well as mobile launched guided missiles and satellite space shuttle spacecraft, guided missile measurement ships, nuclear submarines, etc., this hybrid system obtains comparatively extensive applications.

II. THE ASTRO-INERTIAL HYBRID NAVIGATION SYSTEM [1,2]

The inertial guidance system referred to in this paper is a semi-analytical system that is based on the directions of the northeastern space geographic coordinate system. For analysis we draw three groups of coordinate systems: OXYZ is the geographic coordinate; $Ox_p y_p z_p$ is the platform coordinate system; $Ox_c y_c z_c$

is the computer coordinate system. In theory, these three groups of coordinate systems should coincide but in reality they possess small vector error angles between each other.

It is assumed that $\bar{\psi}$ is the vector angle between the platform coordinate system and the computer coordinate system;

$\delta\bar{\theta}$ is the vector angle between the computer coordinate system and the geographical coordinate system;

$\bar{\varphi}$ is the vector angle between the geographical coordinate system and the platform coordinate system.

From the above definitions we obtain $\bar{\varphi} = \bar{\psi} + \delta\bar{\theta}$

The definitions for the angular velocities of the three groups of coordinate systems are as follows:

$\bar{\omega}_p$ is the angular velocity of the platform coordinate system corresponding to inertial space;

$\bar{\omega}_c$ is the angular velocity of the computer coordinate system corresponding to inertial space;

$\bar{\omega}$ is the angular velocity of the geographic coordinate system corresponding to inertial space.

To make the platform track the geographic coordinate system, the computer output information ω_c renders a gyro so that the platform revolves around the axial rotation of the computer coordinate system and thereby causes the platform inertial space to use ω_c angular velocity rotation. However, the output information ω_c given to the gyro in reality makes the platform rotate around the platform coordinate system and thus the platform in inertial space does not use ω_c angular velocity rotation. The angular velocity direction of the platform's actual rotation has already been rotated passed the ψ angle from the ω_c direction as shown in Fig. 1.

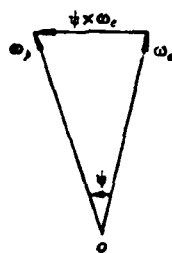


Fig. 1.
Relationship
between ang-
ular veloc-
ities ω_p
and ω_c .

From the analysis of inertial guidance system errors we can obtain the formula:

The platform coordinate system expressed in formula (1) corresponds to the vector angle in the computer coordinate system. It is called the platform drift angle ψ equation and is an extremely important equation in the analysis of inertial guidance system errors. It directly established the connection between platform drift angle ψ and gyro drift rate ϵ .

We assume that the mathematical model of the gyro's random drift rate is a first order Markov equation where the mean value is zero. It possesses the index law auto-correlation function $R(\tau) = \sigma^2 e^{-\beta|\tau|}$, σ^2 is the variance of the gyro drift velocity and β is the inverse correlation time constant of the gyro drift velocity which satisfy the forming filter equation of the gyro drift model as shown in Fig. 2.

In Fig. 2, f is the zero mean value, the auto-correlation

function is the white noise of $2\beta\sigma^2\delta(\tau)$ and $\delta(\tau)$ is a unit pulse function. The figure indicates that we use f to drive a simple lag network, the output of the network is ϵ_r . It combines with the constant value gyro drift ϵ_c to form gyro random drive function ϵ which also views the highly related colored noise ϵ_r as the output of the linear system driven by white noise f .

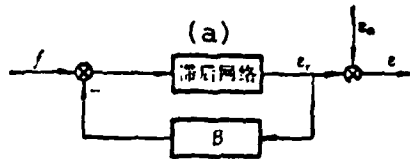


Fig. 2. Gyro drift model.
Key: (a) Lag network.

Assuming $\epsilon_{rx}, \epsilon_{ry}, \epsilon_{rz}$ are the platform random sectional drift rates on the three directions of northeast space, $\epsilon_{cx}, \epsilon_{cy}, \epsilon_{cz}$ are the constant value sectional drift rates on the three directions of northeast space.

Thus we have:

$$\left. \begin{aligned} \dot{\epsilon}_{rx} &= -\beta_x \epsilon_{rx} + f_x \\ \dot{\epsilon}_{ry} &= -\beta_y \epsilon_{ry} + f_y \\ \dot{\epsilon}_{rz} &= -\beta_z \epsilon_{rz} + f_z \\ \dot{\epsilon}_{cx} &= 0 \\ \dot{\epsilon}_{cy} &= 0 \\ \dot{\epsilon}_{cz} &= 0 \end{aligned} \right\} \quad (3)$$

The equation for inertial guidance systems errors is:

$$\begin{bmatrix} \dot{\psi}_x \\ \dot{\psi}_y \\ \dot{\psi}_z \end{bmatrix} = \begin{bmatrix} 0 & \Omega \sin \varphi + \frac{V_x}{R} \operatorname{tg} \varphi & -\Omega \cos \varphi - \frac{V_z}{R} \\ -\Omega \sin \varphi - \frac{V_x}{R} \operatorname{tg} \varphi & 0 & -\frac{V_y}{R} \\ \Omega \cos \varphi + \frac{V_z}{R} & \frac{V_y}{R} & 0 \end{bmatrix} \begin{bmatrix} \psi_x \\ \psi_y \\ \psi_z \end{bmatrix} + \begin{bmatrix} \varepsilon_x \\ \varepsilon_y \\ \varepsilon_z \end{bmatrix} \quad (1)$$

In the equation, Ω is the angular velocity of the rotation of the rotation of the earth, V is the velocity vector: R is the average radius of the earth.

Taking the vector angle between the inertial guidance system's platform coordinate system and computer coordinate system, and the gyro random sectional drift rate and constant value sectional drift rate as the state variable:

$$X = (\psi_x, \psi_y, \psi_z, \varepsilon_{xx}, \varepsilon_{yy}, \varepsilon_{zz}, \varepsilon_{yx}, \varepsilon_{xy}, \varepsilon_{zx}) \quad (5)$$

From this, we establish the equation of state as:

$$\dot{X} = A(t)X(t) + Gf(t) \quad (6)$$

In the equation:

$$A(t) = \begin{array}{c|c} \begin{array}{ccc} 0 & \Omega \sin \varphi + \frac{V_x}{R} \operatorname{tg} \varphi & -\Omega \cos \varphi - \frac{V_z}{R} \\ -\Omega \sin \varphi - \frac{V_x}{R} \operatorname{tg} \varphi & 0 & -\frac{V_z}{R} \\ \Omega \cos \varphi + \frac{V_x}{R} & \frac{V_y}{R} & 0 \end{array} & \begin{array}{c} 0_{3 \times 6} \\ \\ \\ \\ \\ \\ \end{array} \\ \hline \begin{array}{c} 0_{3 \times 6} \\ \\ \\ \\ \\ \\ \end{array} & \begin{array}{c} -\beta_x \quad 0 \quad 0 \quad 0 \quad 0 \quad 0 \\ 0 \quad -\beta_y \quad 0 \quad 0 \quad 0 \quad 0 \\ 0 \quad 0 \quad -\beta_z \quad 0 \quad 0 \quad 0 \\ 0 \quad 0 \quad 0 \quad 0 \quad 0 \quad 0 \\ 0 \quad 0 \quad 0 \quad 0 \quad 0 \quad 0 \\ 0 \quad 0 \quad 0 \quad 0 \quad 0 \quad 0 \end{array} \end{array} \quad (7)$$

$$G = \begin{bmatrix} 0_{1 \times 3} \\ I_{3 \times 3} \\ 0_{3 \times 3} \end{bmatrix} \quad (8)$$

With dispersement of equation (6) we obtain:

$$X_k = \phi_{k,k-1} X_{k-1} + W_{k-1} \quad (9)$$

In the formula, $\phi_{k,k-1}$ is the conditional rotation matrix; dynamic-state noise W_{k-1} is the independent noise arrangement that has a mean value of zero. Its common variance is:

$$E(W_k W_k^T) = Q_k \delta_{kj} \quad (10)$$

In the equation, Q_k is the non-negative defined matrix and δ_{kj} is the Kronecker δ function:

$$\delta_{kj} = \begin{cases} 1 & k = j \\ 0 & k \neq j \end{cases}$$

Considering the control effect of hybrid navigation, adding in control sum $\Gamma_{k,k-1} v_{k-1}$, therefore the effect equation of

state of the closed cycle system is:

$$x_k = \Phi_{k,k-1} x_{k-1} + \Gamma_{k,k-1} u_{k-1} + w_{k-1} \quad (11)$$

2. Measurement Equation

The external measuring information of the hybrid navigation system is given by the astronavigational star tracker. If the star tracker is installed on the inertial guidance platform, when the star aims, the star tracker can measure the three projected weights $L \cosh_p \sin A_p$, $L \cosh_p \cos A_p$ and $L \sinh_p$ of the corresponding platform coordinate system. In the equation, h_p is the star altitude angle, A_p is the star azimuthal angle and L is the aiming line length. The three projected weights of the stars in the computer coordinate system are $L \cosh_c \sin A_c$, $L \cosh_c \cos A_c$ and $L \sinh_c$, and from the coordinate transformation we can obtain:

$$\begin{bmatrix} L \cosh_p \sin A_p \\ L \cosh_p \cos A_p \\ L \sinh_p \end{bmatrix} = \begin{bmatrix} 1 & \psi_x & -\psi_y \\ -\psi_x & 1 & \psi_z \\ \psi_y & -\psi_z & 1 \end{bmatrix} \begin{bmatrix} L \cosh_c \sin A_c \\ L \cosh_c \cos A_c \\ L \sinh_c \end{bmatrix} \quad (12)$$

In the equation:

$$\begin{bmatrix} 1 & \psi_x & -\psi_y \\ -\psi_x & 1 & \psi_z \\ \psi_y & -\psi_z & 1 \end{bmatrix} \text{ is the coordinates transformed matrix of the computer coordinate system to the platform coordinate system.}$$

Letting $\Delta h = h_p - h_c$ after reduction operations we can obtain:

$$\Delta A = A_p - A_c$$

$$\begin{bmatrix} \Delta h \\ \Delta A \end{bmatrix} = \begin{bmatrix} -\operatorname{tg} h_c \sin A_c & -\operatorname{tg} h_c \cos A_c & 1 \\ -\cos A_c & \sin A_c & 0 \end{bmatrix} \begin{bmatrix} \psi_x \\ \psi_y \\ \psi_z \end{bmatrix} \quad (13)$$

Letting:

$$Y = \begin{bmatrix} \Delta h \\ \Delta A \end{bmatrix} \quad H = \begin{bmatrix} -\operatorname{tg} h_c \sin A_c & -\operatorname{tg} h_c \cos A_c & 1 \\ -\cos A_c & \sin A_c & 0 \end{bmatrix} \quad 0_{1 \times 3}$$

Therefore:

$$Y_k = H_k X_k + V_k \quad (14)$$

In the equation, V_k is the measured noise of the star tracker which is the independent white noise arrangement with a zero mean value. Its common variance is:

$$E(V_k V_j^T) = R_k \delta_{kj} \quad (15)$$

In the equation, R_k is a positive defined matrix,

$$\delta_{kj} = \begin{cases} 1 & k = j \\ 0 & k \neq j \end{cases}$$

From the equation (13) we can see that angles Δh , ΔA , and Ψ that the astronavigational star tracker measurements obtained are related, and angle Ψ also directly established the connection between the platform drift angle and gyro drift rate. Therefore, angle values Δh and ΔA that were obtained by the astronavigation star tracker measurements can reflect the gyro's drift rate. This is most directly perceived in the physical sense. If we use the Kalman filter method to process this measurement data, to provide the most advantageous estimate for the conditions of the inertial guidance system, we carry out compensation, thereby raising inertial guidance precision. Therefore, we can say that the astro-inertial hybrid navigational system, in the physical sense, is a fairly reasonable and comparatively accurate navigational hybrid method.

3. Optimal Correction

To obtain the optimal correction, we should make the estimated value of the inertial guidance system always equal to zero, which is $\hat{X}_{k/k-1} = 0$. For this reason we select control matrix $T_{k,k-1} = \phi_{k,k-1}$, and control input $U_{k-1} = -X_{k-1/k-1}$. At this time,

the filter's estimated value is $\hat{X}_{k/k} = K_k Y_k$, and therefore the Kalman filter equation under the optimal correction is:

$$\left. \begin{aligned} \hat{X}_{k/k} &= K_k Y_k \\ P_{k/k-1} &= \Phi_{k,k-1} P_{k-1/k-1} \Phi_{k,k-1}^T + Q_{k-1} \\ K_k &= P_{k/k-1} H_k^T (H_k P_{k/k-1} H_k^T + R_k)^{-1} \\ P_{k/k} &= (I - K_k H_k) P_{k/k-1} \end{aligned} \right\} \quad (16)$$

After being given the initial values \hat{X}_0 , P_0 and Q_0 and then each time given the observed value Y_k we can find the optimal estimate $\hat{X}_{k/k}$ of the K moment. From this, we can determine the optimal estimate $\hat{X}_{k/k}$ of the K moment and then determine the controlling weight U_k of the K moment so as to realize the optimal correction for the inertial guidance system.

III. DESIGN OF THE STAR TRACKER

The star tracker is the primary component of the astronavigation system. It is also an important facility that can measure the angle of a celestial body which is used to compensate for the gyro drift rate. It can search, lock-on and track stars or other celestial body targets on a sky background. It accumulates light energy from these celestial targets and by differentiating star energy in the background and measuring the aiming line of the tracker in the aircraft (or submarine) coordinate system it corresponds to a device of the coordinate angle.

The star tracker is composed of several primary parts such as the optical system, signal scanning modulation system, radiation detector, and automatic identification and control system. It is shown in Fig. 3.

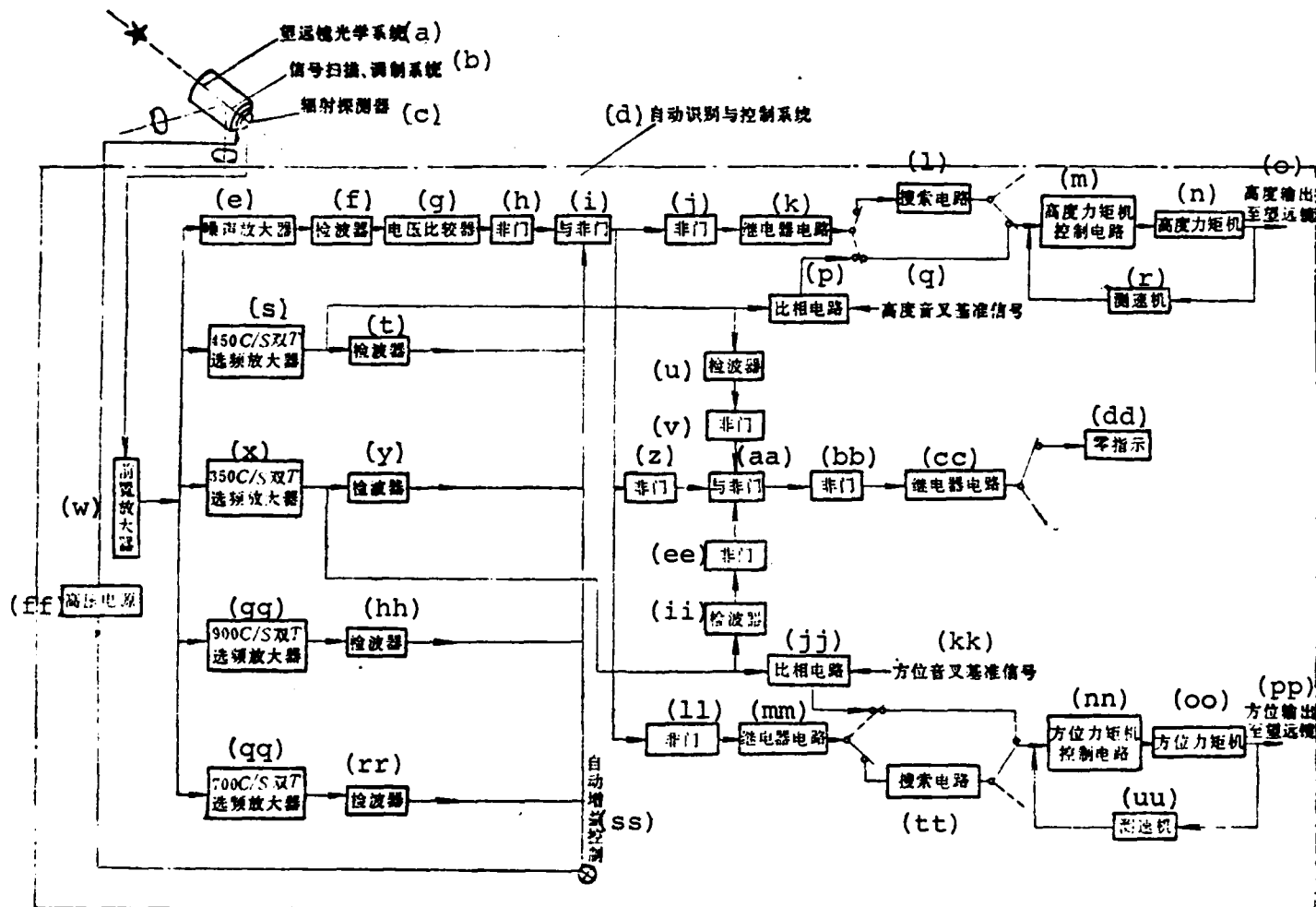


Fig. 3. Key: (a) Telescope optical system; (b) Signal scanning and modulation system; (c) Radiation detector; (d) Automatic identification and control system; (e) Noise amplifier; (f) Detector; (g) Voltage comparator; (h) NOT gate; (i) AND NOT gate; (j) NOT gate; (k) Relay circuit; (l) Searching circuit; (m) Altitude moment of force engine control circuit; (n) Altitude moment of force engine; (o) Altitude output to telescope; (p) Comparison circuit; (q) Altitude tuning fork reference signal; (r) Speed finding machine; (s) 450 C/S dual T selective frequency amplifier; (t) Detector; (u) Detector; (v) NOT gate; (w) Prime amplifier; (x) 350 C/S dual T selective frequency amplifier; (y) Detector; (z) NOT gate; (aa) AND NOT gate; (bb) NOT gate; (cc) Relay circuit; (dd) Zero indication; (ee) NOT gate; (ff) High voltage source; (gg) 900 C/S dual T selective frequency amplifier; (hh) Detector; (ii) Detector; (jj) Comparison circuit; (kk) Bearing tuning fork reference signal; (ll) NOT gate; (mm) Relay circuit; (nn) Bearing moment of force engine control circuit; (oo) Bearing moment of force motor; (pp) Bearing output to telescope; (qq) 700 C/S dual T selective frequency amplifier; (rr) Detector; (ss) Automatic

Fig. 3 (continued)

gain control; (tt) Searching circuit; (uu) Speed finding machine.

The parallel light coming from the celestial body acts as the optical system's input. The optical system accumulates this light energy and later through the signal scanning modulation system again transmits it to the radiation detector. The detector will transmit the signal to an automatic identification and control system so as to determine the tracker position in the search or track state.

The primary technical key of the star tracker lies in measuring an extremely low radiation level coming from a star in a sky background with a very high light intensity. For a zero (visual) grade ($m_v=0$) star, outside the earth's atmosphere its luminous flux density I_0 is only 2.1×10^{-10} lumen/cm², but the light energy of the daytime sky background frequently is several magnitudes higher than the star. In light of this, we must obtain the optimal performance through comprehensive consideration of determination of the optical system's structural parameters, signal scanner and modulation technology, selection and comparison of the detector, design of the circuit of the automatic identification and control system, etc.

This paper will discuss the above primary technical key problems in star tracker design.

1. Determination of the Structural Parameters of the Optical System

In the design of the star tracker's optical system, the determination of the structural parameters should take the signal-noise ratio criteria [7] as the basis:

$$S/N = \frac{1.59 \times 10^8 H \sqrt{Q \lambda A}}{\sqrt{B M a^4}} \quad (17)$$

In the equation, star radiation $H=5.18 \times 10^{-16} t_{e10}^{-0.4m}$
 $\int_0^\infty \left(\frac{H_\lambda}{H_{\lambda_{max}}} \right) \sigma(\lambda) d\lambda$ watts/cm²; in this expression, m is the bolometric magnitude and to transform into visual magnitude it is necessary to correct the heating radiation; t_e is the effective star temperature K°; $\int_0^\infty \left(\frac{H_\lambda}{H_{\lambda_{max}}} \right) \sigma(\lambda) d\lambda$ is the integral of the product of star light spectrum response rate $H_\lambda / H_{\lambda_{max}}$ and detector light spectrum response rate $\sigma(\lambda)$;

Effective background radiation $M=0.511 \times 10^{-8} B_s \int_0^\infty \left(\frac{M_\lambda}{M_{\lambda_{max}}} \right) \sigma(\lambda) d\lambda$
watts/cm²·degree^e;

B_s is the daylight sky brightness;

$\int_0^\infty \left(\frac{M_\lambda}{M_{\lambda_{max}}} \right) \sigma(\lambda) d\lambda$ is the integral of the product of background light spectrum response rate $M_\lambda / M_{\lambda_{max}}$ and detector light spectrum response rate $\sigma(\lambda)$;

Q is the quantum efficiency of the detector;

λ is the wavelength;

A is the effective area of the telescope's incident aperture;

B is the band width;

α is the telescope's field of vision.

Formula (17) shows: to increase the signal-noise ratio we must increase the square root of the effective area of the telescope's incident aperture, which is also the aperture of the telescope; raise the detector's quantum efficiency Q; and reduce field of vision α and band width B. Because the structural limits of the telescope's aperture in the design can possibly create constraint conditions, therefore the detector's width B, field of vision α , and selected high quantum efficiency Q are often variable design parameters. Moreover, we must carry out comprehensive consideration in each area when designing.

2. Signal Scanning and Modulation Technique

The signal scanning and modulation system of the star tracker are used for scanning, identification of star positions, modulating information and eliminating the interferences of the natural background. Here we use what is called a tuning fork signal scanning control system.

Operational Principles: The two tuning forks that are installed in the two directions X and Y compose the scanning control system. Each tuning fork is on an arm driving a thin metal strip with long holes and narrow cracks. The tuning forks are regarded as the self-oscillator of the transistor circuit. Star light passes through two parallel small holes with criss-crosses. These two small holes are installed close to each other on a certain side of the telescope's focal plane, and the small holes cross and form square holes. When the porous plates vibrate it then describes the Li Shayu pattern. In this way, the square region of holes that is swept by the instantaneous scanning then constructs the motion field of vision of the star tracker. Each scan takes the velocity that is determined by the fixed frequency of the tuning forks as a free oscillating vibrator for motion.

Theoretical Analysis: (1) The luminous flux ϕ that is accumulated by the star modulates the light that is discharged on the first scanner.

$$\phi(x, t) = \phi[f_0(x) + f_1(x)\sin\omega_1 t + f_2(x)\cos 2\omega_1 t + \dots] \quad (18)$$

(2) When the light beam goes through the installed second scanner with the first scanner becoming a right angle it forms the function of light intensity as time and coordinates X and Y:

$$\begin{aligned} \phi(x, y, t) = & \phi(f_0(x)f_0(y) + f_0(y)f_1(x)\sin\omega_x t + f_0(y)f_2(x)\cos 2\omega_x t \\ & + f_0(x)f_1(y)\sin\omega_y t + f_0(x)f_2(y)\cos 2\omega_y t + \text{和与差项}) \quad (19) \end{aligned}$$

Key: (1) Sums with differences.

Each sum on the right side of formula (19) contains the desirable position and the identified information. The first sum in the brackets is the average flux, the second sum is the X axial position signal, X the third is the X axial identification signal, X the fourth is the Y axial position signal, X the fifth is the Y axial identified information X and the remainder are sums with differences. Selective scanning frequencies ω_x and ω_y are not mutually whole multiples and to ensure that the sums with differences transcend the pass band of the tracking amplifier, in this kind of circuit there is then no cross coupling.

To eliminate cross coupling, the program selected $\omega_x = 350$ cycles/second, and $\omega_y = 450$ cycles/second. The structural parameters of the tuning fork blades are: narrow crack width $B = 0.1\text{mm}$, length $L = 1\text{mm}$, oscillation amplitude $A = 0.7\text{mm}$, the two tuning fork blade narrow crack distance $H = 0.2\text{mm}$.

The merits of this scanning control system are:

(1) Because we eliminated the electrical machinery and gear transmission that is generally needed for the modulation disk, therefore it possesses low power depletion, high life and high dependability. It is suitable for application in aeronautical and astronautical technology.

(2) The frequency stability degree is high.

(3) The effect of eliminating non-uniform background is advantageous to the general modulation disk.

3. Selection and Comparison of the Detector

The star tracker that is applied in earth and space navigations uses a typical detector that is primarily of two types; the photoelectric multiplier and photoconductor camera.

The selection and comparison of the detector also use a signal-noise ratio criteria [6] as data. The signal-noise ratio of the photoelectric multiplier is the ratio of the positive pole signal current and positive pole noise current. The signal current eliminated from the noise current of photoelectric conductor target surface is the signal-noise ratio of the photoconductor camera.

The formula for the signal-noise ratio of the photoelectric multiplier is:

$$S/N = \frac{\epsilon K_1 f_s S (1 - e^{-\delta/RC})}{\sqrt{2q(I_s + \epsilon K_1 I_a S)(f_s - f_n) \left(1 + \frac{1}{G}\right)}} \quad (20)$$

The formula for the signal-noise ratio of the photoconductor camera is:

$$S/N = \frac{\epsilon K_1 f_s S M (1 - e^{-\delta/RC}) r_s}{\sqrt{2q(I_s + \epsilon K_1 I_a S M)(f_s - f_n)}} \quad (21)$$

In the formula:

- ϵ is the optical transmission coefficient;
- K_1 is the ratio of the sensitivity of the detector and the sensitivity of the radiation on 2870° K color temperature under conditions of incident radiation of star color temperature;
- f_s is the signal flux of the optical system incident photo pupil (lumen);
- S is the photosensitive surface sensitivity of radiation on 2870° K color temperature (amps/lumen);
- $1 - e^{-\delta/RC}$ is the amplitude transformation properties of the electron signal amplifier with a time constant of RC and signal pulse with a duration of δ ;

G	is the gain of each level in the photoelectric multiplier;
$1 + \frac{1}{G}$	is the added noise due to the photoelectric multiplier;
q	is the electron charge (coulombs);
I_d	is the dark current of the photoelectric negative pole (amps);
K_2	is the ratio of detector sensitivity and radiation sensitivity on 2870° K color temperature under conditions of incident radiation that uses background color temperature;
I	is the illuminance due to background radiation on the optical system's focal plane (inch·candlepower);
a	is the area of the scanning hole (inch ²);
$f_2 - f_1$	is the band width of the detection system (cycles/second);
M	is the sensitivity gain caused by the storage; its value is equal to unit number scanned on the grating;
r_a	is the amplitude response coefficient of the small electron charge on the photosensitive surface caused by the electron beam on the small light image;
A	is the area of the photoelectric conductor target surface (inch ²).

Under conditions of daytime operation to select the the photoelectric detector we primarily considered three parameters:

- (1) The sensitivity of the photosensitive surface that forma a direct ratio with the quantum efficiency;
- (2) Storage gain;
- (3) Band width of the detection system.

If we use the photoelectric multiplier, because relatively speaking the photo negative pole sensitivity of this type is always comparatively low, they do not possess storage gain properties. Therefore, from its signal-noise ratio in the formula (20), we know that in daylight operations to be able to have a suitable signal-noise ratio, the band width of the detection

system must be small and therefore the search velocity of examining a star will be slow. Because the reciprocal of the band width represents the time of examining the star, it expresses that the telescope must use a small time length from the star accumulated energy to maintain the signal-noise ratio. Inspection time t divided by field of vision a is called the "inspection velocity" $W=a/t=aB$, expressing that the star tracker can revolve past stars and not lose the signal power velocity. Therefore, we should use the star tracker of the photoelectric multiplier and generally must utilize gyros or inertial platforms to make the aim line of the telescope obtain high precision stability. The sensitivity of the photosensitive surface of the photoconductor camera is extremely high and moreover it possesses storage gain properties. From signal-noise ratio formula (21) of the photoconductor camera we know that by utilizing a wide frequency band system, we can also use a fast speed search and can very quickly lock-on the star.

Under conditions of nighttime operations, in selecting the photoelectric detector we primarily consider three parameters:

- (1) Sensitivity of the photosensitive surface;
- (2) Signal gains that are obtained by storage or photoelectric multiplication;
- (3) Dark current.

The photoelectric multiplier has comparatively low dark current value and high photoelectric multiplier gains. Nighttime application performance is relatively good. Although the photoconductor camera possesses five to ten times more photosensitive surface sensitivity than the photoelectric multiplier, it only obtains gain from storage. It does not possess photoelectric multiplication properties and the dark current level is also extremely high. Thus, in the area of nighttime performance, the photoconductor camera is not as good as the photo-

electric multiplier.

Based on the above analysis of detector performance, as to the star tracker that is used at high altitude in the daytime when we take nighttime tracking of stars as primary, the selection of the photoelectric multiplier for the detector is comparatively suitable. We used the GDB-23 model photoelectric multiplier that was made in China. It has S-20 light spectrum response properties and approximately 23% peak quantum effectiveness, dark current equivalent input luminous flux is 5×10^{-11} lumens, negative pole integral sensitivity is 100 microamps/lumen and positive pole sensitivity is 100 amp/lumen (the operating voltage is 1140 volts, dark current is 40 nanoamps) which basically satisfies the design requirements.

4. Design of Automatic Identification and Control System Circuit

Requirements:

(1) On a given directional, the automatic search circuit can be carried out according to a certain program in searching a field of vision. When there are no stars in the field of vision, the system is positioned in the automatic search state.

(2) When stars appear in the field of vision, the system can automatically transform from the searching state to the tracking state.

(3) When the target star in the field of vision reaches zero potential, the system should have zero potential indication.

(4) When the moon, sun, clouds and bright or weak stars outside of the required magnitude appear in the field of vision, the automatic identification system can cause the system to continue to be positioned in the searching state.

5) When different magnitudes appear within the range of the tracking requirements, to maintain system tracking stability, the system should have an automatic gain control circuit.

The automatic identification and control system circuit program is shown in Fig. 3;

(1) In the searching field of vision, to be able to carry out searching for target stars, according to a certain program, the program uses the transistor self multivibrator as the cyclic pulse signal generator to control the altitude of the optical telescope and the rotation of the bearing torque electrical machinery. Here we utilize the self multivibrator wherein on the bearing is long cycle $T_1=23$ seconds and the altitude is short cycle $T_2=1.5$ seconds to form a searching field of vision with an altitude bearing of 1 radian x 1 radian.

(2) The radiation from the star can go through the photo-electric multiplier after going through the tuning fork scanning modulator, transforms into telegraphic signal output, and again goes through the prime amplifier where it is divided into five channel outputs. When there are no stars in the field of vision or weak stars outside the range of requirement, its output, after detection, is the direct flow weight below the threshold voltage value of the voltage comparator and in the channels of $\omega_x, \omega_y, 2\omega_x, 2\omega_y$, at this time there are no signal outputs. Going through the logical circuit of the star identification detector, output is at a high power level and the relay causes the system to be positioned in the automatic searching state.

(3) When the magnitudes that are within the required range appear in the field of vision, the output value is still below the value of the threshold power level of the voltage comparator. At this time, a signal already exists in the ω_x, ω_y

circuits and therefore the star identification detector is at a low power level and the system then transforms to the automatic tracking state.

(4) When the moon, sun, clouds and bright stars outside the required magnitude appear in the field of vision, because the increase of the noise amplifier input signal exceeds the power level of the voltage comparator threshold power level, the output is in a low electric potential. In the selective frequency amplifier channel, due to the large areas of the moon and clouds, the tuning fork scanning modulator has no exchange of signal output. Therefore, the output of the star identification detector is at a high power level and the system is still positioned in the automatic searching state.

(5) When bright stars appear in the field of vision outside of stars that exceed the required magnitude, the noise amplifier output exceeds the value of the threshold power level of the voltage comparator and in the selective frequency circuit there is also output. However, the star identification detector is positioned in a high power level and thus the system is still positioned in the searching state.

(6) When the star is located in the intermediate zero position, selective frequency channels ω_x ω_y have no output, selective frequency channels $2\omega_x$, $2\omega_y$ have output, its effect is the same as ω_x , ω_y and the system is positioned in the automatic tracking state. However, the detector that is tracking zero position comes into play and at this time the zero position display system is located in the zero position tracking state.

(7) The comparator circuit utilizes a phase sensitive detector that has no induction or tuning loop and the voltage of the self-driven oscillating circuit output of the tuning fork is regarded as the reference signal voltage. When the input stellar

error signal voltage and the phase of its reference voltage that its phase corresponds to changes from 0 degrees to 360 degrees, the output voltage of the comparator circuit is in direct ratio with the vector sum of the input signal voltage and the reference signal voltage and is a typical detection curve. For this reason, it can drive the torque electrical machinery on the altitude and bearing, and the speed measurement electrical machine causes the telescope's photoaxis to continually track the star and makes the aiming line coincide with the star.

(8) Utilizing the sums of $2\omega_x$ and $2\omega_y$ as the automatic gain control of the high voltage source of the photoelectric multiplier, when stars of comparatively bright magnitude are tracked within the required range, in order to make the output of the photoelectric multiplier within a fairly wide range be able to maintain a constant value level, the automatic gain control then can produce negative direct flow voltage that becomes proportionate to the signal. This causes the high voltage source output to change with the automatic gain control voltage. The higher the negative direct voltage produced, the lower the high voltage that is added to the photoelectric multiplier. In this way, the sensitivity of the photoelectric multiplier can then be controlled and the maintained output is a constant value.

IV. EXPERIMENTAL RESEARCH

After considering the above design principles, we developed a star tracker. The results that were obtained through stellar tracking tests are shown in the following table:

(a) 夜 間 跟 踪			
(b) 星 体 名 称	(c) 星 等 m	(d) 输出信号 (毫伏)	
(e) 大犬座 α 星 (天狼星)	-1.6	3.5	
(f) 猎户座 ϵ 星	1.8	2.3	
(g) 猎户座 δ 星	2.4	2	
(h) 黄 昏 跟 踪			
(i) 天琴座 α (织女星)	0.1	3.2	
(j) 白昼一定亮度背景下跟踪			
(k) 金 星	-3.4	3	

Key: (a) Nighttime tracking; (b) Name of stellar body; (c) Magnitude m ; (d) Output signal (millivolt); (e) Canis major α (Sirius); (f) Orion; (g) Orion; (h) Dusk tracking; (i) Lyra α (Vega); (j) Daytime tracking under a certain brightness; (k) Venus.

The above data is data that was obtained by ground receiving track tests. For example, in application on high altitude aircraft, considering that the atmospheric attenuation greatly decreases, performance will be somewhat better.

V. CONCLUSION

(1) The shortcomings of astronavigation are that it is easily influenced by meteorological conditions. Its use is limited at low altitudes but at high altitudes, especially in deep space, the influences of meteorological conditions do not exist. Due to its directional and fixed position accuracy, errors produced by the measured data do not accumulate with time; anti-interference capabilities are strong; concealment is good, etc. As a result, it obtains fairly extensive application for some particular strategic and tactical weapons required for military use such as high altitude long range warning, reconnaissance, bombing anti-submarine and other aircraft as well as guided missiles, satellites, airships, etc.

(2) In a physical sense, the astro-inertial hybrid is a fairly reasonable and comparatively accurate hybrid form. The

hybrid can make an inertial guidance system with medium range accuracy and comparatively low cost. Due to the precise astronomical measuring data, use of the Kalman filter technique is the optimal state estimate provided by the inertial guidance system, and using the optimal control mode to add the inertial guidance system's state estimate to the inertial guidance system, we thereby obtain the high precision navigational parameter output.

(3) After solving some primary technological key design criteria based on the design of the related star tracker discussed in this paper, the automatic star tracker that was developed obtained a predetermined performance target through tests. Therefore, some design criteria considered in this paper are reasonable and possess certain reference value.

References

- [1] Wang Enping, Guan Xing Dao Hang Xi Tong, [Inertial Navigation Systems], Academia Sinica, Institute for System Science, 1977.
- [2] Lei Yuanchao, ed., Guan Ying Dao Hang Xi Tong [Inertial Navigation Systems], Harbin Institute for Ship Engineering, 1978.
- [3] C.F. Aotangnaier, ed., Qun Ying, tr., Guan Ying Dao Hang Fen Xi Yu She Ji [Inertial Navigation Analysis and Design], Defense Industry Press, 1972.
- [4] Jing Xi, Ka Er Man Lu Bo Ji Qi Ying Yong Ji Chu [Foundations of the Kalman Filter and its Application], Defense Industry Press, 1973.
- [5] Yang Yuqi and Shen Gongxun, tr. and ed., Tian Wen Dao Hang [Astronavigation], Defense Industry Press, 1965.
- [6] "Celestial Trackers, Theory, Design, Applications" IEEE Transaction on Aerospace and Navigational Electronics ANE-10 No. 3, September 1963.

References (continued)

- [7] M. Kayton and W.R. Fried, "Avionics Navigation Systems," New York, 1969.
- [8] Wang Yuqi, Shen Gongxun, Qin Shiguang, Chang Qingzhi and Zhou Danian, Zu He Shi Da Hang Xi Tong Zhong Xing Ti Gen Zong Qi Yan Jiu Yu She Ji [Research and Design of Trackers in Hybrid Navigation Systems], Beijing Aviation Science and Research Report BH-B326, 1978.
- [9] "Optical Tracking Systems," Proceeding SPIE Vol. 23, 1971.

MONOPULSE TECHNIQUE IN AIRBORNE RADAR

Ji Jie

Airborne Radar Institute, China Aeronautic Research Institute

Abstract

This paper sums up the research and application of the monopulse technique in airborne radar. Discussion is focused on the key technique of the amplitude comparison system and related data is given.

The monopulse technique is viewed in light of anti-interference performance and particular applications. These applications which include air-to-ground range finding, improvement of angular resolution and terrain avoidance are expounded in this paper.

I. FOREWORD

Depending on single echo pulse to determine target angle deviation, this monopulse technique is a technique that has received serious attention since radar was discovered. Although in the early period because antenna microwave devices and other circuits were not resolved but uses cylindrical scanning as the primary system of automatic angle tracking, after waiting for the development of the sum and difference monopulse system, the application of the monopulse technique in airborne radar then became more and more extensive. Now almost all rocket control radar use this technique. In China, research and applications of the above technique also has a history of the last twenty years.

The serious attention that the monopulse technique has received is due to its many merits. The monopulse antenna's sum

beam gain can be designed higher than those of the cylindrical scanning antenna and the distance of the surveyed object can increase. The directional sensitivity will be twice as close. However, when tracking, the largest value of the antenna directional diagram illuminates the target. Therefore, in the area of energy, it has a 5.2 decibels superiority over the cylindrical scanning system. The search angle resolution is 30% better than that of the cylindrical scanning system and the tracking angle resolution will double. When the signals in the sum and difference beams undergo certain processes, they are able to further raise the angle resolution. The highest data processing speed of the system which is the pulse repetition frequency is one quantity level higher than that of the cylindrical scanning system. The three channel monopulse system eliminates the instability of the tracking system that is caused by the bearing in the cylindrical scanning system and the pitch channel cross coupling, greatly improving the quality of angle tracking. Many references have expounded the above subjects and this paper is not prepared to discuss them. One outstanding advantage of the monopulse system which this paper will discuss in detail is its anti-interference capabilities in relation to airborne radar. Additionally, airborne radar will also take into consideration the particular applications of multiple beam information which this paper will present in separate sections.

According to its actual possible conditions, the monopulse system can be divided into the two categories of amplitude comparison and phase comparison. According to a combination of different directional methods and different angle measurement discriminators it can be further divided into nine types of basic systems. The vibration amplitude-sum and difference type is commonly used in airborne radar, that is, we use the antenna's amplitude direction and sum and difference angle discriminator to determine the directional properties of the system. This

system is not too stringent on receiving consistent requirements of the branch circuit properties. The phase-sum and difference is only used for the slot array plate antenna with wave guide feed. Other forms of monopulse systems which have not been seen applied in airborne radar will not be discussed in this paper.

The monopulse technique was originally only used in tracking radar. Now it has also been applied in searching radar. Utilizing a digital electronic computer and beam scanner antenna it realizes the functions of both searching and tracking. Additionally, it also jointly used with the pulse Doppler technique, phased array technique, frequency agility, pulse compression and other radar techniques. Thus, a series of new technological problems emerges.

II. THE TYPICAL AIRBORNE MONOPULSE SYSTEM AND ITS KEY TECHNICAL PROBLEMS

Because airborne radar has stringent requirements in volume, weight and dependability, a series of key technical problems exists in areas of the formation, amplification and processing of the monopulse signal, and ensuring of the gain and phase consistency. Based on experiences in development, the following section focuses discussion on several problems.

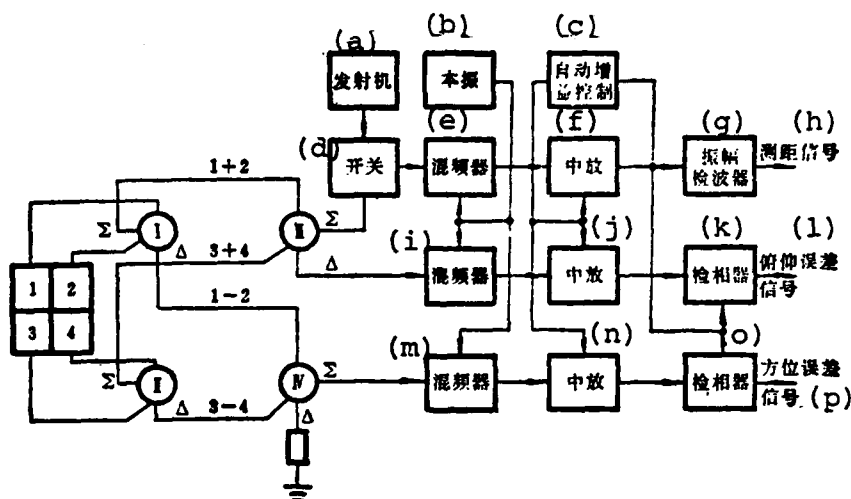


Fig. 1. Block diagram of a two-dimensional monopulse system.

Key: (a) Transmitter; (b) Local oscillator; (c) Automatic gain control (d) Switch; (e) Mixer; (f) Center release; (g) Amplitude detector; (h) Range signal; (i) Mixer; (j) Center release; (k) Phase detector; (l) Pitching error signal; (m) Mixer; (n) Center release; (o) Phase detector; (p) Bearing error signal.

- $\Delta\theta$ is the error angle
- G_A is the antenna directional diagram's normalized slope on the aiming line, generally the antenna can approximately be a $\pi/0$ value center beam angle;
- g_1 is the specific value of the transmission coefficient in the passage in front of the sum and difference instrument;
- g_2 is the specific value of the transmission coefficient in the passage in back of the sum and difference instrument;
- ϕ_1 is the phase shift difference in the passage in front of the sum and difference instrument;
- ϕ_2 is the phase shift difference in the passage in back of the sum and difference instrument

The monopulse system's output directional error angle is approximately expressed as: $\Delta\theta = \frac{1}{2G_A} [(1-g_1) - \phi_1 \text{tg } \phi_2]$ (1)

Measurement angle sensitivity

$$\left. \frac{ds(\theta)}{d\theta} \right|_{\theta=0} = G_A g_2 \cos \phi_1 \quad (2)$$

From the relational expression, we can see that the transmission coefficient in the channel in front of the sum and difference instrument and the phase shift measurement cannot consistently produce directional angle error. In order to have comparatively good performance within the fairly wide frequency band range, in front of the sum and difference instrument do not install an active component, as much as possible shorten the length of the beam in front of the sum and difference instrument and make its length equal. In reality, there is already no way of measuring the transmission coefficient in front of the sum and difference instrument and the phase shift quantity. Frequently we use the two new practical parameters of zero point drift and zero value depth of the difference beam. Because the zero point drift that the transmission coefficient in the passage does not consistently produce can be determined by measurement, the zero value depth is a power level decibel number of an antenna difference beam zero point with a sum and difference instrument that is lower than the peak value of the sum beam. It is determined by the different beam's relative separation angle and the phase difference value in front of the sum and difference instrument. The typical value of airborne radar is better than 30 decibels. The phase difference in the passageway of the output from the sum and difference instrument changes 180° close to the zero point and variation slope is determined by the zero value depth. When the zero value depth is better than 30 decibels, the phase shift difference value in front of the sum and difference instrument only has very few degrees and the phase difference's variation slope is already very big. The zero point drift quantities produced by the several ten degree phase difference in back of the sum and difference instrument can all be overlooked. Formula (2) explains the relationship of the transmission coefficient in back of the sum and difference instrument and the directional sensitivity variation caused by phase shift inconsistency. Typical airborne radar allows directional sensitivity

to vary $\pm 50\%$. Therefore, the requirement for transmission coefficient inconsistency generally is 2 decibels and the requirement for phase shift inconsistency generally is $30^\circ \sim 45^\circ$.

In microwave systems, the standing wave coefficient of the unmatching component linkage will be the function of frequency. The unmatching not only brings about the variation of the amplitude of each circuit signal but also causes inconsistent phase shift to appear in each circuit signal. In monopulse radar with a beam width of 5 degrees and a 1.25 standing wave coefficient will cause a zero point drift with the largest value being 0.7 micrometers and an angle sensitivity variation with the largest value being 2.4%.

The relative gain differences in back of the sum and difference instrument and the inequality of the phase shift quantity primarily arise from the resonant cavity of the receiver protecting discharge tube and the intermediate frequency amplifier. When the Q values of the two narrow band discharge tubes have differences of 10%, the tuning deviations reach one fifth of the bandwidth, and when the signal frequency deviates to the communication band edge, the attenuation difference value reaches 1.5 decibels or higher. In the process of discharge tube recovery, it is still possible to create an even larger phase shift difference. Therefore, the receiver protecting discharge tube should possess a comparatively wide frequency band or utilize the protecting device without a resonance cavity and extremely short recovery time. The intermediate frequency amplifier must fully ensure the consistency of the gains and the communication band conditions when debugging so as not to let large relative gain differences and phase shift differences emerge when frequency and temperature vary. The automatic gain control generally must control a receiver dynamic-state range of 60 decibels or higher or it will cause very great gain differences and phase

shift differences. In order to block the magnetic transfer in each circuit and reduce the imbalance of control, airborne radar generally will separately add the tunable wave filter output level with automatic gain control voltage passing the transmission coefficient to the intermediate frequency amplifier in each circuit. This measure can cause gain differences not to be greater than 20% and phase shift differences not to be greater than 10 degrees.

The magnetic transfer in the wave guide and electric cable of each circuit will form difference beam zero point drift. To make the drift less than 5% of the beam angle, magnetic transfer power should be lower than -20 decibels.

The antenna is the key component in monopulse radar. The applications of the waveguide feed radiator that extends from the parabolic reflecting surface center are fairly extensive. The radiator is separated by the extended waveguide dividing it into two groups wherein each irradiates half the reflecting surface thereby decreasing the use of the antenna aperture. Yet, this structure is very compact and the extended waveguide is used to construct the sum and difference instrument of all horn signal microwave processing. This structure makes the waveguide length in front of the sum and difference instrument reach the shortest level and it can obtain a zero value depth of -30 decibels. This sum and difference instrument is composed of slotted waveguide bridge components such as the two 3 decibel side wall couplers, the two 3 decibel top wall couplers, the two $+90^\circ$ fast shift wave circuits and the two -90° slow shift waves. The signal-flow graph and phase relationship when transmitting is shown in Fig. 2. The transmitted energy is divided to four horn orifices from four summing circuits. The phase-shift to each horn orifice uniformly is -90° and they are relatively the same. The phase relationship of each point from each horn reaching

the graph and the four output ends when receiving is shown in Fig. 1. From the phase of points A, B and C we can see that the four horn signals realize sum and difference processing there.

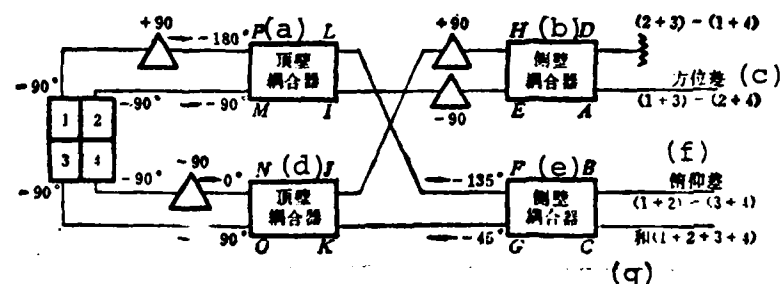


Fig. 2. Signal-flow graph and phase relationship when transmitting.

Key: (a) Top wall coupler; (b) Side wall coupler; (c) Bearing error; (d) Top wall coupler; (e) Side wall coupler; (f) Pitching error; (g) Sum.

TABLE 1: RELATIONSHIP OF PHASE OF FEED SYSTEM WHEN RECEIVING

(a)	(b) 各 点 相 位															
	P	O	N	M	L	K	J	I	H	G	F	E	D	C	B	A
1	+90°				+45°			+135°			+45°	+45°	-90°	-90°	0	0
2				0	+45°			-45°			+45°	-135°	+90°	-90°	0	-180°
3		0				-45°	+45°		+135°	-45°			+90°	-90°	-180°	0
4			-90°			-45°	-135°		-45°	-45°			-90°	-90°	-180°	-180°

Key: (a) Loudspeaker of received echo; (b) Phase of each point.

The further development of airborne radar produced the Cassegrain antenna. The feed source of this antenna is in the center of the parabolic reflecting surface and uses a hyperboloid as the auxiliary reflecting surface. It both raises the use of the antenna orifice surface and increases antenna gains. It can also cause the structural dimension in front of the parabolic surface to reduce by half. As to ray polarization waves, the cover of the auxiliary reflecting surface uses a grid

structure and a polarized reverse reflecting surface to resolve it. When this antenna is matched with a multimode horn feed source, this can make the structural dimensions extremely compact. The corrected reflecting surface design can obtain very low side lobe power level. What presently is even more extensively used is the inverted Cassegrain antenna. Its first reflecting surface is a grid parabolic surface. The second reflecting surface is a polarized reverse plane. This structure, besides possessing the advantages of the above-mentioned Cassegrain antenna, due to the deflection of the beam, only relies on the rotation of the polarized inverted reflecting surface to omit the rotation link of the waveguide. The feed source and microwave components, and receiver and transmitter can be firmly linked together. The inverted Cassegrain antenna has loss in tracking precision of the rotational angle and antenna gains. The former can use the computer for correction and when the latter is in a beam rotational angle not greater than $\pm 65^\circ$, the gain loss within the wide frequency band range is not greater than 0.5 decibels.

The multimode feed source for the single horn is one of the keys of monopulse radar obtaining good performance and it is already has extensively applied. The sum signal of the multimode feed source utilizes model TE_{10} , the difference signal on surface H utilizes model TE_{20} asymmetrical electrical field, surface E utilizes a TM_{31} (or TE_{11}) and model M_{11} composite asymmetrical electrical field. These two asymmetrical electrical fields possess properties that are needed for the difference circuit signal. Because the multimode feed source only has one horn orifice, it then has three primary strong points. (1) Its efficiency with the antenna coupling exceeds and is even the "optimum" antenna feed source. (2) It possesses symmetrical short structures, aiming performance is good and electrical axis stability is not related to frequency. Polar changing within a 10% frequency width range reaches 30 decibel zero value depth.

(3) The structure is compact and simple. Therefore loss is low, weight is light, and the aperture cover is small. The shortcoming is that the formed circular polarization will make the feed source become very complex.

III. MONOPULSE TECHNIQUE USED IN MEASURING ANGLES IN AIRBORNE RADAR

Airborne rocket control radar that utilize monopulse techniques are primarily used in measuring angles and tracking angles of targets. Angle tracking of a single object frequently is achieved together with distance tracking of a single object. Measuring angles of many targets is achieved in monopulse search radar.

As for the factors that influence angle measurement precision in airborne monopulse radar, aside from the amplitude of the receiving circuit that was already discussed in the previous section and the directional error caused by the phase inconsistency, the amplitude of the echo signal fluctuates past the limited bandwidth of the automatic gain control circuit increasing the dynamic-state directional error. Target angle measurement scintillation and the internal noise of the receiver are also primary factors of directional error. Because airborne radar generally uses the linear polarization antenna, the polarization distortion of the complex target echo signal also is a factor worth noting. The cross polarization directional diagram of most antennas can produce very large deformation and an equal strength signal direction possibly deflects on to the half power beam direction. The grid mesh structure can inhibit the cross polarization weight and reduce its harmful influence.

In monopulse search radar which measures the angle of multiple targets, the receiver cannot use automatic gain control normalization. The normalization of the sum and difference signal

uses the division circuit or the subtraction circuit behind the phase detector (logarithmic intermediate frequency amplifier) for processing. The normalized error signals for the computer carry out digital tracking of the many targets or are used for real time corrections of the outputs of antenna coordinates.

The widespread applications of the monopulse technique in airborne radar are primarily due to the fact that its angle measurement anti-interference performance is fairly good. In angle measurement, the monopulse system is not sensitive to the amplitude fluctuations of the echo signal. The amplitude modulation interference, frequency modulation and phase modulation interference of the single interference source are not only not harmful to angle measurement, but on the contrary because the strengthening of the echo signal causes the tracking distance to increase, the tracking errors decrease. Yet, because strong interference can cause error signal saturation, it can cause a break in the tracking process. The interference of the control key can both cause periodic overload of the receiver and can cause control key frequency to go through the resonant properties of the automatic gain control and tracking system so that the antenna produces angular pursuit pendulum. For the coherent interference, scintillation interference or scan frequency interference produced by the space multiple-points, the monopulse systems can receive interference in the same way. Because these interferences are based on causing the electromagnetic wave wave-fronts that reach the radar antenna to produce distortion in these three interferences, the cost of realizing coherent interference is fairly high and the threat to the radar is not large. Scintillation interference will cause the antenna pursuit arrangement to reach the 80% of the included angle in the jammer. It should cause the interference signal to be nine decibels stronger than the echo signal. Scan frequency interference then uses the effect of the receiver's communication frequency band

and the result is the same as with scintillation interference. Radar within the scan frequency range will always receive interference. Because the target of airborne radar possibly forms or utilizes the wingspan to form multiple point interference, the possible harm of this interference is fairly large. Another effective interference for the monopulse system is the use of the cross polarization directional diagram to cause the radar's directional properties to produce cross polarization interference of the distortion. Cross polarization interference also causes an intense coupling effect to be produced between the bearing branch circuit and the pitching branch circuit, thereby bringing about the fixed phase mismatch of the tracking system. In the area of its ability to inhibit clutter, tests prove that it advanced 23 decibels more than the cylindrical scanning radar. From the above discussion we can see that theoretically the monopulse system can counter many kinds of interference. Although there are several other kinds of interference that can still jam it, all in all its anti-interference capabilities are much better than those of cylindrical scanning radar. This is because in the area of electronic countermeasures, there has never been a perfectly sound plan.

Airborne radar utilizes the monopulse technique to measure angles, although in the area of method error there is some decline. Yet, other error items under airborne conditions still play a marked role. In angle measurement precision, airborne monopulse radar and non-monopulse radar belong to the same quantitative level and there are no obvious breakthroughs. Contrasting them, in actual application the raising of anti-interference capabilities is common knowledge. The inverse interference, to specially cope with the cylindrical scanning radar has no influence at all on the monopulse rada..

IV. PARTICULAR APPLICATIONS OF THE MONOPULSE TECHNIQUE IN AIRBORNE RADAR

In airborne radar, the monopulse technique is not only used to measure angles, but is also used for accurate range finding on the ground, improvement of resolution and terrain avoidance. Many terrain avoidances and terrain operational principles that follow airborne radar go so far as to completely rely on monopulse techniques. Because these applications have not received the attention that they should in other literature on the monopulse technique, this text will discuss them in greater length.

The slanting distance of the single beam radar measurement to the ground is very sketchy. Because the beam width in airborne radar cannot be too narrow, the distance section of the beam that irradiates to the ground is very long, and the slanting distance measurement of certain targets on this inevitably have very large errors. The pitching difference beam signal of the monopulse system provides the possibility of precise range finding. The difference beam phase detection video-frequency signal changes polarity in the area of distance D_2 (time delay t_2) aimed at by the aiming line. Based on the zero point measured time delay of this changed polarity signal, or using the automatic tracking of the tracking distance's wave gate we then can accurately measure slanting distance D_2 . The angle aiming of the target that requires a measured distance cannot depend on the radar but generally is aimed by visual optics. Aside from the automatic range finding of ground targets, this is applied to topographical tracking radar which measures the slanting distance of topographical contours to obtain comparatively high range finding precision.

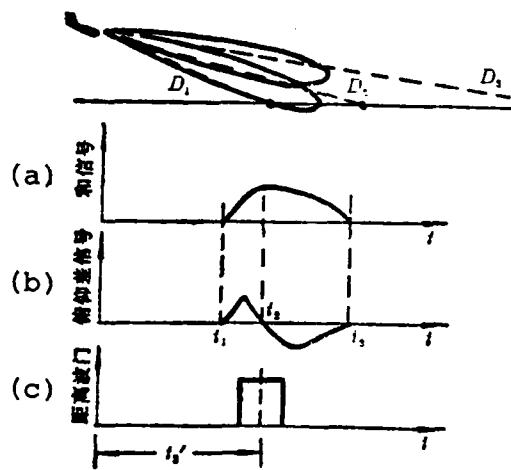


Fig. 3. Wave form on ground range finding.
Key: (a) Sum signal; (b) pitching difference signal; (c) Distance wave gate.

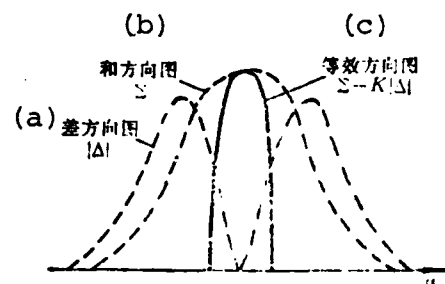


Fig. 4. Improvement of bearing resolution.
Key: (a) Difference directional diagram; (b) Sum directional diagram; (c) Equivalent directional diagram.

Monopulse techniques are used for the improvement of angular resolution and it has many applications in airborne radar. Its basic principle is utilizing sum and difference signals for suitable processing so as to raise the target's angular resolution. The improvement of the bearing resolution is processed according to the reduction of absolute values of the sum circuit video-frequency pulse and the K-times difference circuit video-frequency pulse. The circuit inhibits the negative pulses and only outputs positive pulses. The equivalent antenna directional diagram of the point target is a narrow beam that is positioned close to the center of the beam (see Fig. 4). Selecting $K=1$ can cause the improvement of the resolution to be 1.5 times the original resolution. For a single target, increasing the K value can cause the equivalent directional diagram to further become narrow. For example, we can raise the resolution for a single target 15 times, but in reality, this has already lost the

AD-A127 983

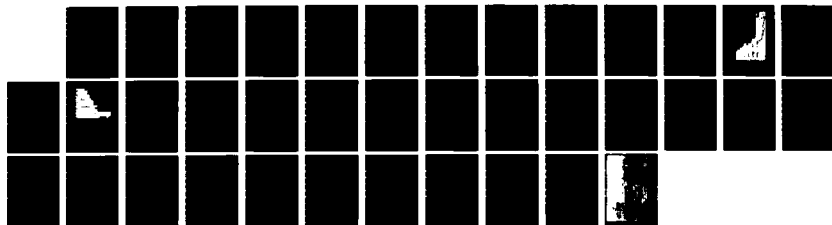
ACTA AERONAUTICA ET ASTRONAUTICA SINICA(U) FOREIGN
TECHNOLOGY DIV WRIGHT-PATTERSON AFB OH F QIAN ET AL.
04 MAR 83 FTD-ID(R5)T-0664-82

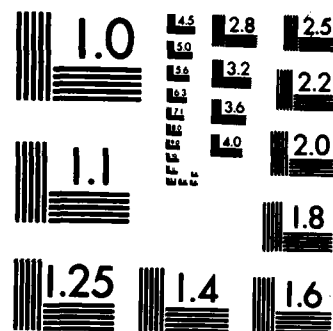
3/3

UNCLASSIFIED

F/G 20/4

NL





MICROCOPY RESOLUTION TEST CHART
NATIONAL BUREAU OF STANDARDS-1963-A

significance of resolution. Multiple targets in the real beam of the antenna do not possess the above-mentioned equivalent directional diagram. The maximum improved ability of the bearing resolution in only 2.1 times and what exceeds this value is only a measure of reducing the angle range of the radar display. The mutual reducing processing of the sum circuit signal and the K-times difference circuit signal will cause the noise power to increase to $(K+1)$ times. When $K=1$, the operating distance drops approximately 20%. When $K=20$, the operating distance will drop 54%. Another method to reduce the angle range of the radar display is using the difference signal to make real time corrections on the oscilloscope tube deflection signal. That is, the deflection signal, aside from the computations obtained from distance D and bearing scanning angle α , also includes a correction term of the video-frequency pulse of the bearing difference circuit phase detector output. The expressions are as follows:

$$x = D \cos \alpha - \Delta \alpha D \sin \alpha \quad (3)$$

$$y = D \sin \alpha + \Delta \alpha D \cos \alpha \quad (4)$$

The circuit with the realized real time correction is comparatively complex, but it cannot lose the signal-noise ratio and is beneficial to maintaining the operating distance.

What the monopulse technique in airborne radar first realized when used for terrain avoidance was displaying on the display the topographic scanned surface with a very wide bearing angle. This method is called terrain avoidance and it began to be used abroad during the 1950's. Following the lowering of flight altitude, an E model display was used to show the front topographical contours (curve of pitching angle-slant distance) with narrow level surfaces and wide vertical surfaces; or while using a very wide beam of the phase interferometer technique on the

vertical surface to carry out the level scan, use a display to show certain fixed distance topographic cross tangent planes (curve of pitching angle-bearing angle). Although the display of these two topographies can be realized, yet they are rarely used. With the development of aircraft automatic control techniques, topographical tracking radar was extensively applied. The antenna beam of this kind of radar carries out vertical scanning on aircraft velocity vector directions. The computer, based on the slanting distance and pitching angle of the topography surveyed by the radar, computes the operational commands of the aircraft, causing the aircraft to maneuver vertically in accordance with the topography and to maintain flight according to a predetermined altitude interval. The above various ways of terrain avoidance operations all utilize monopulse techniques to carry out radar survey of the topography.

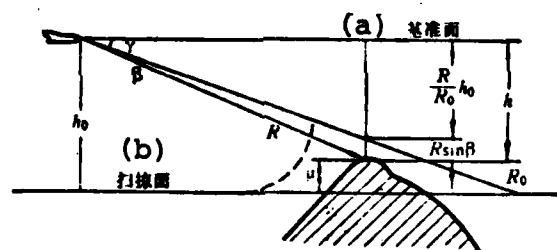


Fig. 5. Geometric figure of terrain avoidance.

Key: (a) Datum surface; (b) Scanning surface

- h_0 - interval of adjusted datum surface and scanning surface;
- R_0 - distance of selected antenna axis and scanning surface crossing point; some were selected as 5 nautical miles, some were selected as 10 nautical miles;
- γ - antenna pitching angle given according to scanning surface's adjusted value;

- R - real distance to the topographic obstacle;
- β - included angle of the obstacle and antenna axis; above the axis is positive, below the axis is negative;
- n - $n = \frac{R}{O} h_o - R \sin \beta$;
- μ - height of obstacle extended scanning surface; above the surface is positive, below is negative.

The basic operational principle of using a monopulse system to achieve terrain avoidance is the use of the sum and difference signal of the monopulse video-frequency to carry out processing and computations of the signals in the geometric diagram. In order to show the obstacle that is higher than the scanning surface, we must compute in real time the highest point of each obstacle above the scanning surface or below the scanning surface. In the diagram:

$$\mu = h_o - R \sin(\gamma - \beta) = h_o - \frac{R}{R_o} h_o + R \sin \beta \quad (5)$$

Because angles γ and β are both very small, the above formula can approximately be:

$$\mu = h_o - R \left(\frac{h_o}{R_o} - \beta \right) \quad (6)$$

In monopulse radar, h_o is expressed by pulse voltage $h_o E_s$. At this point E_s is the sum circuit video-frequency pulse, h_o is the variable proportionality coefficient and can use a potentiometer to change. The β angle is expressed by the normalized value $E_d/E_{smax} = K E_d$ of pitching difference circuit video-frequency pulse. After these two pulses are added to each other, they are multiplied with a sawtooth voltage using the complete multiplication of R. The negative pulse of the multiplication result is then added with the $h_o E_s$ pulse which completes the analogue computation of approximation formula (6). If the computed result is a positive pulse, this explains that $\mu > 0$ which would be shown on

the display. If the computed result is a negative pulse, this explains that $\mu < 0$ which would not be indicated. The datum surface in the figure is of three kinds. If we select a level plane of the earth as the datum surface, the scanning surface would be called an equi-altitude surface; if we selected the plane of the aircraft axis as the datum surface, the scanning surface would be called the terrain avoidance scanning surface; if we selected the plane of the aircraft velocity vector as the datum surface, the scanning surface would be called the smooth scanning surface under the aircraft. The corresponding different datum surfaces should determine the angles under different antenna pitch. Aside from this, the signal processing methods of the three scanning surfaces then are completely identical. If the scanning surface is not a plane but is a curved surface rolling up from outside a certain distance (as the broken line in the figure shows), it is a sled form scanning surface. This scanning surface needs a correction of adding $\frac{1}{2}at^2$ on h_0 which can be realized by using the parabolic waveform in the analogue circuit. The corrected results can cause an aircraft at a certain velocity with a certain duration to take a certain overload as the vertical and maneuver and fly passed the obstruction. For example, when the scanning surface is positioned at 170m, the aircraft with a velocity of 250m/seconds has a duration of 10 to 12 seconds in which it can fly passed the obstruction with an overload of $a=0.1g$. The terrain avoidance method is generally processed using video-frequency pulse in an analogue computer circuit; total errors can reach several hundred meters. When the aircraft altitude is fairly low, this operational method has no way of satisfying the requirements.

The topographical tracking operation method that possesses fairly high precision uses the monopulse technique to accurately measure the terrain avoidance parameters. There are three concrete methods: outside the aiming line method, above the compared

amplitude aiming line method, and above the compared phase aiming line method. In the outside the aiming line method the beam does not scan and at the same time the angle and distance of the targets that are within the range of the beam are measured. Because this radar's survey distance is small, measurement errors are large and the mapping of the topographical contour is not detailed. It can only make flights from mountain top to mountain top. The above compared amplitude aiming line method uses monopulse bearing resolution to improve circuit processing and error signal to obtain a fairly narrow equivalent pitching directional diagram, or utilizes monopulse to measure a fairly high precision of ground surface slanting distance. The beam center line follows the antenna's mechanical scanning and makes sweeps on the vertical surface completely measuring the pitching angle and distance of the topographical contour. The above compared phase aiming line method is also called the interferometer method. Although the pitching beam of the interferometer is comparatively wide, the pitching difference circuit phase detection video-frequency signal near the aiming axis changes the polarization quality and it forms a very narrow angle gate signal to control the output of the sum circuit video-frequency signal. A good design can cause the angle range to shrink over 100 times, reaching the equivalent beam width of zero point several degrees. The angle wave gate can use digital circuit control and the data processing speed is very high which can reach 10 cycles per second. Moreover, equivalent beam processing can be simultaneously carried out with the bearing scanning of the antenna. It can realize simultaneous terrain avoidance and tracking processing.

V. CONCLUSION

The applications of the monopulse technique in airborne radar, whether for measuring angles, antijamming, improving resolution, air to ground use, etc., have very great practical value. Therefore, airborne radar mostly utilizes this technique. It is

especially indispensable in those areas which have air to air functions as well as multifunction radar which possess air to ground functions and low altitude avoidance functions.

Airborne radar utilizes the starting point of the monopulse technique and has some differences from ground radar. The primary goal of ground radar utilizing the monopulse technique is for the purpose of raising to a large extent angle measurement precision and obtaining fairly high data processing speed. Airborne radar is frequently used for antijamming, multiple beam signals and other goals.

The monopulse technique only resolves angle measurement of radar or some problems related to it. Modern radar also employs some other new techniques to resolve other problems that we are faced with. Because the monopulse system needs many beams and many circuit receiving branch circuits, the requirements of relative gain in sum and difference branch circuits and phase shift consistency will make the application of other techniques complex. For example, frequency agility requires the radar to operate in a fairly wide frequency band. In a fairly wide frequency band will it need to maintain relative gain and phase shift consistency on each frequency? What about the system performance if we do not adopt maintenance measures? These questions all need to be researched. Another example is that although various channels of research were carried out on monopulse channel merging techniques in the 1950's, in the past most airborne radar did not use it and generally there are still the three typical channel receivers. Yet, in pulsed Doppler radar, the narrow band filter made phase consistency very hard to ensure and there already was radar using the channel merging technique. But channel merging will cause the signal-noise ratio to decline; many beams and much target information has no way of being used; information speed drops; anti-interference performance declines; and cross coupling in the bearing and pitching

channels newly emerges. In the face of these new research problems, we still have many new contradictions awaiting research and resolution.

References

- A.N.)
- [1] Liangnuofu, et al, Editor, Translated by Huang Hong, Dan Mai Chong Lei Da. [Monopulse Radar], Defense Industry Press, 1974.
 - [2] M.I. Skolnik, Editor, Translated by Xie Zhuo, Lei Da Shou Ce, [Radar Handbook], Book 8, Defense Industry Press, 1974.
 - [3] Dan Mai Chong Lei Da Jin Xing Di Za Bo Fen Bian De Shi Yan Yan Jiu, [Experimental Research in Monopulse Radar Carrying out Clutter Differentiation], IRE 4th National Con. on Military Electronics, 1960.

MECHANISM OF STRESS CORROSION AND HYDROGEN INDUCED CRACKING

Zhu Wuyang, Li Shiqiong, Xiao Jimei and Zhu Shuyan
Beijing Institute of Iron and Steel Technology

Abstract

The production and expansion of stress corrosion cracking and hydrogen induced cracking was tracked and observed in various hydrogenant environments (e.g. electrolytic charged hydrogen, H_2 and H_2S gases, water, aqueous solution of H_2S etc.) for four types of low alloy steel with different strengths using polished constant displacement specimens. Results showed that after the strength of steel and K_I are larger than a critical value, hydrogen induced delayed plasticity deformation can be produced in any hydrogenant environment, that is, following the diffusion entrance of the atomic hydrogen the plastic zone and its deformation degree on the front end of the original crack enlarged continuously. When the hydrogen induced delayed plasticity deformation develops to a critical condition, this can cause the nucleation and expansion of the hydrogen induced delayed cracking.

We used the smooth tensile specimen, bending specimen, type I, type III as well as I-III complex precrack specimen to research the influence of hydrogen on apparent yield strength. Results showed that for the smooth tensile and precrack twist specimens, the influence of hydrogen on yield strength is not noticeable. However, in specimens with tensile stress gradient (e.g. bending specimens, type I or complex precrack specimens), when the strength of steel and the amount of entering hydrogen exceed critical value, the hydrogen can noticeably decrease the apparent yield stress. This is the cause of hydrogen induced delayed plastic deformation. Based on the dependent relationship of the apparent yield strength on the entering hydrogen

amount and strength, we can explain the dependent relationship of K_{ISCC} and da/dt on strength and environment.

We researched the effects of deformation speed, test temperature and the pre-plastic deformation level on hydrogen induced apparent yield strength reduction. With this foundation, we investigated the reasons for the hydrogen reducing the apparent yield strength.

I. FOREWORD

At present, it is widely considered that the stress corrosion of low alloy steel is a process of hydrogen-induced cracking, but a large controversy exists on the mechanism of hydrogen-induced cracking (i.e. "hydrogen embrittlement") [1-4]. We used a polished WOL type constant displacement specimen, bringing load under a microscope for the tracking and observation of ultra-high strength steel in the process of stress corrosion cracking nucleation and expansion in a water medium, and successfully revealed the interrelation of stress corrosion cracking and delayed plasticity deformation. We propose a new concept that hydrogen-induced delayed plasticity deformation causes hydrogen-induced delayed cracking [5].

This work carried out systematic tracking and observation on the stress corrosion cracking and hydrogen induced cracking process of four low alloy steels under various hydrogenant environments.

If we consider that hydrogen can clearly reduce the apparent yielding strength of steel, then it would be very easy to explain hydrogen-induced delay plasticity deformation. Although there still is controversy [4,6], most workers consider that the effect of hydrogen on the yielding strength of a tensile specimen

is not great. Because stress gradation exists on the front end of a type I crack, three directions of stress and initial plasticity regions exist. Is it due to the existence of these factors that can cause apparent yielding to noticeably drop? For this reason, aside from a smooth tensile specimen, we also used a three point bending specimen (where tensile stress gradation exists), type I, type III and I-III complex precracked specimens to research the influence of stress gradation, three directional stress conditions, and pre-existing plasticity regions on apparent yield strength after charged hydrogen. Additionally, we also carried out research on the strength of steel, initial hydrogen content (altogether there are nine charged hydrogen conditions), test temperature (-110° to 15°C) as well as load velocity ($0.01 \sim 2\text{mm/seconds}$) and other factors. On this foundation, we investigate the hydrogen-induced delayed plasticity deformation mechanism.



Fig. 1. Ultra-high strength steel ($30\text{CrMnSiNi}_2\text{A}$, No. 8, $\sigma_b = 161\text{kg/mm}^2$) process of stress corrosion crack production and expansion of hydrogen-induced delayed plasticity in a water medium; positive pole polarization. Time unit: hours.

Key: (1) mm.

II. TEST PROCESS

For the composition, heat treatment technique and mechanism performance of the tested steel see references [7,8]. When conducting metallographic tracking and observation we fully used a polished constant displacement specimen. For test results see references [9,10].

The specimens that were used to research the influence of hydrogen on apparent yield stress are a smooth tensile specimen ($D=10\text{mm}$), a three point bending specimen ($12\times 12\text{mm}$), a WOL specimen ($B=20\text{mm}$) and I-III complex type specimen (a cylinder inlet specimen that is $D=40\text{mm}$, $d/D=0.4$, pre-cracked). The following several types of charged hydrogen conditions were used : in the H_2SO_4 solution with $\text{pH}=4, 3, 2, 0.1$, soaked for 13 hours; in the $1\text{N H}_2\text{SO}_4$ ($\text{pH}=0.1$) solution electrolyzed charged hydrogen for 13 hours, the current densities separately are $0.2, 1.0, 5.0, 20, 50$ and 80 milliamperes/ cm^2 . The load velocities (crossbeam displacement velocity) separately are $2, 1, 0.15, 0.07, 0.01\text{mm/second}$. Test temperature was -110°C to 15°C .

III. TEST RESULTS

1. Production and Expansion of Stress Corrosion Cracking

Fig. 1 is the process of the production and expansion of hydrogen-induced delayed plasticity deformation and stress corrosion cracking on ultra-high strength steel when there is stress in an aqueous environment, in rigid load and when a plasticity region exists in the front end of the crack (see Fig. 1(a)). If the specimen is placed in the desiccator, then this plasticity region does not change. After being placed in the water, the size of this plasticity region and its deformation rate gradually increase with the time extension (Fig. 1(b)), that is, hydrogen-

induced delayed plasticity deformation is produced. After the delayed plasticity region closes, then in the above-mentioned place, stress corrosion cracking is produced (Figs. 1 (c) and (d)). At the same time, in the front end of this non-continuous crack the second plasticity region is also produced (see Fig. 1(d)). In the dark field, the smooth shift line in the plasticity region is a bright rippled line and stress corrosion cracking assumes a thin brown line. Following the development of hydrogen-induced plasticity deformation, the above process was continually repeated and these non-continuous stress corrosion cracks also gradually link with each other (Fig. 1(f)).

Tracking and observation of other ultra-high strength steel specimens (e.g. the 30CrMnSiNi₂A where $\sigma_b \geq 161 \text{ kg/mm}^2$; the 40CrNiMoA where $\sigma_b = 185 \text{ kg/mm}^2$, and the ZG-18 cast steel where $\sigma_b = 160 \text{ kg/mm}^2$) also shows that so long as $K_I > K_{ISCC}$, then hydrogen-induced delayed plasticity deformation certainly can be produced and moreover it is a precondition of stress corrosion cracking.

If steel strength is fairly low, then the relationship of hydrogen-induced delayed plasticity deformation and hydrogen-induced delayed cracking has slight differences as shown in Fig. 2. When hydrogen-induced delayed plasticity deformation reaches a critical state, cracks continually expand forward along the plasticity region boundaries. The figure already uses A, B, C and D to show the crack position at different times. On the other steel specimens of comparatively low strength (30CrMnSiNi₂A where $\sigma_b = 126 \sim 147 \text{ kg/mm}^2$; 40 CrNiMoA where $\sigma_b = 135 \sim 143 \text{ kg/mm}^2$; and 30CrMnSiA), the results that were gained are completely identical.

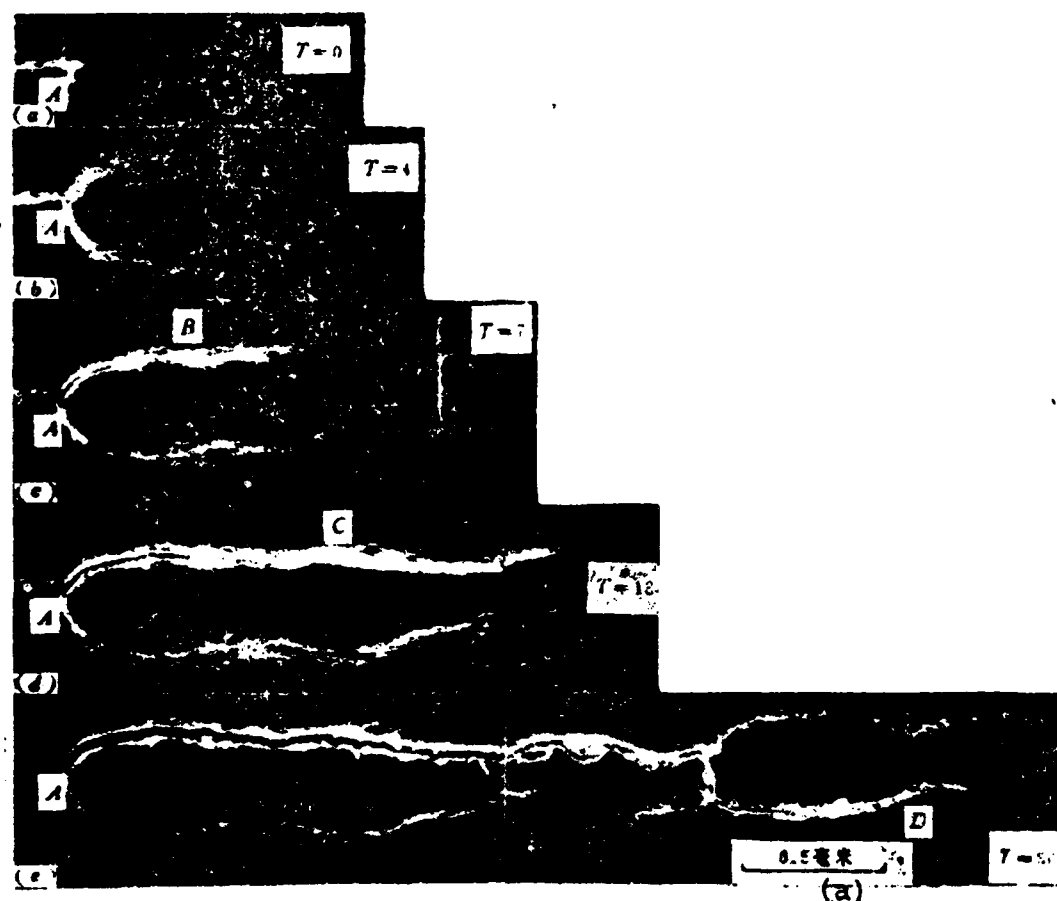


Fig. 2. Fairly low-strength steel (40CrNiMoA, No. 19, $\sigma_b=143\text{kg/mm}^2$; the production and expansion of hydrogen-induced delayed plasticity deformation and stress corrosion cracking in a water medium. Unit: hours.

Key: (a) mm.

In a water medium, negative pole polarization (copper makes a negative pole, 0.5~1 volt), positive pole polarization (magnesium makes a positive pole, 0.5~1 volt) and adding a slow corroding agent ($0.1\text{N K}_2\text{Cr}_2\text{O}_7$) do not influence the above conclusions. In the H_2S aqueous solution [9] and alcohol, acetone and other organic solutions that contain a small amount of water (0.3%), hydrogen-induced delayed plasticity deformation causes the relation of the production and expansion of stress corrosion cracking to be the same as in the water medium.

2. Production and Expansion of Hydrogen-Induced Delayed Cracking

We carried out detailed research on the production and expansion of electrolyzed charged hydrogen and hydrogen-induced delayed cracking in H_2 or H_2S gas [10]. The results show that after K_I is larger than the critical value, the front end of the load crack can produce hydrogen-induced delayed plasticity deformation, thereby causing the nucleation and expansion of hydrogen-induced cracks. On ultra-high strength steel (e.g., 30CrMnSiNi₂A, No. 8, $\sigma_b=161\text{kg/mm}^2$; No. 6, $\sigma_b=166\text{kg/mm}^2$; No. 1, $\sigma_b=180\text{kg/mm}^2$ 40CrNiMoA, No. 18, $\sigma_b=185\text{kg/mm}^2$, the end points of the delayed plasticity region form non-continuous hydrogen-induced cracking. On fairly low-strength steel (e.g. 30CrMnSiNi₂A, No. 12, $\sigma_b=126\text{kg/mm}^2$, 30CrNiMoA, No. 19, $\sigma_b=143\text{kg/mm}^2$, 30CrMnSiA, No. 16, $\sigma_b=145\text{kg/mm}^2$), then hydrogen-induced cracking continually expands along the delayed plasticity region boundary [10].

Tests show that when there is electrolyzing charged hydrogen, because surface layer concentration is high, nucleation of hydrogen-induced cracking on the surface layer is even earlier and development is even faster, When delayed plasticity deformation appears on the specimen surface, regardless of whether it is on the specimen surface or inside the specimen, they still do not produce hydrogen-induced cracking [10,11]. This shows that the delayed plasticity deformation that is seen on the specimen surface is not a predetermined interior formation caused by the crack, it can only be caused by the hydrogen. Therefore, hydrogen-induced delayed plasticity deformation is a necessity and a prerequisite for hydrogen-induced delayed cracking and stress corrosion cracking.

3. Influence of Hydrogen on Apparent Yield Strength

(1) Smooth Tensile Specimen

Fig. 3 shows the comparison of the yield strength of five steel smooth tensile specimens before and after charging with the hydrogen. The results show that the influence of hydrogen on the yield strength of smooth tensile specimens is not noticeable and the difference of yield strength before and after charging with the hydrogen is less than 10%.

(2) The Uncracked Three-Point Bending Specimen

On the tensile surface of the uncracked three-point bending specimen there is a resistance strip and in the process of slow loading we measure the load-strain curve. When corresponding load P_s begins to deviate from a straight line by the above curve, we can compute the yield strength $\sigma_s = 3P_s S / 2BW^2$ (span=4W). The ratio of yield strength before and after charging with the hydrogen can be seen in Fig. 4. When steel strength is fairly low, even severely charged hydrogen σ_s does not change. However, the 30CrMnSiNi₂A where $\sigma_b = 166 \text{ kg/mm}^2$ and the 40CrMnSiMo where $\sigma_b = 200 \text{ kg/mm}^2$ for the ultra-high strength steel increases with the current density of the charged hydrogen and the yield strength after charging with the hydrogen, suddenly drops.

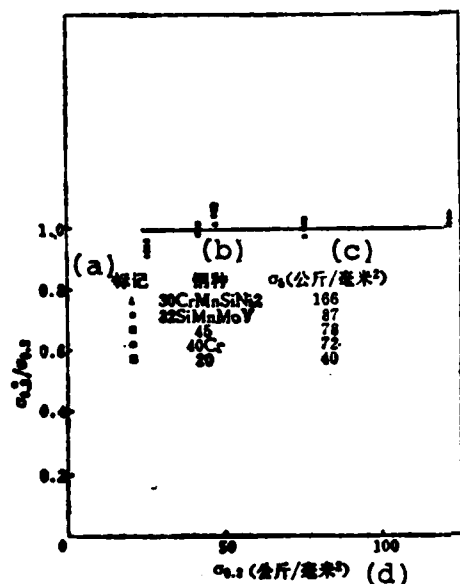


Fig. 3. The ratio of smooth tensile specimen field strength before and after charging with the hydrogen changes with the steel type. Key: (a) Symbol; (b) Steel type; (c) kg/mm²; (d) kg/mm².

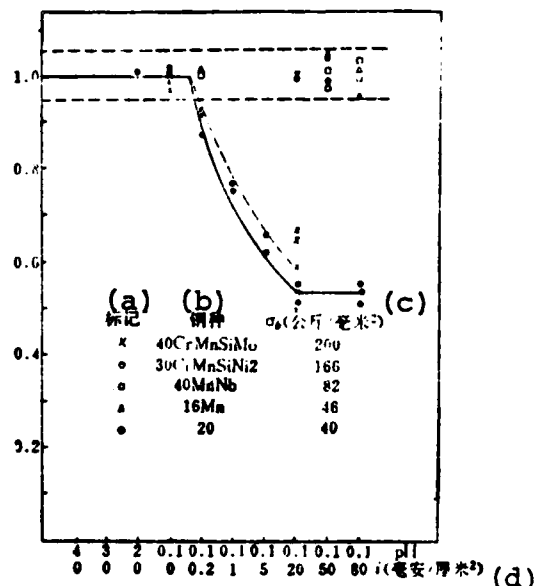


Fig. 4. The ratio of the uncracked bending specimen yield strength before and after charging with the hydrogen changes with the charged hydrogen conditions and specimen strength. Key: (a) Symbol; (b) Steel type; (c) kg/mm²; (d) Milliamps/cm².

Fig. 5 shows that this hydrogen-induced apparent yield decrease depends on the load velocity and moreover it is reversible. With fast loading after severely charging with the hydrogen (cross beam displacement velocity $V > 0.5 \text{ mm/second}$), σ_s does not decrease (compare curves 1 and 2 in Fig. 5). But if after unloading there is then slow loading ($V \leq 0.07 \text{ mm/second}$), then σ_s clearly decreases (curve 3). If there is slow loading after diffusing the hydrogen (280°C , 30 hours), then σ_s again returns to the numeric value of before charging with the hydrogen (curve 4). Because the decrease of yield strength is controlled by the atomic hydrogen in the specimen and its diffusion process, therefore it is not in the hydrogen charging process that we can cause micro-cracks to appear. In fact, once there are visible micro-cracks, then low stress, brittle cracks can be produced and

σ_s^* cannot be measured.

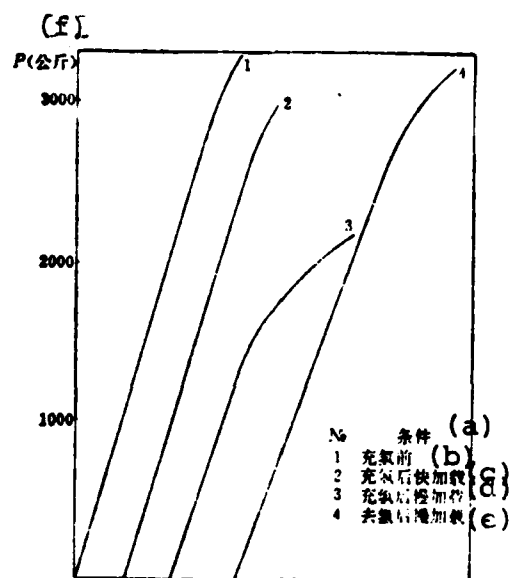


Fig. 5. Load-strain curve of uncracked bended specimen under different test conditions.

Key: (a) Condition; (b) Before charging with the hydrogen; (c) After charging with hydrogen; (d) Slow loading after charging with hydrogen; (e) Slow loading after removing the hydrogen; (f) P(kg).

In order to research the influence of plastic regions on hydrogen-induced apparent yield strength decrease, a group of specimens were pre-overloaded to $\sigma / \sigma_s = 1.3, 2.0$, causing the plastic regions to be produced. After charging with the hydrogen we slow loaded, and discovered that the influence of the existence of the plastic region on σ_s^* / σ_s was not noticeable (Fig.6). Additionally, the charged hydrogen specimen that was not overloaded first slow loaded to measure σ_s^* and then fast loaded to $\sigma / \sigma_s = 2.0$. After unloading, there again was slow loading and therefore the σ_s^* that is obtained is the same as the first time. This also shows that the influence of the original plastic region

and the work hardening process on the hydrogen-induced apparent yield strength decrease is not great.

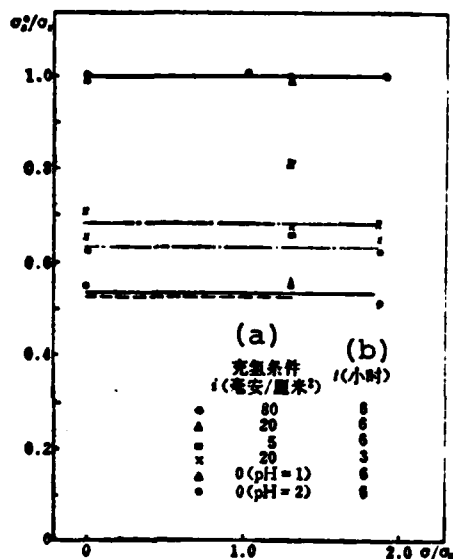


Fig. 6. Influence of pre-plastic deformation on hydrogen-induced apparent yield strength decrease σ_s^*/σ_s (30CrMnSiNi₂A, TS=166kg/mm², uncracked bending specimen). Key: (a) Hydrogen charge condition (milli-amp/cm²); (b) Hours.

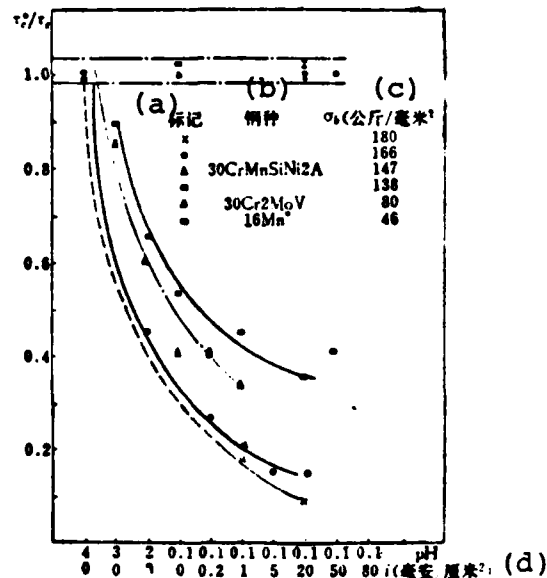


Fig. 7. Ratio τ_c^*/τ_c of specimen WOL (B=20mm) apparent yield stress before and after charging with hydrogen changes with the specimen strength and hydrogen charge conditions. Key: (a) Symbol; (b) Steel type; (c) kg/mm²; (d) Milli-amps/cm².

(3) Type I Pre-Cracked Specimen

Fig. 1 shows that for ultra-high strength steel, hydrogen-induced delayed plastic deformation is carried out along the direction of $\theta = \frac{\pi}{4}$, and by using the stress field formula of the front end of the crack [12] and rotating the coordinate axis $\theta = \pi/4$, we can then obtain the divided stress along the smooth shift line direction:

$$\tau = 0.328K_1/\sqrt{2\pi r} = 0.328PF(a/W)/B\sqrt{2\pi rW} \quad (1)$$

We consider that when the τ of ($r=r_0$) within a sufficiently large range of the front end of the crack are all equal to apparent yield stress τ_c , it will produce macroscopic plastic deformation and at the same time, the load-strain curve will diverge from a straight line. That is:

$$\tau_c = 0.328 P_c F(a/W) / B \sqrt{2\pi r_0 W} \quad (2)$$

Therefore, ratio τ_c^*/τ_c of the apparent yield stress before and after charging with hydrogen is then equal to the critical load ratio P_c^*/P_c of the load-strain curve beginning to diverge from a straight line. The τ_c^*/τ_c before and after charging with hydrogen changes with the strength and hydrogen charge conditions as shown in Fig. 7. When the strength of the steel is lower than 82kg/mm^2 , if there is severely charged hydrogen, the apparent yield stress also does not reduce. If the strength of steel is greater than 138kg/mm^2 , then following the original hydrogen quantity increase that enters in the specimen, the τ_c^*/τ_c sharply decreases.

Hydrogen-induced apparent yield stress reduction obviously depends on test temperature and loading velocity, as Fig. 8 shows. For example, when the cross beam displacement velocity is larger than 0.5mm/seconds , even if there is severely charged hydrogen, the ambient temperature in the test also cannot cause decrease of apparent yield strength. When test temperature is less than -90°C , since it causes slow loading, τ_c^* also does not decrease. Additionally, after the specimen eliminates the hydrogen (280°C , 30 hours), τ_c^* again returns to the numerical value of before charging with the hydrogen. These all show that hydrogen-induced apparent yield strength decrease is controlled by hydrogen diffusion.

(4) Type III and Type I-III Complex Specimens

The pre-cracked cylinder inlet specimen torsion (Type III

cracked), based on the torsional moment of the point when the torsional moment-rotational angle curve begins to diverge from a straight line, can compute the torsional yield stress τ_{cIII} . The tests show that after ultra-high strength steel (30 Cr₂MoV, $\sigma_b = 185 \text{ kg/mm}^2$) has severe hydrogen charge ($i = 20 \text{ milliamps/cm}^2$, 13 hours), the torsional yield strength does not decrease but conversely, due to work hardening, it can have a slight lift (Fig. 9). If a constant tensile load (K_I) is added beforehand it again reverses (Type I-II cracked), and then when K_I is relatively small (e.g. $K_I < K_{IC}/5$), the apparent torsional yield stress after charging with hydrogen also does not decrease. But following the increase of K_I , the apparent torsional yield stress after charging with hydrogen gradually decreases (Fig. 9). If we diffuse the hydrogen (240°C, 48 hours), then the apparent torsional yield stress again returns to the numerical value of before charging with the hydrogen (Fig. 9).

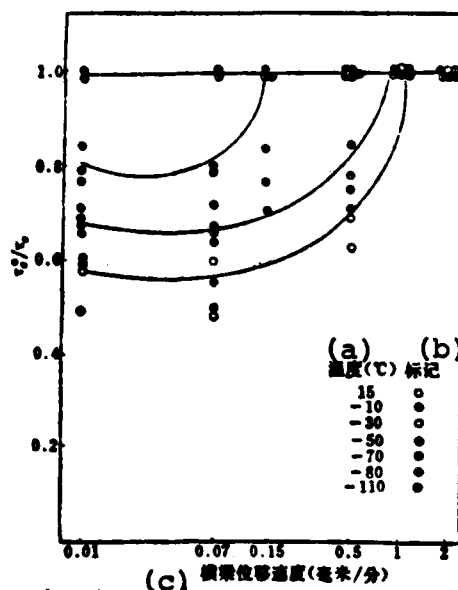


Fig. 8. Influence of test temperature and deformation velocity on hydrogen-induced apparent yield stress decrease σ_c^*/σ_c (30CrMnSiNi₂A, $\sigma_b=166\text{kg/mm}^2$, WOL specimen).
Key: (a) Temperature; (b) Symbol; (c) Cross beam displacement velocity (mm/minute).

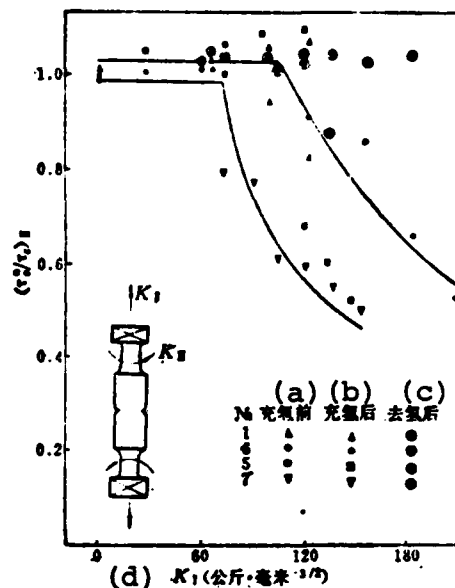


Fig. 9. Type I-III composite specimen apparent torsional yield stress before and after charging with hydrogen changes with K_I (30Cr₂MoV, $\sigma_b=185\text{kg/mm}^2$, $i=20$ milli-amperes/cm², 13 hours).
Key: (a) Before charging with hydrogen; (b) After charging with hydrogen; (c) After removing hydrogen; (d) K_I ($\text{kg}\cdot\text{mm}^{-3/2}$).

IV. DISCUSSION OF RESULTS

The above tests show that when steel strength and K_I are larger than the critical value (it is related to test environment), then in various hydrogenant environments hydrogen-induced delayed plastic deformation can be produced. Once they develop to critical conditions stress corrosion cracking or hydrogen-induced delayed cracking then can nucleate and develop. Therefore, hydrogen-induced delayed plastic deformation is a necessity and a precondition for hydrogen-induced delayed cracking. Under the effect of the three-directional stress gradients

in the front end of the crack, the atomic hydrogen that enters the specimen can be induced and diffused by the stress and accumulate in the front end of the crack. When local hydrogen concentration reaches critical value then it can cause apparent yield stress to noticeably decrease. Thus, under the effect of an even lower K_I , it can then produce hydrogen-induced delayed plasticity deformation.

When the three-directional stress gradient exists in the specimen, the distribution of the hydrogen concentration after being induced and diffused by the stress is [13].

$$C = C_0 \exp(P_h V_H / RT)$$

In the formula, C_0 is the average hydrogen concentration, V_H is the partial molar volume of the hydrogen in iron, $P_h = \frac{1}{3} (\sigma_x + \sigma_y + \sigma_z)$ is the static pressure of the fluid. We consider that after local hydrogen concentration reaches critical value, the accumulated atomic hydrogen can form "atomic hydrogen air mass" similar to that proposed by Fujita [14]. In this air mass there is extremely high internal pressure. It cannot cause atomic surface dissociation (thereby forming micro-cracks) but assists the external stress to produce local plasticity deformation. Therefore, although the yield strength of the material itself does not noticeably change, because the shearing stress weight of the internal pressure of the hydrogen air mass is very great, thus it causes the external stress that is needed for the plastic deformation of the material to become noticeably less, that is, the apparent yield stress noticeably decreases.

Because the formation of an "air mass" is controlled by diffusion of atomic hydrogen, this then can explain the influence of the temperature and the loading velocity (Figs. 5 and 8). Because the "air mass" is reversible, therefore it can explain various reversible phenomena. For example, after the hydrogen is removed,

the values of σ_s and the uncharged hydrogen will be identical (Figs. 5 and 9), after slow loading σ_s decreases, again there is fast loading and σ_s again rises to the original value. Because the pressure of the air mass is very great and moreover is unrelated to the positioned potential complex structure, this then causes the apparent yield stress to be unrelated to whether or not there exists pre-plastic deformation (Fig. 6).

As to the single direction tensile specimen, because stress gradation does not exist, $C=C_0$. When there is tensile, in each place hydrogen concentration cannot reach critical value and form an air mass and thus σ_s also does not noticeably decrease. For pre-cracked torsional specimens (Type II), although there is stress gradation, $P_h=0$. It still cannot form an air mass and thus γ_c after charging with the hydrogen does not reduce (Fig.9). Because P_h and K_I form a direct ratio, only when K_I (i.e., P_h) is sufficiently large can it cause C to reach critical value and form an air mass. Tests on the Type I-III complex type prove this point (Fig. 9). Therefore it can also explain why a K_{ISCC} exists in any hydrogenant environment, and when lower than that it then cannot produce hydrogen-induced delayed plastic deformation and hydrogen-induced cracking [10].

Because in the plastic region of the front end of the crack the largest P_h and the steel strength form a direct ratio [13], therefore C also increases with the increase of steel strength. Thus, we can explain the dependent relationship of apparent yield strength decrease after charging with the hydrogen and the specimen strength (Figs. 4 and 7). The hydrogen charge conditions influence C_0 and thus can noticeably influence apparent yield strength (Figs. 4 and 7).

According to equation (1), when K_I is equal to critical value K_{IH} , the front end of the crack has an amply large $(r-r_c)$ inside

the distance. The shearing stress along the smooth shift direction is always equal to apparent yield stress τ_c^* and thus produces delayed plasticity deformation (see Fig. 4). That is:

$$\tau_c^* = K_{IH} 0.328 \sqrt{2\pi r_e} = \frac{1}{D} K_{IH}$$

Because hydrogen-induced delayed plastic deformation is a necessity and a precondition for hydrogen-induced delayed cracking, therefore the above K_{IH} (or K_{ISCC}) is the critical stress field strength factor of hydrogen-induced delayed cracking (or stress corrosion cracking). The above formula shows that the variation patterns of K_{IH} (K_{ISCC}) which follows the strength or the hydrogen amount entering the specimen (achieved through changing the environment), and the effective yield stress are alike. Therefore, according to the results in Fig. 7, we can satisfactorily explain the dependent relationship of K_{ISCC} and da/dt on the specimen strength and experimental environment [10].

V. CONCLUSIONS

(1) Only if the steel strength and K_I are larger than critical value, can we produce hydrogen-induced delayed plastic deformation in any hydrogenant environment. When it develops into a critical state it then can cause production and expansion of delayed cracking. Hydrogen-induced delayed plastic deformation is a necessity or a precondition of hydrogen-induced cracking.

(2) The influence of hydrogen on smooth tensile specimens and pre-cracked torsional specimens (Type II) is not obvious, but if tensile stress gradation exists in the specimen (such as bending, Type I, or Type I-III complex cracked specimens), then hydrogen can obviously decrease the apparent yield strength. Moreover, it strongly depends on the strength of the material and the average amount of hydrogen that enters the specimen.

(3) Hydrogen-induced apparent yield strength decrease is

related to test temperature and loading velocity and therefore it is controlled by atomic hydrogen diffusion. Moreover, it is reversible. Additionally, it is unrelated to whether or not there is pre-plastic deformation or work hardening. We can consider that atomic hydrogen goes through stress-induced diffusion and accumulates in the largest three-directional stress area. When its concentration reaches critical value, it can then cause apparent yield stress to noticeably reduce and thus produce hydrogen-induced delayed plasticity deformation.

Comrades Zhu Fengwu, Deng Baojun, Liu Hui et al participated in part of the test operations. Professor Ke Jun gave valuable opinions on the work of this paper. We would especially like to express our thanks here.

References

- [1] C.A. Zapffe and C.E. Sims, "Hydrogen Embrittlement and Defects in Steel". Trans. AIME, Vol 145 (1941) 225.
- [2] N.J. Petch and P. Stables, "Delayed Fracture of Metals Under Static Load", Vol 169, (1952) 842.
- [3] R.A. Oriani, P.H. Josephic, "Equilibrium Aspects of Hydrogen-Induced Cracking of Steels", Act Met., Vol 22, (1974) 1065.
- [4] C.D. Beachem, "A New Model for Hydrogen-Assisted Cracking (Hydrogen "Embrittlement")", Met. Trans., Vol 3, (1972) 437.
- [5] Wu-Yang Chu (褚武揚), Chi-Mei Hsiao (蕭紀美), Shi-Qun Li (李世群), "Hydrogen Induced Delayed Plasticity and Cracking", Scripta Met., Vol 13, (1979) 1063.
- [6] R.A. Oriani, "Hydrogen Embrittlement of Steels", Ann. Rev. of Mat. Sci., Vol 8, (1978) 539.
- [7] Chu Wuyang, Xiao Jimei, Li Shiqiong and Wang Chang, "Research on High Strength Steel Aqueous Environment Stress Corrosion," Jin Shu Xue Bao [Metallurgy Journal], No. 16, 1980, p. 179.
- [8] W.Y. Chu, C.M.Hsiao, S. Q. Li; "A New Engineering Fracture Toughness Parameter $K_{ISCC}(p)$ ", Scripta Met. Vol 13, (1979) 1057.
- [9] W.Y.Chu, S.Q.Li, C.M. Hsiao, J.Z. Tien, "Mechanism of SCC in H_2S ", Corrosion Vol 36 (1980) 475.

References (continued)

- [10] Chu Wuyang, Xiao Jimei and Li Shiqiong, "Hydrogen-Induced Crack Mechanism, Jin Shu Xue Bao [Metallurgy Journal, No. 17, 1981.
- [11] W.Y. Chu, C.M. Hsiao, S.M. Li, "Mechanism of SCC and Hydrogen-Induced Delayed Cracking" in proceeding of the 5th International Conference on Fracture, Theme 6 (1981).
- [12] Chu Wuyang, Editor, Duan Li Xue Ji Chi, [Foundations of Crack Mechanics], Science Publishing House, 1979, 29.
- [13] W.W. Gerberich, J. Garry and J.F. Lessar: "Grain Size and Concentration effects in internal and external hydrogen embrittlement", In "Effect of Hydrogen on Behavior of Materials" (A.W. Thompson and I.M. Bernstein ed.) New York (1976) 70.
- [14] F.E. Fujita, "Theory of hydrogen induced delayed fracture of steel", In "Hydrogen in Metals", Proceedings of the 2nd international congress, paris, (1977) Vol 5, 2B10.

THE 1980 ANNUAL CONFERENCE OF CSAA IN SHANGHAI

From September 4 through September 10, 1980, the China Society of Aeronautics and Astronautics (CSAA) held a comprehensive annual scientific meeting in Shanghai on aerodynamic mechanics and flight mechanics, structure strength, dynamics, electronics, and automatic control. This was a large-scale scientific meeting which was represented by 49 units with 257 people coming from various areas of scientific research, design, production and institutes of higher learning within China. Among them, 58 representatives had the positions of assistant professors, assistant researchers and higher.

The CSAA invited a group of 23 people from the American Institute of Aeronautics and Astronautics (AIAA) headed by Mr. Gibson to participate in the conference. A professor of "Kang Nai Er" University of the United States, Mr. Shen Shenpu, who was lecturing at the time at Beijing Institute of Aeronautics and Astronautics, was also invited to attend the meeting and read a paper.

The conference received 327 scientific papers and after criticism and examination the meeting was divided into four specialized groups in which 150 articles were read. 25 of them were exchanged with the American delegation. The American Delegation also submitted 18 reports. The delegation members separately participated in the paper reading and discussion activities of the first three days. The Chinese and American scientists jointly discussed scientific problems and the sphere in the conference hall was quite lively.

The papers that were read at this meeting had a noticeably high scientific level. For example, in the aerodynamic and motive force computations of flow fields, they went deeply into the areas of three dimensionality, instability, viscosity flow,

etc., and posed some new and original computation methods; flight vibration experimental research also obtained new developments; in the area of aircraft and engine strength computations, they applied the finite element method considered the aspects of temperature field, three dimensionality complex conditions, etc., and posed a comprehensive structural analysis program and some practical computation methods; in the area of fatigue and crack mechanics, there also were some original papers on a new model for the overload lag effect, counting method for the aircraft load spectrum etc. There were also some distinctive views on automatic control theory research and progress was fairly quick.

In the duration of the meeting, four department committees respectively convened work conferences, conducted summarization of the conference, appraised and selected outstanding papers and proposed arrangements for scientific activities in the near future. The aeromechanic and flight mechanic committees considered that after a two year preparation, we can convene an international science conference with the American Institute of Aeronautics and Astronautics.

This large-scale scientific conference played a positive, progressive role in the development of China's aeronautic enterprises and Chinese-American scientific exchange.

A BRIEF ABOUT THE CONFERENCE ON COMPOSITES BY CSAA

The Material and Technique Specialized Committee of the China Society of Aeronautics and Astronautics (CSAA) convened a scientific exchange conference in Beidaihe from August 21 to 27, 1980. 130 representatives from 50 units coming from various places in China participated in the conference. The goal of the conference was to review the achievements of the scientific research done in China in recent years, exchange scientific ideas, and propose the recommendation of developing China's composites to the nation.

Eight professors and specialists who were invited to and attended the conference separately gave special scientific reports on the development trends of composites abroad, the present and future prospects in the research work in China on composites and the structural design, quality control, boundary surface theory, mechanical properties, manufacturing techniques etc. of composites. There were four representatives that gave explanations regarding the applications of composites in fighter planes, guided missiles and satellites. These reports were welcomed by the conference representatives.

The conference received a total of 88 scientific papers. A total of 56 papers were read on the two specialized groups of composite techniques and composite mechanical properties and testing. These papers reflected the encouraging progress that has been obtained in China's research on composites.

In order for China's research work composites to be carried out as quickly as possible, representatives proposed a "Recommended Draft for Developing China's Composites". In the "Draft" it was proposed that we should foremost develop high performance, low cost carbon fiber and its raw and processed materials.

Because composites possess many scientific characteristics we should organically organize them according to systematic engineering requirements; then we will be able to obtain comparatively large advancement. We must further strengthen basic theoretical research work, such as composite mechanisms, micro-cosmic mechanics, structural mechanics, test criteria, methods for nondestructive testing, etc. Aside from this, the specialists in the area of developing composites also were a top priority.

The committee for composite techniques convened a work meeting during the conference, discussed the question of the formation of composite speciality groups and adopted a list of members. Professor Hu Zhenwei, specialized committee member from the University of National Defense Science and Technology, held the concurrent post of group leader, and convened the first meeting of the speciality group. They researched the related matters of publishing "Collected Articles from the First Conference on Composites", formulated plans for scientific activities and decided on a suitable time in 1982 to convene the second scientific exchange conference on composites.

THE VISIT OF THE THIRD CSAA DELEGATION TO THE UNITED STATES

A delegation of 10 people from the China Society of Aeronautics and Astronautics (CSAA) accepted the invitation from the American Institute of Aeronautics and Astronautics (AIAA) and visited the United States from August 2 to 21, 1980. This is the third visit to the United States by the CSAA following the first two visits in January and May of 1980.

The delegation participated in the Scientific Conference on Aircraft Systems and Technologies that the AIAA convened in Anaheim, Los Angeles. After the meeting, in accordance with arrangements by the AIAA, the delegation successively visited two research centers, three universities, and four manufacturing companies in Los Angeles, San Francisco and Seattle. Included among them were the Ames Research Center of NASA, the Dryden Flight Research Center, Stanford University, the California Institute of Science and Engineering, the University of Southern California, Boeing Aircraft Company, Lockheed Aircraft Company, McDonald Douglas Aircraft Company and the Scientific Development Company.

Aside from this, the person in charge of the delegation exchanged opinions with AIAA Director Mr. Gibson and Foreign Liason Department Head Mr. Gerard regarding the concrete itinerary of an AIAA delegation to visit China.

While in the United States, the delegation received a great deal of attention and were treated with warm friendship by AIAA and friends of related groups so that this visit to the United States by the delegation achieved the desired results and obtained comparatively satisfactory success.

THE VISIT OF AIAA DELEGATION TO CHINA

Accepting the invitation of the China Society of Aeronautics and Astronautics (CSAA), a delegation of 23 people from the American Institute of Aeronautics and Astronautics (AIAA) headed by Director Gibson visited China from August 30 to September 18, 1980. While in China, all the members of the delegation participated in the comprehensive Annual Science Conference that CSAA held in Shanghai, visited aeronautics factories, institutes, aeronautics schools as well as the Academia Sinica's Mechanics Institute, Engineering Thermophysics Institute and related research units. They also went sightseeing to scenic spots and historical sights. CSAA Director Shen Yuanli met with the delegation and explained the conditions of developing China's aeronautical enterprises. Director Shen Yuanli consulted with delegation head Gibson, AIAA Public Policy Department head Professor Ge Lei and International Affairs Department head Jie La, regarding the question of the future scientific exchange between CSAA and AIAA. Duan Zijun, assistant director of the Third Ministry of Machine Building, entertained the delegation.

The delegation members included technical personnel of related American aviation companies, university professors and specialists from United States Navy and Airforce research units or schools. They participated in the CSAA comprehensive Annual Science Conference with great interest. They read papers at the conference and carried out informal discussions with China aeronautical and astronautical scientific and technical workers. They also listened to the papers read by Chinese specialists and participated in discussions on the papers. Foreign friends expressed praise to the Chinese scientific and technical personnel for the success that has been gained in scientific research, production, education and application.

The delegation was very interested in the development of

China's aeronautical enterprises when visiting factories, schools and research institutes. During their visits, they thoroughly inquired about related conditions, and energetically proposed opinions for further improving operations. Their attitude was warm and friendly.

The delegation also carried out separate informal discussions with Chinese specialists on the enterprises of aeromechanics, structural strength, engines, control systems and technological materials. They explained to each other conditions of related technical developments and applications so that both sides benefited.

Through the sightseeing visits and informal discussions, the exchange of Sino-American aeronautical science and technology was further advanced and the friendship between the Chinese and American people was enhanced.

THE NATIONAL CONFERENCE ON SYSTEM SIMULATION TECHNIQUE IN LUSHAN

The second National Conference on System Simulation Technique was jointly held by the China Astronautical Society, the China Automation Society and China Aeronautical Society from October 7 to 12, 1980 in Lushan.

This conference had a total of more than 160 representatives from 106 national units participating, and a total of 97 papers were read at the conference. This conference stressed exchange in the five areas of simulation models and simulation methods, digital simulation, analogue and mixed simulation, simulation experiments and simulation applications, and physical simulation equipment. During the conference they also held two special topic lectures, five special topic discussions, and a meeting that introduced products. The scientific exchange of many forms advanced mutual understanding of those in the same areas and created extremely beneficial conditions for the further development of thrust simulation techniques.

The conference representatives considered that system simulation is a new branch in the area of automation and that it is a rising science which takes control theory, computation technology and similar principles as the foundation, and takes computers and various physical simulation equipment as the tools. It is in the process of gradually forming its own theoretical system and engineering contingency. Due to its importance in systems analysis and synthesis, as well as its noticeable results in the areas of economics, safety, economizing on energy sources and reducing environmental pollution, etc., it should attract our extensive interest. Compared with the First National Conference on System Simulation that was held in 1979, this conference had a considerable increase in the number of papers and the number of representatives. The quality of the papers also showed noticeable improve-

ment. The representatives considered that this was an extremely encouraging phenomenon.

During the conference, the China Aeronautical Society, China Automation Society and China Astronautical Society also decided on the convening of the Third National Conference on System Simulation Techniques in October 1981, and issued notices soliciting papers when the conference concluded.

END

FILMED

6-83

DTIC